Magnetic flux generation and transport in cool stars

Dissertation
zur Erlangung des Doktorgrades
der Mathematisch-Naturwissenschaftlichen Fakultäten
der Georg-August-Universität zu Göttingen

vorgelegt von
Emre Işık
aus Trabzon, Türkei

Göttingen 2007

Bibliografische Information Der Deutschen Bibliothek

Die Deutsche Bibliothek verzeichnet diese Publikation in der Deutschen Nationalbibliografie; detaillierte bibliografische Daten sind im Internet über `http://dnb.ddb.de` abrufbar.

D7
Referent: Prof. Dr. Franz Kneer
Korreferent: Prof. Dr. Manfred Schüssler
Tag der mündlichen Prüfung: 18.01.2008

ISBN 978-3-936586-78-7

Publisher: Copernicus Publications 2008
http://publications.copernicus.org
© Emre Işık

Printed in Germany

Contents

Summary **5**

1 Introduction **7**
- 1.1 Observational results . . . 7
- 1.2 Surface transport of the emerging magnetic flux . . . 9
- 1.3 The rise and emergence of magnetic flux . . . 10
- 1.4 Storage of magnetic flux . . . 11
- 1.5 Generation of magnetic flux . . . 13
- 1.6 Coupling the models . . . 14

2 Magnetic flux transport on active cool stars: starspot lifetimes **15**
- 2.1 Introduction . . . 15
- 2.2 Model setup . . . 16
- 2.3 Starspots as bipolar magnetic regions . . . 19
  - 2.3.1 Main sequence star of solar radius . . . 20
    - 2.3.1.1 The effects of large-scale flows upon lifetimes . . . 20
    - 2.3.1.2 Larger starspots and the formation of polar spots . . . 23
  - 2.3.2 A subgiant star (HR 1099) . . . 24
  - 2.3.3 Emergence of multiple bipoles . . . 26
- 2.4 Structure of starspots . . . 27
- 2.5 Discussion . . . 31

3 Effects of external flows on thin magnetic flux tubes **37**
- 3.1 Deformation of flux tubes by perpendicular flows . . . 39
  - 3.1.1 Flux tubes in the equatorial plane . . . 41
  - 3.1.2 Flux tubes outside the equatorial plane . . . 43
  - 3.1.3 Parameter study . . . 48
- 3.2 Nonlinear effects caused by finite perturbations . . . 50
  - 3.2.1 Flux tubes at high latitudes . . . 51
  - 3.2.2 Flux tubes at low latitudes . . . 53
- 3.3 Nonlinearity of the friction-induced instability . . . 54
- 3.4 Summary . . . 58
- 3.5 Conclusion . . . 59

4 A coupled model of magnetic flux generation and transport 61
- 4.1 Dynamo model . . . 61
  - 4.1.1 Differential rotation and the α-effect . . . 61
  - 4.1.2 Dynamo equations . . . 62
- 4.2 Emergence of magnetic flux . . . 64
  - 4.2.1 The removal of magnetic flux from the dynamo layer . . . 66
  - 4.2.2 The rise of flux loops . . . 70
- 4.3 Surface flux transport . . . 71
  - 4.3.1 Treatment of source BMRs . . . 71
  - 4.3.2 Size distribution and the emerging magnetic flux . . . 72
  - 4.3.3 The surface evolution of magnetic flux . . . 73
- 4.4 Rapidly rotating Sun-like stars . . . 73
  - 4.4.1 $P_{\mathrm{rot}} = 10$ d . . . 75
  - 4.4.2 $P_{\mathrm{rot}} = 2$ d . . . 78
- 4.5 Discussion . . . 79
- 4.6 Conclusions . . . 80

5 Outlook 83

A An alternative treatment of flux loss 85

Bibliography 95

Publications 103

Acknowledgements 105

Lebenslauf 107

Summary

Magnetic activity in stars with outer convection zones, such as the Sun, results from the interaction of turbulent convection, large-scale flows, and magnetic fields. In this dissertation, I consider problems concerning the generation, storage, emergence, and surface transport of solar and stellar magnetic flux.

- Surface flux transport simulations have been carried out to investigate the effects of differential rotation and meridional flow on the lifetimes of bipolar magnetic regions on dwarf and subgiant stars, in order to study the structure and evolution of starspots. It is found that the lifetime does not change considerably with emergence latitude, rotational shear, and meridional flow, but depends strongly on the tilt angles of the emerging bipolar magnetic regions, i.e., on the angle between the line connecting the two regions of opposite polarity and the local latitudinal circle. A sustained emergence of bipolar magnetic regions at mid-latitudes can lead to the formation of long-lived polar spots on stars.

- Magnetic flux storage at the bottom of the solar convection zone has been studied by analytical calculations and numerical simulations of toroidal magnetic flux tubes under the influence of perpendicular flows. I have considered the problem whether flux tubes can be stored for times of the order of years under the effects of perpendicular and longitudinal flows in the convective overshoot region. First, relations between the flow velocity and the resulting displacement and deformation of a flux tube have been obtained as a function of flow and tube parameters. Second, the dependence of the nonlinear Parker instability and the friction-induced instability on the perturbation amplitude have been investigated by numerical simulations. A comparison of the simulations with the analytical results indicates that a flux tube with a radius of 1000 km and field strength $7 \cdot 10^4$ G can be stored in the bottom of the convection zone for times on the order of a few years, if the convective velocities are of the order of 10 m s^{-1}.

- A coupled model of magnetic flux generation and transport in cool stars has been developed in order to test solar and stellar dynamo models by comparison with observations, and to gain a better understanding of the relationships between the physical processes involved. The model consists of three components: 1) field generation by hydromagnetic dynamo action at the bottom of the convection zone, 2) instability and emergence of magnetic flux tubes from the dynamo layer, 3) surface transport of the emerged flux under the influence of differential rotation, meridional flow, and turbulent diffusion. The combined model has been applied first to the Sun, using the large-scale flow pattern in the solar interior and at the surface. It is

found that the dynamo waves at the bottom of the convection zone and the surface emergence pattern match, because the deflection of rising flux tubes is small in a relatively slow rotator such as the Sun. This result supports an implicit assumption that is often made when interpreting solar dynamo models, namely that the surface activity pattern reflects the deep-seated dynamo wave pattern.

- The combined model has been applied to stars of solar structure which rotate 3 and 13 times faster than the Sun. For such rapidly rotating stars, it is found that the difference between the magnetic field patterns in the deep convection zone and on the surface can become quite significant. This stresses the importance of considering emergence and surface transport processes jointly with stellar dynamo models. It turns out that, for rapidly rotating stars, a cyclic dynamo at the bottom of the convection zone may lead to a non-cyclic surface activity. This is caused by a combination of strong overlapping between consecutive cycles, large tilt angles of emerging flux tubes, and surface flux transport. The combined model developed here can be easily extended to study magnetic activity in stars in a wide range of rotation, mass, and evolutionary state.

1 Introduction

All observed activity phenomena of the Sun and other cool stars[1] are related to the presence of magnetic fields, which affect plasmas in various environments, from the deep interiors out to upper atmospheres of stars. With the exception of very low-mass stars, which are fully convective, cool stars have a radiative core, where energy is transported by radiation, and an outer envelope where energy transport by convection dominates. In the outer envelope, the interaction of convection, rotation, and meridional circulation leads to the generation and transport of magnetic fields. The large scale magnetic fields are generated inside within the convection zone, and they become buoyant and emerge in the photosphere, the visible "surface" of the star. The emerging flux is transported by surface flows.

In the following, I will give a short summary of observations and the present understanding of the physical processes related to the generation and transport of stellar magnetic flux, starting from the photosphere down to the bottom of the convection zone.

1.1 Observational results

The Sun. The observed surface magnetic field of the Sun exhibits a considerable spatio-temporal organisation on large scales (see Fig. 1.1). Magnetic fields emerge at a latitude range of about 40° to the north and south of the equator, in the form of *bipolar magnetic regions* (hereafter BMRs), two neighbouring regions with opposite magnetic polarity. They consist of relatively dark and concentrated sunspots and pores (smaller sunspots without a penumbral structure), and smaller scale magnetic elements. BMRs have a predominantly vertical magnetic field in the photosphere. and their number and area vary with a period of about 11 years (the solar activity cycle). For a BMR, the two neighbouring regions of opposite polarity are called as the preceding (p-, leading in the sense of solar rotation), and the follower (f-, trailing in the sense of solar rotation) polarity regions. The amount of magnetic flux in BMRs ranges between 10^{20}-10^{22} Mx. The "quiet Sun" outside BMRs has weaker magnetic fields, in a much more intermittent form with mixed polarities, possibly generated by local dynamo action of surface magnetoconvection (Vögler and Schüssler 2007). Sunspots are the most coherent magnetic structures in BMRs. In the first stages of the emergence of a large BMR, pores (small dark features without a surrounding penumbra) appear. As a bipolar magnetic structure develops on a larger scale, pores coalesce to form sunspots. The formation of a sunspot occurs rather

---

[1] By the term 'cool stars' I refer to those with effective temperatures less than about 7000 K, namely between spectral types F to M, which have outer convection zones.

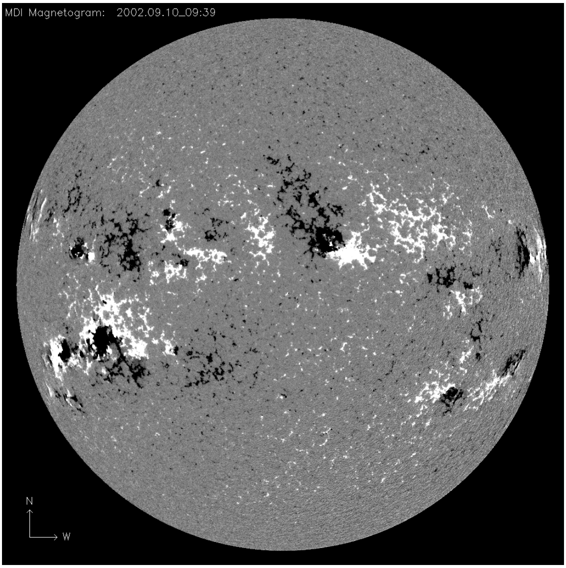

Figure 1.1: An observed magnetogram of the Sun, during the activity maximum, in 2002. Black and white colors represent the two polarities of magnetic field.

quickly, between a few hours and a few days. In the course of the emergence, the two opposite polarities of the BMR separate from each other within a range of angular distance of roughly 3° to 10°, depending on the magnetic flux content. The east-west sequence of the polarities is fixed at one hemisphere during one cycle. This is referred to as Hale's polarity rule, in which the polarity order of the f and the p regions in one hemisphere reverses every 8-9 years. This is a few years shorter than the activity cycle of about 11 years, thus the consecutive activity cycles overlap with each other for a few years. A few years before an activity cycle ends at low latitides, the next cycle starts at mid-latitudes. The opposite polarities of BMRs are almost east-west oriented, and the order of the polarity sequence is antisymmetric about the equator. In both hemispheres, the line joining the centres of opposite polarity regions shows a systematic deviation from east-west orientation (called the *tilt angle*), such that the f-polarity lies at a slightly higher latitude than the p-polarity (Joy's law). Although a large scatter is observed, the tilt angle averaged over all active regions increases with increasing latitude.

Other cool stars. In cool stars, the Sun-like activity signatures such as the chromospheric and coronal emissions, the filling factor of photospheric inhomogeneities (spots), etc. increase mainly with stellar rotation rate (a function of stellar mass and age) and convection zone depth (a function of stellar mass on the main sequence). A dimensionless parameter which combines both of these quantities is the *Rossby number*, $\mathrm{Ro} = P_{\mathrm{rot}}/\tau_{\mathrm{c}}$, where P_{rot} is the stellar rotation period and τ_{c} is the convective turnover time, which in-

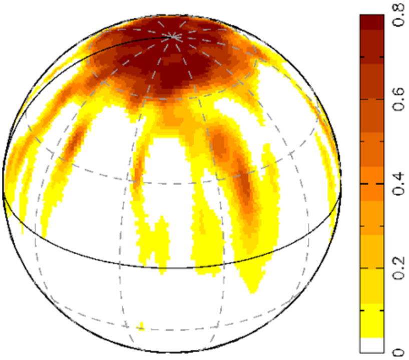

Figure 1.2: The surface brightness map of AB Doradus, a K0V type star rotating with a period of 0.69 days. The coloured areas show the distribution of dark spot-like features (Donati et al. 1999). Image credit: J.-F.Donati.

creases with stellar mass, according to mixing length models of convection. The strength of some stellar magnetic activity indices is roughly inversely proportional to the Rossby number. The Sun has a relatively thin convective envelope, and slow rotation, thus relatively weak activity. A "Sun" at a distance of a few light years from us, would possibly be chosen as an "inactive standard star", for instance to infer the level of chromospheric activity patterns on a very active star (e.g., Işık 2004), or a potential target for extrasolar planet surveys. If a cool star rotates faster than the Sun, it is either hotter (more massive), or younger, or a component of a close binary system. For cool stars rotating more rapidly than the Sun (for Sun-like stars or cooler stars), the activity patterns are concentrated to higher latitudes than in the Sun (Strassmeier 2002). Fig. 1.2 shows the reconstructed surface brightness map of a very fast rotator (AB Dor, $P_{\rm rot} \approx 0.6\ d$), on which spots around the poles are detected with the Doppler imaging technique.

1.2 Surface transport of the emerging magnetic flux

The emerging magnetic flux, being almost purely vertical at the photosphere, is transported rather passively on the surface by means of latitudinal differential rotation, meridional circulation, and convection on supergranular scales (~ 30 Mm), as shown by models of surface flux transport (Sheeley 2005). The systematic tilt of bipolar regions leads to a net transport of f-polarity magnetic flux towards the poles, which eventually reverses the sign of the polar fields.

Numerical simulations of the transport of surface fields sourced by bipolar regions reproduce the evolution of solar magnetograms (Sheeley 2005). The development and reversals of the weak dipolar component of the solar magnetic field, which amounts a few gauss near the rotational poles, can be explained by surface flux transport, owing to Hale's polarity rule and Joy's law for tilt angles.

The model developed by Baumann et al. (2004, 2006) is applied in Chapter 2 to stars by taking the stellar radii and differential rotation from observations. It is shown that the formation of long-lasting strong polar magnetic fields observed in very active stars can be explained by the emergence of strongly tilted active regions at mid- to high latitudes. We find that the lifetimes of starspots (in particular those at high latitudes) are sensitive on the size and the tilt angle of bipolar regions, as well as on the stellar radius, which determines the diffusion time.

1.3 The rise and emergence of magnetic flux

The observational evidence summarised in Sect. 1.1 suggests that azimuthally oriented magnetic fields emerge from the solar interior, in the form of (fragmented) magnetic flux tubes. As shown by Parker (1975), a horizontal magnetic flux tube located in the temperature equilibrium with the surrounding convection zone buoyantly rises with a velocity of the order of the Alfvén speed $v_{\mathrm{A}} = B/\sqrt{4\pi\rho}$. Substituting the average density in the lower convection zone ($\rho \sim 10^{-1}$ g cm^{-3}) and a field strength of $B = 10^4$ G, one finds a rise time of roughly one month through the convection zone. As pointed out by Galloway and Weiss (1981), the conditions in the stably stratified overshoot region at the bottom of the convection zone make it a potential location for the formation and storage of magnetic flux (see Sect. 1.4 for more recent developments). The field strength for which the magnetic energy density is in equipartition with the kinetic energy density ($B_{\mathrm{eq}}^2/8\pi = \rho v^2/2$) is called the equipartition field strength (B_{eq}). One finds $B_{\mathrm{eq}} \simeq 10^4$ G at the bottom of the convection zone, taking the velocity, v, from the mixing-length models of convection. A flux tube with a field strength of that order and a magnetic flux of 10^{20}-10^{22} Mx has a cross-sectional radius of 500-5000 km. If one takes $B_{\mathrm{tube}} = 10^5$ G, which is required to explain various properties of active regions (Caligari et al. 1995), the tube radius would be in the range 200-2000 km. These values are small compared to the local pressure scale height in the middle of the overshoot region, about 55000 km, and also compared to other relevant length scales, such as the radius of curvature of a toroidal flux ring, etc. This makes the *thin flux tube approximation* applicable to the problem (Defouw 1976, Roberts and Webb 1978, Spruit 1981). The approach makes the dynamical problem tractable for both the linear stability analyses and the numerical simulations. In the thin flux tube approximation, a flux tube is defined as a bundle of magnetic field lines which is in total (magnetic and gas) pressure equilibrium with the field-free surroundings, since the magneto-acoustic travel time perpendicular to the field is shorter than other relevant dynamical time scales, for a sufficiently small tube radius. Therefore the lateral pressure balance requires

$$p_i + \frac{B^2}{8\pi} = p_e, \tag{1.1}$$

so that the internal gas pressure, p_i, is less than the external gas pressure, p_e, by the amount of the magnetic pressure. In the case of thermal equilibrium with the surroundings, Eq. (1.1) and the ideal gas relation require a density deficit with respect to the ambient medium. Therefore, the flux tube feels an upward directed buoyancy force, called the *magnetic buoyancy*. The physical quantities are taken as averages over the tube cross section, and they are allowed to change along the tube axis.

According to the rising flux tube scenario, azimuthal magnetic flux tubes of superequipartition field strengths (10^4-10^5 G) experience undulatory buoyancy (Parker) instabilities in the overshoot region (Spruit and van Ballegooijen 1982, Ferriz-Mas and Schüssler 1993, 1995). They form loops rising through the convection zone up to the surface, where they create bipolar magnetic regions (BMRs) on the photosphere. Numerical simulations made by Caligari et al. (1995, 1998) reproduced many observed properties of active regions, e.g., the tilt angle relationship, proper motions of sunspots, asymmetry between the two legs of an emerging loop. The tilt forms at the top of the rising loop, and mostly at the final stages of emergence by the Coriolis force acting on the horizontally expanding tube.

Soon after the emergence, the field is likely to become dynamically disconnected from its subsurface roots, as suggested by Schüssler and Rempel (2005). In their model, the disconnection occurs at a certain depth, where the flux density of the tube is drastically reduced by rising high-entropy plasma. As a result, the dynamics of the emerged loop is governed by the effects of large-scale surface flows and not by the deeply anchored toroidal field structure.

Extensive applications of thin flux tube simulations on stars with a variety of properties (age, mass, rotation rate) have been made by Schüssler et al. (1996), Deluca et al. (1997), Granzer et al. (2000). The effects of deep convection zones (for stars cooler than the Sun), and rapid rotation have been identified as responsible for the presence of high latitude spots on stars, as predicted by Schüssler and Solanki (1992) for fast rotators.

1.4 Storage of magnetic flux

How can the required magnetic flux (flux tubes with $B \sim 10^5$ G and a total flux of 10^{24}-10^{25} Mx per 11-year activity cycle) be generated and stored in the overshoot region between the radiative interior and the convective envelope? The following is a list of some important aspects of the problem.

1. Observations of the internal rotation of the Sun by helioseismic inversion techniques have revealed that there is a region of significant radial and latitudinal velocity shear, straddling the upper radiative zone and lower convection zone, called the *tachocline*[2] (see Miesch 2005). However, the kinetic energy of a shear layer of 10^4 km thickness and a velocity difference of 100 m s^{-1} is about 10^{38} erg, about 1-2 orders of magnitude less than what is required for a total flux of 10^{24}-10^{25} Mx over an 11-year activity cycle (Howard 1974, Harvey and Zwaan 1993) at a field strength of 10^5 G. With this energy source, a serious problem is how to sustain the rotational shear to compensate for the energy transferred to magnetic energy.

2. Convective pumping of magnetic flux (see Fan 2004, Sect. 6) can provide only a negligible part of the necessary energy, because the kinetic energy density of convective flows is estimated to be about two orders of magnitude less than the magnetic energy density for a 10^5 G layer.

---

[2] The word *tachocline* literally means the [region of] rotational-velocity change.

3. According to a suggested non-local model of solar convection (e.g., Shaviv and Salpeter 1973, Pidatella and Stix 1986, Skaley and Stix 1991), the flow patterns are extremely asymmetric in the lower convection zone. In the surface layers, material loses its entropy by means of radiation and sink downwards, merging with other downdrafts. This leads to strong downflows carrying low-entropy material down to the lower convection zone, mixing there with the higher entropy material. This mixing works as a valve, which reduces the radial entropy gradient, making the stratification subadiabatic (positive radial entropy gradient), hence stably stratified. The downflows continue (to sink) at this stage, because they still have an entropy deficit with respect to the surroundings. Thus in the lower convection zone, mass motions are driven not by the convective instability, but by mass conservation and the self-readjustment of the interior towards local hydrostatic equilibrium. The downflows are finally stopped in the overshoot region, where they penetrate only because of their excess inertia. Material which penetrates into the overshoot region gains entropy excess with respect to the ambient medium, thus it is strongly decelerated. In addition, the same downflows pump magnetic flux from the convection zone down to the overshoot zone (Tobias et al. 2001, Dorch and Nordlund 2001). Regardless of the significance and importance of the overshoot region, the lower convection zone thus provides with a stable environment for the storage of azimuthal magnetic fields, until the magnetic buoyancy instabilities set in.

4. A toroidal magnetic flux tube located outside the equatorial plane can be kept in mechanical equilibrium only if it has zero buoyancy. In that case, a balance can be established between the magnetic curvature force and the Coriolis force induced by an azimuthal flow along the tube. In the case of such a balance between the magnetic and inertial forces for a neutrally buoyant flux tube, the normal (cylindrical-radial) component of the equation of motion takes the form

$$\frac{B_0^2}{4\pi R_0} - \rho_{i0} R_0 (\Omega_{e0}^2 - \Omega^2) \quad = \quad 0, \tag{1.2}$$

   where ρ_{i0} is the internal density, R_0 is the distance from the rotation axis, Ω_{e0} is the angular velocity of the external medium (taken as the reference frame in which the medium around the flux tube is at rest), and Ω is the internal angular velocity (van Ballegooijen 1982, Moreno-Insertis et al. 1992).

5. As shown by Rempel et al. (2000), a magnetic layer in the upper radiative zone can establish a mechanical equilibrium owing to a latitudinal pressure gradient of the entire layer, where the pressure force compensates for the axial component of the buoyancy force. They found that a magnetic layer extending from the upper radiative zone to the lower convection zone develops a pressure-driven equilibrium in the radiative zone, and an azimuthal flow driven equilibrium for the convective overshoot region. Therefore, the latter case allows for the storage/existence of flux tubes with a mechanical equilibrium stated in Eq. (1.2).

6. A possible mechanism which provides with sufficient potential energy source is the field intensification by flux tube "explosion" (Moreno-Insertis et al. 1995). When a

flux tube rises adiabatically in the convection zone, its internal pressure decreases more slowly than the external pressure, because of the superadiabatic temperature gradient of the convection zone. Consequently, the internal and external gas pressures would become equal at a certain height. Then the lateral pressure balance (Eq. 1.1) would yield a zero magnetic pressure. This means that the crest of the tube, which has reached this critical height, undergoes an extreme expansion. This leads to a buoyant rise of high-entropy material. Consequently, the magnetic pressure in the lower parts of the tube which are anchored in the deeper layers increase, leading to an increase of the field strength there. Rempel and Schüssler (2001) have made numerical simulations showing the dynamics of such an explosion process, and they found that the field strength can reach 10^5 G in about 6 months.

7. The formation of flux tubes can take place by means of magnetic Rayleigh-Taylor instability of a uniform magnetic layer located below a field-free layer (e.g., Fan 2001). For a layer of toroidal (azimuthal) field, perturbations which are periodic in the latitudinal direction grows faster than those which are periodic in the azimuthal direction. Because in the latter case, magnetic tension has a restoring effect.

In spite of all the work which indicate the possibility of sufficiently strong toroidal magnetic fields, the problem of flux storage is still under investigation. In principle, any sort of (magneto-)hydrodynamical instability in the bottom of the convection zone with growth times significantly shorter than about half the activity cycle time scale, poses a natural problem for flux storage. I give here a few example studies related to the storage of flux tubes. The nonlinear effects of a local updraft of material is examined by Caligari et al. (1998). They found that upflow velocities in the range 20-50 m s^{-1} can destabilise a flux tube, which form a rising loop, reaching the surface within one year. They remarked that the convective velocities determined by the mixing-length model in the overshoot layer are too small to cause such a nonlinear Parker instability. In Chapter 3, I extend this work and investigate analytically the effect of perpendicular flows acting on a toroidal flux tube. I give scaling relations between the flow parameters and the flux tube parameters, and provide conditions for the non-linear development of Parker instability and the friction-induced instability (Holzwarth et al. 2007) for a stably stored flux tube.

1.5 Generation of magnetic flux

One of the fundamental problems of astrophysics is the generation and amplification of magnetic fields on various spatial and temporal scales. The problem is how to generate and maintain magnetic fields by the motions of astrophysical plasmas. The research field which investigates these issues is called hydromagnetic dynamo theory (see e.g., Moffatt 1978). Dynamo mechanisms play a key role in many cosmical phenomena, ranging from planetary magnetism to magnetic fields in galaxies (see, e.g. Moffatt and Murdin 2000, Rüdiger and Hollerbach 2004, Brandenburg and Subramanian 2005).

Apart from the general consensus that sunspots and the periodic nature of solar activity result from a cyclic dynamo mechanism, many aspects of solar and stellar dynamo problem remain unresolved, so that a complete dynamo model which uniquely predicts the observations and does not rely on parametrisation has not been constructed (see Ossendrijver 2003, Charbonneau 2005). The reason is two-fold. Firstly, magnetic fields within solar/stellar convection zones are not directly observable. On the theoretical side, highly complex and nonlinear interactions of turbulence - the theory of which is itself incomplete - with convection, differential rotation, meridional circulation, and magnetic fields are poorly understood.

1.6 Coupling the models

In the literature, the work is mainly focused on the individual aspects of solar and stellar magnetism, e.g., as described in the previous sections. The most global models that incorporate various aspects of solar magnetism are the Babcock-Leighton-type [flux transport] dynamo models (e.g., Dikpati and Charbonneau 1999). They parametrise the effects of magnetic buoyancy and assume that the surface distribution of the field is the same as at the bottom of the convection zone. The first attempt to combine models of flux emergence and surface transport has been presented by Holzwarth et al. (2006) for rapidly rotating cool stars. The authors prescribe butterfly diagrams for the initial distribution of flux tubes in the bottom of the stellar convection zone, and they let the Parker-unstable thin flux tubes rise through the convection zone, under the influence of strong meridional flows and rapid rotation. The resulting emergence pattern is then used as input for a surface flux transport model. In their model, meridional flows are an order of magnitude faster than the solar values, and this is the primary effect reproducing the intermingling of mixed polarity regions around the rotational poles, similar to the detected patterns on AB Dor, a rapidly rotating K-type dwarf star. In Chapter 4, I present the first model which combines the generation, emergence, and surface transport of solar magnetic flux, and I apply it to the cases of other, more active cool stars. The coupled model is not meant to be a conclusive solution to the solar dynamo problem itself, neither is it intended to “predict” solar magnetic cycles. It is made to have a reference model which represents the basic features of solar magnetic activity with consistently coupled components. The main aim is to check the consistency of different model components with each other, and furthermore apply the model to more active cool stars, in order to gain insight on the physics of stellar magnetic activity in a broader scale.

2 Magnetic flux transport on active cool stars: starspot lifetimes[1]

2.1 Introduction

Magnetic flux emerges on the solar surface in the form of bipolar magnetic regions (hereafter BMRs or bipoles), the larger ones of which include sunspots, pores, and plages (consisting of small-scale magnetic flux concentrations) in two patches of opposite polarity. The observations indicate that, after their emergence, magnetic flux in BMRs is subject to flux transport by means of convective motions on different scales (granulation, supergranulation), differential rotation, and meridional flow. Under the effects of these flows, magnetic flux is redistributed on the surface, leading to flux cancellation and polarity reversals of the polar field, which is possibly an important ingredient of the underlying dynamo mechanism. Magnetic flux transport on the surface of the Sun has been studied through numerical simulations by several authors, who were able to reproduce the evolution of the radial magnetic field on the solar surface through the magnetic cycle (e.g., Wang et al. 1989a, Dikpati and Choudhuri 1995, van Ballegooijen et al. 1998, Wang 1998, Mackay et al. 2002, Baumann et al. 2004).

Observations of spots and magnetic fields on stars other than the Sun are mainly restricted to rapidly rotating, i.e. magnetically active, nearby G-K stars, because of the relatively high spectral resolution and low noise required by the indirect surface imaging techniques. One of the striking observational results is that, in contrast to the solar case, long-lived spots or spot groups lie at high latitudes and often even cover the rotational poles (see Strassmeier 2002), in some cases with intermingling of opposite polarities (Donati et al. 2003a). Such accumulation of magnetic flux at high latitudes can arise by a combination of poleward deflection of rising flux tubes by the Coriolis force (Schüssler and Solanki 1992, Schüssler et al. 1996, Granzer et al. 2000) and surface flux transport after emergence (Schrijver 2001, Schrijver and Title 2001). Recently, Mackay et al. (2004) used a flux transport model to show that the observed intermingling of large amounts of positive and negative magnetic flux at very high latitudes could occur with a flux emergence rate 30 times that of the Sun, a range of emergence latitudes between 50°-70°, and a meridional flow of 100 $\mathrm{m\,s^{-1}}$, which is about 10 times faster than in the case of the Sun. Intriguingly, the observed fields of very active stars often appear to have a strong azimuthal component (Donati et al. 2003a), which is not observed in the case of the Sun[2].

---

[1] This chapter is a slightly modified and extended version of the article published by Işık et al. (2007).

[2] Recently, a weak toroidal field component on the solar surface has been reported, which varies in phase with the magnetic cycle (Ulrich and Boyden 2005).

Observational techniques like Doppler imaging can only detect starspots which are much larger than typical sunspots. Because of the limited resolution of the imaging techniques, it is unknown whether the observed starspots are single large spots or conglomerates of smaller spots (cf. Solanki and Unruh 2004). In any case, except for the polar spots, which in some cases persist up to decades (cf. Hussain 2002), the observed starspots have lifetimes that are less than one month (Barnes et al. 1998, Hussain 2002, Kővári et al. 2004). An individual sunspot (and presumably a starspot as well) is a more coherent structure than the magnetic region in which it is embedded: because of the magnetic forces, its magnetic flux is not passively transported by convective flows or sheared by differential rotation, but resists to them (e.g., by suppressing granulation). Sunspots gradually lose flux through (turbulent) erosion by convection at the boundaries (Petrovay and Moreno-Insertis 1997). The decay time of an individual sunspot is proportional to its maximum diameter (Petrovay and van Driel-Gesztelyi 1997), which is consistent with the turbulent erosion models (Petrovay and Moreno-Insertis 1997). On the other hand, a cluster of small spots is more likely to be dispersed by differential rotation, meridional flow, and supergranulation. The structure and evolution of starspots, in comparison with sunspots, has been reviewed by Schrijver (2002). So far there has been no theoretical investigation devoted to the lifetimes of starspots.

In this chapter, we present simulations of BMR and starspot evolution on the basis of a linear surface flux transport model, with an aim to explain the observed starspot lifetimes, and to compare various configurations. We carry out numerical simulations in order to examine the evolution of the radial magnetic flux in monolithic as well as in clustered forms, and to infer lifetimes for starspots covering a range of sizes, initial latitudes, and transport parameters. We apply the surface flux transport code of Baumann et al. (2004) (see also Baumann 2005), to the cases of a single bipolar magnetic region with different parameters, to a multitude of bipoles at high latitudes, to a unipolar cluster of starspots, and to a large monolithic, unipolar spot. The plan of the chapter is as follows: the surface flux transport model and the definition of starspots are introduced in Sect. 2.2. The evolution of bipolar regions is treated in Sect. 2.3, with emphasis on the effects of surface flows and the emergence latitude upon BMR lifetimes. The results for a set of starspot configurations are discussed in Sect. 2.4 and concluding remarks are given in Sect. 2.5.

2.2 Model setup

To simplify the problem, we ignore any horizontal components of the surface magnetic field and assume that the magnetic field on the stellar surface is directed only in the radial (vertical) direction, as well justified for the case of the Sun (Solanki 1993, Martínez Pillet et al. 1997). Stellar magnetic regions are assumed to have a bipolar structure with a geometry similar to those of the solar BMRs (except for Sect. 2.4, in which unipolar spots are considered). The flux transport model is restricted to the surface, which is defined by the stellar radius, $r = R_\star$. The signed flux density of a BMR is written in the form

$$B(\lambda, \phi) = B^{+}(\lambda, \phi) - B^{-}(\lambda, \phi), \tag{2.1}$$

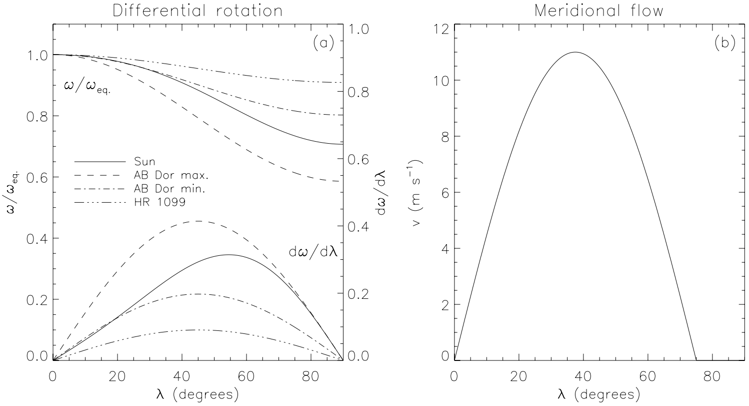

Figure 2.1: (a) Angular velocity normalised to its equatorial ($\lambda = 0$) value (left axis, top curves) and shear rate (right axis, bottom curves) for three stars: the Sun, AB Dor, and HR 1099. ‘AB Dor max.’ and ‘AB Dor min.’ correspond to the maximum and minimum observed $\Delta\omega$ values obtained by Donati et al. (2003b). (b) Meridional flow velocity (positive means poleward flow). Both plots are for the northern hemisphere. The shear rate and the meridional flow profiles are antisymmetric with respect to the equator.

where λ denotes the stellar latitude and ϕ the longitude. Following van Ballegooijen et al. (1998) and Baumann et al. (2004), we assume the unsigned field strength of the two polarities of a newly emerged BMR to be

$$B^{\pm}(\lambda, \phi) = B_0 \exp\left[-\frac{2\,[1-\cos\beta_{\pm}(\lambda,\phi)]}{\beta_0^2}\right]. \tag{2.2}$$

Here, $\beta_{\pm}(\lambda, \phi)$ are the heliocentric angles between any given position (λ, ϕ) and the centre of the positive and negative polarities, $(\lambda_{\pm}, \phi_{\pm})$. The total size of a BMR is controlled by β_0, the initial characteristic width of each polarity, and by the angular separation of the centres of the two poles, $\Delta\beta$, which are related by the relation $\beta_0 = 0.4\Delta\beta$. B_0 is arbitrarily set to 250 G, a reasonable value for the case of the Sun [3]. Initially the BMR is placed at a given latitude according to one of the following configurations: (1) both poles of the BMR are at the same latitude, (2) the line joining the centres of the two polarities makes an angle α with a latitudinal circle, which is called the tilt angle. The latitude dependence is chosen to be $\alpha = 0.5\lambda_0$, where λ_0 is the latitude of emergence. The orientation of a bipole axis (i.e., the line joining the centres of the two polarities) is such that the leading polarity (with respect to the direction of rotation) is nearer to the equator. The time evolution of the radial magnetic field is determined by the induction equation, which is written in spherical coordinates $(R_\star, \lambda, \phi)$ as

---

[3] The magnetic field strength can be scaled arbitrarily, because the field evolution described by Eq. (2.3) is linear and passive. Therefore, a different peak strength for the initial field results in the *same* patterns of flux evolution, only scaled by a factor in the field strength. Because we take a fixed fraction of B_0 as the threshold field strength to define the size of an evolving BMR (see below), the resulting flux evolution is independent of the initial peak strength. Another reason for choosing B_0=250 G is that we get magnetic fluxes comparable to those of solar active regions.

$$\begin{aligned}\frac{\partial B}{\partial t} &= -\omega(\lambda)\frac{\partial B}{\partial \phi} + \frac{1}{R_\star \cos\lambda}\frac{\partial}{\partial \lambda}\left(v(\lambda) B \cos\lambda\right) \\ &\quad + \frac{\eta}{R_\star^2}\left[\frac{1}{\cos\lambda}\frac{\partial}{\partial\lambda}\left(\cos\lambda\frac{\partial B}{\partial\lambda}\right) + \frac{1}{\cos^2\lambda}\frac{\partial^2 B}{\partial\lambda^2}\right] \\ &\quad + S(\lambda,\phi) - D_r(\eta_r), \end{aligned} \tag{2.3}$$

where λ is the latitude, $\omega(\lambda)$ is the angular velocity of rotation, $v(\lambda)$ is the meridional flow velocity, η is the constant coefficient for horizontal turbulent diffusion associated with the nonstationary convective motions (supergranulation in the case of the Sun), $S(\lambda, \phi)$ is the source term describing the emergence of the BMRs, and D_r an additional decay term representing the radial diffusion of magnetic flux with an effective diffusivity η_r (Baumann et al. 2006). For the numerical solution of Eq. (2.3), the magnetic field is expanded in spherical harmonics with a maximum degree of 63, which (for $R_\star = R_\odot$) corresponds roughly to the observed size of supergranules ($\approx$30 Mm) on the Sun. For the newly emerged BMRs, the spherical harmonic coefficients defining the field distribution are multiplied by a spatial filter of the form $\exp[-\beta_0^2 l(l+1)/4]$ (van Ballegooijen et al. 1998), in order to diminish the effect of ringing (Gibbs phenomenon) caused by the truncation of the expansion in spherical harmonics.

The relevant quantities for the flux transport are the latitudinal angular velocity profile $\omega(\lambda)$, the meridional flow profile $v(\lambda)$, the horizontal turbulent magnetic diffusivity, η, and the effective radial diffusivity, η_r. As a reference configuration we consider the values corresponding to the solar case. The angular velocity profile is taken after Snodgrass (1983),

$$\omega(\lambda) = 13.38 - 2.30\sin^2\lambda - 1.62\sin^4\lambda \quad \text{deg day}^{-1}, \tag{2.4}$$

and the meridional flow profile (Snodgrass and Dailey 1996, Hathaway 1996) is assumed as

$$v(\lambda) = \begin{cases} -v_0 \sin(\pi\lambda/\lambda_c) & : \text{ if } |\lambda| < \lambda_c \\ 0 & : \text{ otherwise,} \end{cases} \tag{2.5}$$

where $v_0 = 11$ m s^{-1} and $\lambda_c = \pm 75°$ (van Ballegooijen et al. 1998, Baumann et al. 2004). For the case of rapid rotators, the following differential rotation profile is used:

$$\omega(\lambda) = \omega_{eq} - \Delta\omega \sin^2\lambda. \tag{2.6}$$

Here, ω_{eq} is the equatorial angular velocity and $\Delta\omega$ is the velocity difference between the poles and the equator. The values of the latter are 5.54 and 2.64 deg day^{-1}, for AB Dor (maximum and minimum observed surface shear rates), and 1.21 deg day^{-1} for HR 1099 (Donati et al. 2003b). The differential rotation and meridional flow profiles given by Eqs. (2.4)-(2.6) are shown in Fig. 2.1.

In the following, we consider the evolution of BMRs on stars with various shear rates and radii in order to investigate the impact of surface flows on the lifetimes for BMRs of different sizes. Then we consider the evolution of starspots in Sect. 2.4.

2.3 Starspots as bipolar magnetic regions

In this section we present numerical simulations of single bipolar magnetic regions and of multiple BMRs emerging randomly around a polar spot. Partly, BMRs are important because they harbour starspots visible in Doppler imaging. Partly, the Zeeman-Doppler imaging technique should be able to detect the largest BMRs on stars. In this connection, we consider starspots as bipolar magnetic regions. We take the horizontal diffusivity $\eta = 600$ km^2 s^{-1} (Wang et al. 1989b) and the effective radial diffusivity $\eta_r = 100$ km^2 s^{-1} (Baumann et al. 2006). These values are appropriate for the Sun. We adopt them for all the simulations in this section, since the properties of the large-scale convective flows (which determine the turbulent diffusivities) are unknown for stars with a different mass in a different evolutionary stage. This uncertainty should be kept in mind when considering the results for stars other than the Sun. The smallest BMR considered here has $\beta_0 = 4^\circ, \Delta\beta = 10^\circ$, roughly representing the largest solar BMRs shortly after their complete emergence, and also the smallest structures that can be resolved in Zeeman-Doppler reconstructions of active cool stars (Donati et al. 2003a). We consider this angular size as the 'standard' one in Sec. 2.3.1 and Sec. 2.3.2. The area of a BMR at a given time is determined from the corresponding simulated field distribution on an angular grid with 360 points in azimuth and 180 points in latitude, by adding up the area for which a threshold magnetic field strength is exceeded. Fig. 2.2 shows the fractional area of the region as a function of the threshold field strength and time. If the normalised threshold strength is taken below about 0.2, the area determined by that threshold shows an an initial increase owing the diffusion of the magnetic field to a larger area. After a certain time, the region defined by the threshold starts to shrink. In the present context, the threshold field strength is taken to be 0.14 times the value of the initial peak field strength B_0, so that the initial area for the 'standard' BMR is equal to 323 square degrees, or about 8 thousands of the stellar surface area. This value is determined by requiring that the lifetime of a BMR (as defined by the time when the field strength falls entirely below the threshold) with $\beta_0 = 4^\circ, \Delta\beta = 10^\circ$ becomes equal to two months, which is about the lifetime of a similar-sized BMR around a solar minimum, which we estimated visually from SOHO/MDI synoptic magnetograms for the time period 25.06.2004 and 14.09.2004 (Carrington rotations from 2018 to 2020). We obtained this estimate by tracking relatively isolated BMRs of size $\Delta\beta \approx 10^\circ$ at a latitude of about 10° on consecutive synoptic magnetograms. The estimated lifetimes of around two Carrington rotations, roughly two months after their maximum size of development, can be compared with the largest BMRs shown by Harvey (1993), which have areas up to 70 square degrees and lifetimes up to 3 months.

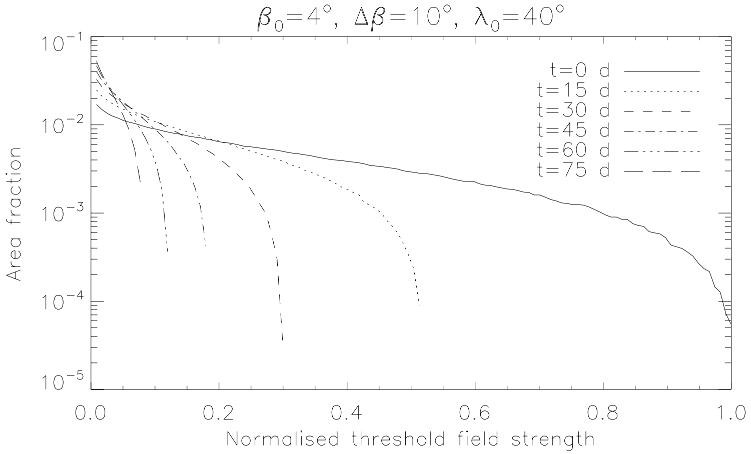

Figure 2.2: Profiles of area (in fractions of the solar surface area) of a BMR as a function of the threshold field strength, for different times (in days) after the emergence. The initial BMR has the size corresponding to $\beta_0 = 4°$ and $\Delta\beta = 10°$, which covers a fraction 0.8% of the solar surface, and emerges at $\lambda_0 = 40°$ latitude. The threshold field strength is normalised to the initial peak field strength. The lower the threshold value, the longer the duration of the initial expansion of the BMR. Above a threshold value of 0.2, the area always decreases, i.e., BMR always shrinks.

2.3.1 Main sequence star of solar radius

In this section we present simulations of the evolution of single BMRs on a star of solar radius. Examples are the Sun and the rapidly rotating K0-dwarf AB Doradus, ($R \approx R_\odot$, according to Ambruster et al. (2003).

2.3.1.1 The effects of large-scale flows upon lifetimes

Fig. 2.3 illustrates the dependence of BMR lifetime on emergence latitude. It shows the evolution of BMRs with $\beta_0 = 4°, \Delta\beta = 10°$, for three different emergence latitudes: 10°, 40°, and 60°. The flow profiles represent the solar case given by Eqs. (2.4) and (2.5). It can be seen that, 55 days after the emergence, the BMR emerged at $\lambda_0 = 60°$ has more remaining flux than the one at $\lambda_0 = 10°$, while the one at $\lambda_0 = 40°$ has already lost all its flux with field strengths above the threshold. Fig. 2.4a shows the evolution of area (normalised to its initial value) for the BMR at $\lambda_0 = 40°$ and Fig. 2.4b shows the BMR lifetime as a function of the emergence latitude. For all emergence latitudes, the area increases in the initial phase by about 10 percent, owing to the spreading by diffusion of the field above the threshold (e.g., Fig. 2.4a for 40°). After about 15 days, the region above the threshold field strength begins to shrink, as the reduction of its length scales (steepening of the field

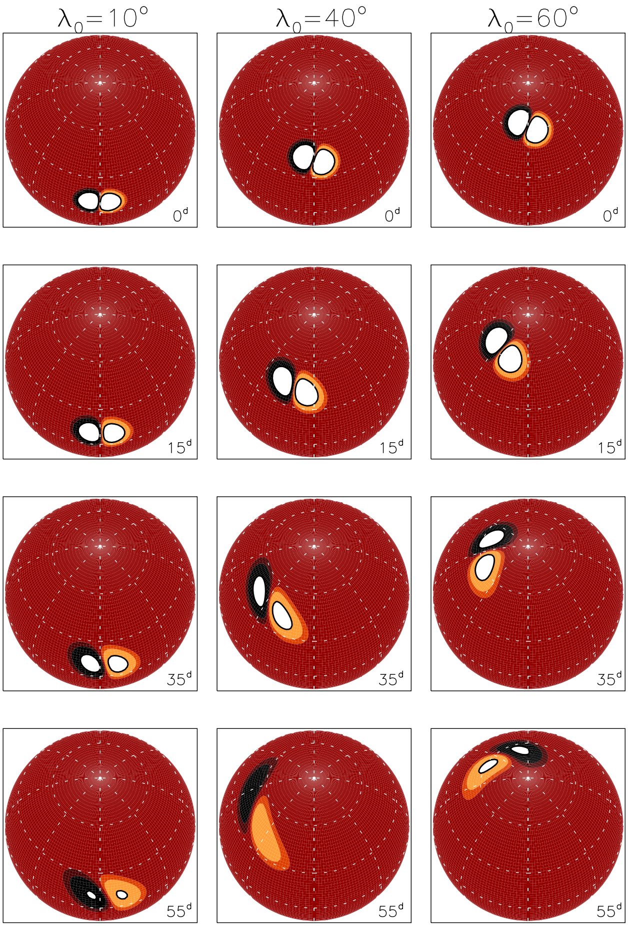

Figure 2.3: Evolution of BMRs with different emergence latitudes (λ_0), with tilt angles equal to $0.5\lambda_0$, and with solar surface shear. Magnetic field values above the threshold are indicated by white regions enclosed by a thick black contour. The projections are centred at a fixed meridian and 60° latitude. The latitude circles are plotted with 30° intervals. Elapsed time after emergence (in days) is indicated. Stellar (differential) rotation is shown with respect to the rest frame of the equator. The initial BMR configuration corresponds to $\beta_0 = 4°, \Delta\beta = 10°$, leading to an initial area of about 323 square degrees, or 0.8% of the solar/stellar surface area.

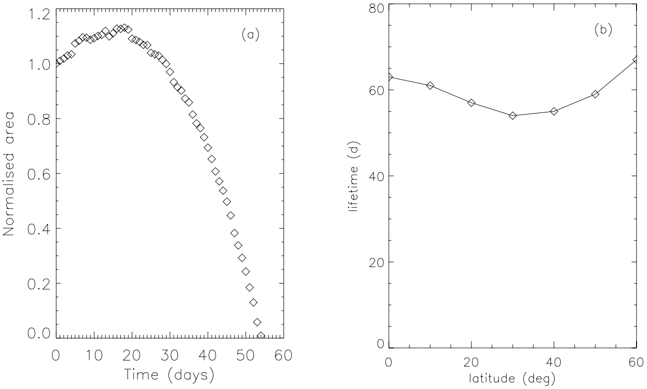

Figure 2.4: (a) Time variation of BMR area normalised to its initial value, for a BMR with $\beta_0 = 4°, \Delta\beta = 10°$ emerged at 40°. BMR area is defined as the area above a given threshold (see text). (b) BMR lifetime as a function of the emergence latitude.

gradient) by means of surface shear leads to increasing diffusion rates. The strength of this effect is proportional to the local surface shear (see Fig. 2.1a), and is partly responsible for the variation of lifetime as a function of emergence latitude (Fig. 2.4b). The effect can also be seen when one compares the evolution of BMRs at 10° and 40° in Fig. 2.3. On the other hand, the bipole at 60° lives longer than the ones at 10° and 40°, although the local shear rate is higher for the former. The reason is the meridional flow (see Fig. 2.1b): firstly, there is an acceleration of the poleward flow with increasing latitude until around 37°, above which the flow is decelerated. Therefore, a BMR emerging at a latitude lower (higher) than about 37° experiences a diverging (converging) flow. The effect can be seen in Fig. 2.5, in which lifetimes are plotted as a function of emergence latitude, in the presence and absence of the meridional flow (Eq. 2.5). Another effect of the meridional flow is that low-latitude BMRs are advected to latitudes with stronger shear, whereas the high-latitude BMRs are moved to regions with less shear. Both of the effects mentioned above contribute to the longer lifetimes of high-latitude BMRs.

Next we consider the effect of varying the latitudinal rotation profile (surface shear) by using the results for the solar profile (as above), and those for AB Doradus (Fig. 2.1a), with observed minimum and maximum values for $\Delta\omega$ of 2.64 and 5.54 deg day^{-1}, respectively (Donati et al. 2003b). The variation of BMR lifetime as a function of the emergence latitude for the three cases is shown in Fig. 2.6, for tilt angles $\alpha = 0.5\lambda_0$ (Fig. 2.6a) and $\alpha = 0$ (Fig. 2.6b), respectively. The lifetimes are affected by the shape of the rotational shear profile (cf. Fig. 2.1a). For instance, for $\lambda_0 = 30°$, 56% weaker shear leads to an about 37% (14 days) longer lifetime. The effect of meridional flow becomes more noticeable for the cases with smaller rotational shear. For $\alpha = 0$, the BMRs suffer more flux cancellation at the longer neutral line between the opposite polarities, so that they live

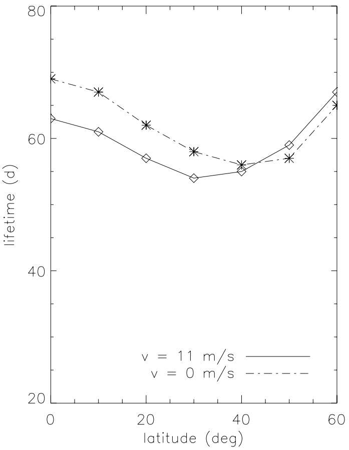

Figure 2.5: The effect of meridional flow upon lifetimes of BMRs emerged at various latitudes. The solar differential rotation profile has been used. The diamond symbols show the lifetimes with a meridional flow according to Eq. 2.5 (Fig. 2.1b). The asterisks show lifetimes in the absence of meridional flow. Below $\lambda_0 \approx 40°$, meridional flow decreases the lifetimes, because the meridional flow accelerates with latitude and carries the BMR to regions with larger rotational shear. Above $\lambda_0 \approx 40°$, it decelerates with latitude and also carries the BMR to regions with less shear (cf. Fig. 2.1).

shorter than their tilted counterparts. The presence of a tilt angle $\alpha = 0.5\lambda_0$ prolongs the lifetimes, particularly so at higher latitudes: because the opposite polarities have different angular velocities, they gradually separate so that the neutral line at the interface for flux cancellation shortens (see Fig. 2.3).

2.3.1.2 Larger starspots and the formation of polar spots

Larger BMRs have systematically longer lifetimes owing to a larger initial area. Fig. 2.7 shows the lifetimes, for 40° emergence latitude, of BMRs with initial area equal to or larger than in the reference case presented above. The presence of a tilt (filled circles) leads to polarity separation by differential rotation, thus reducing the cancellation rate and leading to longer lifetimes, particularly so for very large BMRs. This is illustrated in Fig. 2.8, which shows BMRs of initial area fractions (area covered by the BMR as a fraction of the stellar surface area) 0.008 and 0.12 shortly before completely falling below the threshold. For non-zero tilt ($\alpha > 0$), the follower polarity of the large BMR forms a polar cap after about 6 months (panel c). Its nearly circular shape decelerates its diffusive spreading because the shear can no longer reduce its effective length scale. For the non-tilted case ($\alpha > 0$), however, the two polarities rotate with the same speed and spiral

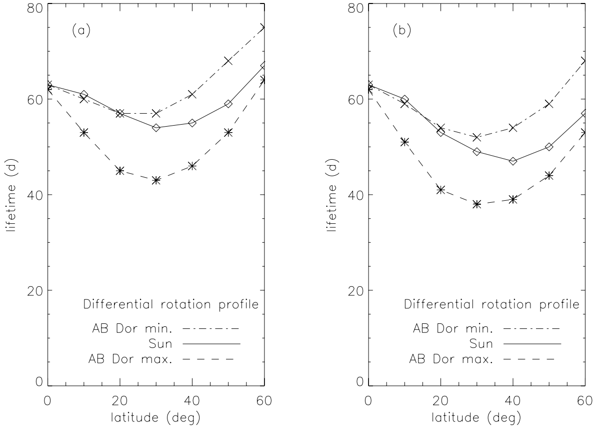

Figure 2.6: Lifetime of BMRs as a function of the emergence latitude, for three differential rotation (surface shear) profiles: solar shear (diamonds), the minimum observed shear for AB Dor (crosses), and the maximum observed shear for AB Dor (asterisks). (a) for the tilt angle relation $\alpha = 0.5\lambda_0$. (b) $\alpha = 0$.

towards the rotational pole through the action of the meridional flow, leading to enhanced flux cancellation at the elongated neutral line.

Fig. 2.9 shows the evolution of area for the sample of tilted BMRs that were given in Fig. 2.7. The area is normalised to its initial value for each simulation. Note the sudden decrease in the decay rate for the largest three BMRs in the sample. This change occurs when the maximum field strength of one polarity, the preceding one in the present case, falls below the threshold value. The effect can also be seen in Fig. 2.8c: the preceding polarity region already fell below the threshold when it had been stretched in the azimuthal direction by the strong differential rotation. On the other hand, after the formation of a polar cap of the follower polarity, the only remaining "area" of interest is the slowly diffusing polar cap. This sudden decrease in the decay rate becomes more abrupt for larger BMRs because the polar spot has a larger length scale and is confined by the meridional flow, which leads to a slower decay.

2.3.2 A subgiant star (HR 1099)

In a subgiant star like the active component of the binary system HR 1099 with a radius of 3.3 $R_\odot$, lifetimes for the same initial area fractions as in the case of a 1 $R_\odot$ star are much longer. This is expected for two reasons: firstly, surface differential rotation is weaker in the case of HR 1099 (see Fig. 2.1), and secondly, the characteristic decay time τ_l of the

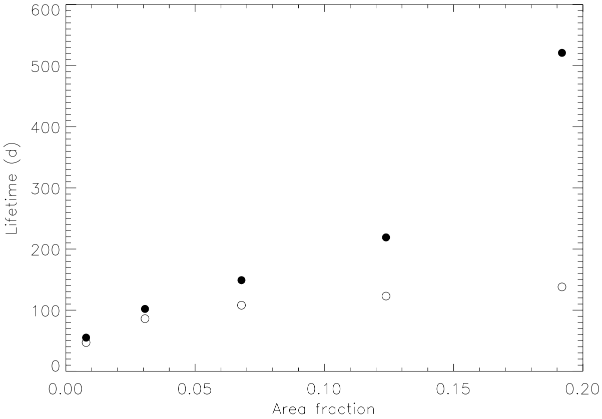

Figure 2.7: Variation of BMR lifetime as a function of initial size. The initial angular radii of each pole of the BMR are $\beta_0 = 4°, 8°, 12°, 16°, 20°$, and the initial separation between the poles satisfies the relation $\Delta\beta = 2.5\beta_0$. Open circles denote the case with tilt angle $\alpha = 0$, filled circles with $\alpha = 0.5\lambda_0$.

eigensolution of the diffusion equation is given by

$$\tau_l = \frac{R_\star^2}{\eta l(l+1)}, \tag{2.7}$$

so that for features of the size corresponding to the spherical harmonic degree l, τ_l scales with $R_\star^2$. The larger the radius of the star, the longer the lifetime of regions with the same area fraction. The presence of large-scale flows modifies the simple quadratic dependence of decay time on the stellar radius in Eq. (2.7), and prevents us from simply rescaling. We substitute the radius of the active component of HR 1099 (3.3 $R_\odot$), its observed differential rotation rate, ($\Delta\omega = 1.21$ deg day^{-1}), and the solar-like meridional flow (Eq. 2.5) into the flux transport simulation. The imposed BMR emerges at a latitude of 40°; its initial fractional area is 0.008 (323 square degrees), and the tilt angle is 20°. The resulting lifetime is about 290 days (≈ 9.5 months), which must be compared to the value of 55 days (≈ 2 months) for $R = R_\odot$ for the same fractional area and the solar differential rotation profile. Scaling with $R_\star^2$ would give $55 \times 3.3^2 \approx 600$ days (1.6 years). The difference between the calculated lifetime and the diffusion time scale is due mainly to the surface differential rotation, which reduces the characteristic length scales of the BMR. Therefore, the rate of diffusion increases with time, compared to the constant rate in the absence of large-scale flows.

For a BMR of the same size, but starting at $\lambda_0 = 70°$, the evolution with the same transport parameters leads to a lifetime of about 2 years, as shown in Fig. 2.10. Therefore,

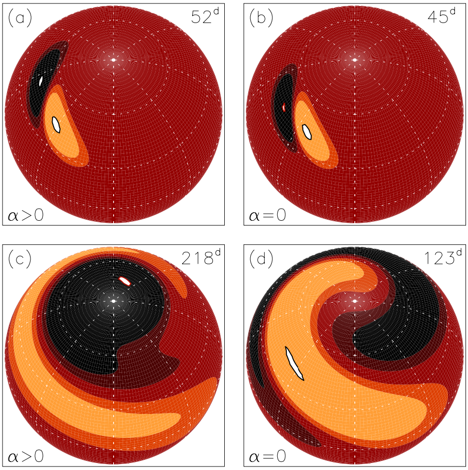

Figure 2.8: Magnetic field distributions for relatively small (a,b) and very large (c,d) BMRs (area fractions 0.008 and 0.12 of the stellar surface area), emerged at 40° with tilt (a,c) and without tilt (b,d). The snapshots for each of the four cases represent the moment shortly before the peak field strength falls below the threshold. The number of days since the bipole emerged is given in each frame. Colours and contours are the same as in Fig. 2.3. Non-zero tilt yields longer lifetimes, particularly so for a very large BMR which eventually forms a polar cap (panel c).

the long lifetimes of polar spots on RS CVn-type active stars can possibly be related to the low rate of shear at the polar regions of (sub)giant stars and a poleward-decelerating meridional flow, particularly if the BMRs emerge at high latitudes and are strongly tilted.

2.3.3 Emergence of multiple bipoles

We have shown in Sec. 2.3.1.2 that when a polar cap of one polarity is developed, its decay is significantly slower than for the lower latitudes. The example case shown in Fig. 2.8c yields a lifetime of about 7 months. Now, in the course of its evolution, we let six more bipoles of fractional area 0.03 to emerge at a latitude of 60°, at random longitudes and random times within a period of 500 days (1.4 years). This high-latitude temporary "activity belt" extends the lifetime of the polar spot to about 2.4 years (see the animation at `http://www.solar-system-school.de/alumni/isik_movies/dwarf.mpg`). The enhancement of lifetime by means of newly emerging bipoles does not depend on when the random emergence period begins within the lifetime of the already existing polar BMR.

In the case of the subgiant star of Sec. 2.3.2, the lifetime of a polar spot is a factor of about $(R_\star/R_\odot)^2$ longer than the one having the same fractional area on a solar-radius

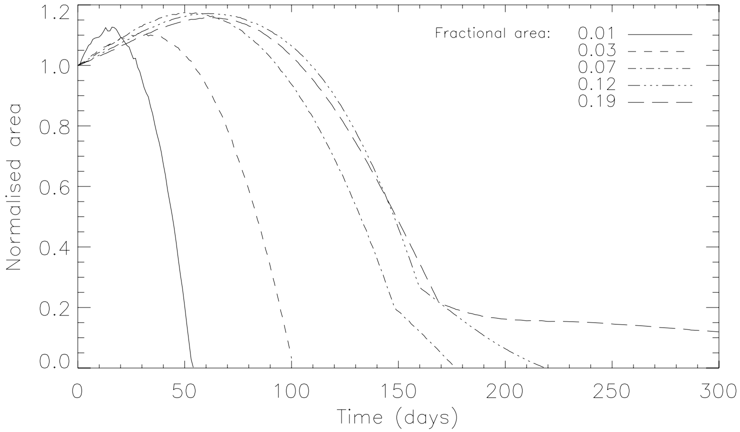

Figure 2.9: Comparison of the variations of area with time for tilted BMRs of different sizes, all emerged at $\lambda_0 \approx 40^\circ$. The area values normalised to the initial values indicated in the legend (in units of the solar surface area). As the initial size increases, a rapid change in the decay rate in the late phase of the evolution results from the fact that the preceding polarity region falls below the detection threshold and the follower polarity, being closer to the rotational pole, lives longer. The larger the initial size, the larger is the polar cap formed by the follower polarity region.

star. The lifetime of a unipolar polar cap of fractional area 0.004 ($\beta_0 = 4^\circ$) is about 3 years on the subgiant star, compared to about 0.3 years on the dwarf. Random emergence of six bipoles of fractional area 0.03 during 500 days (1.4 years) at λ_0=60° prolongs the lifetime of the polar spot to about 10 years (see the supplementary animation at `http://www.solar-system-school.de/alumni/isik_movies/subgiant.mpg`).

2.4 Structure of starspots

It is not known whether the observed starspots are monolithic structures or conglomerates of smaller spots. In addition, the only general information available regarding their evolution are lifetime estimates, indicating values of less than one month at mid-latitudes of rapid rotators (Hussain 2002). Here we compare different possible configurations for starspots or starspot groups of sizes comparable to those observed at mid-latitudes of rapid rotators. Sunspots and their clusters with relatively long lifetimes are unipolar features. Therefore, in contrast to the BMR simulations presented above, we now consider starspots to be unipolar regions, with the other polarity placed on the opposite hemisphere, in order to conserve the total flux on the surface. We also assume that the diffusion rate of a

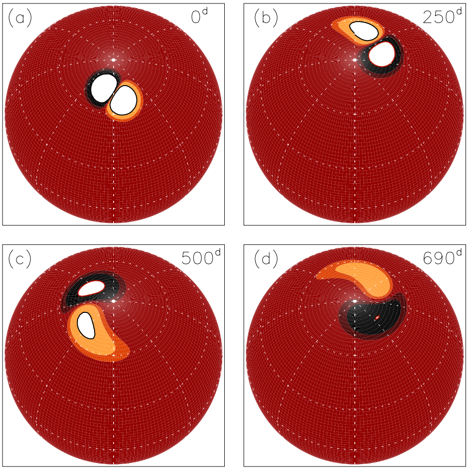

Figure 2.10: Evolution of a polar BMR with $\beta = 4°, \Delta\beta = 10°$, starting at $\lambda_0 = 70°$ on a star with a radius of $3.3R_\odot$. The effects of weak differential rotation ($\Delta\omega$ = 1.21 mrad day^{-1}) and the same meridional flow profile and magnetic diffusivity as in the solar case are considered. The large stellar radius and the weak surface shear at high latitudes of the star lead to a lifetime of about two years. Since the meridional flow ceases at 75°, The BMR is not completely drifted up to the rotational pole.

starspot is reduced compared to the case of a BMR, which consists of spots, plages, and ephemeral regions. The reason is that the strong and coherent magnetic fields in a starspot can suppress convection, as in the case of sunspots. This effect is represented in our simulations by choosing a magnetic diffusivity that is much lower than the value adopted for BMR evolution. The observed decay rates of sunspots correspond to a diffusivity of 10-50 km^2 s^{-1} (Martínez Pillet et al. 1993). We adopt a value of η = 50 km^2 s^{-1} for the starspot simulations. In the following, we describe simulated scenarios in the presence and absence of large-scale flows in order to discriminate between the effects; we consider monolithic and cluster structures as well as two BMR-like models to compare their evolution. All configurations harbour the same amount of total magnetic flux (1.52×10^{22} Mx). The cases are described in Table 2.1.

The threshold field strength which determines the observable flux is taken to be 0.14 times the initial peak field strength. Fig. 2.11 shows the evolution of magnetic flux at a field strength above the threshold, normalised to its initial value. In case 1, the flux decays nearly linearly in time, while for case 2 (the same monolithic spot, but with large-scale flows) the decay is not linear in time, because the surface shear and the meridional flow modify the length scale of the spot. For large-spot cluster cases, with and without flows (cases 3 & 4), the initial decay is much faster than in the other cases: the conglomerate structure contains smaller flux elements, which diffuse faster than the group as a whole.

Table 2.1: Configurations for starspots

Configuration	Fractional area	Large-scale flows[a]	η (km^2 s^{-1})
Monolithic spot	0.005	−	50
Monolithic spot & flows	0.005	+	50
Cluster of large spots	0.006	−	50
Cluster of large spots & flows	0.006	+	50
Cluster of small spots[b]	0.05[c]	+	50
Passive BMR[d]	0.05	+	600

---

[a] Solar-like differential rotation and meridional flow (− if absent, + if present).

[b] The spots are not individually followed, but represented by a weak (25 G) unipolar magnetic field under the influence of large-scale flows.

[c] Including both magnetic and non-magnetic regions

[d] A completely passive flux distribution, similar to the BMR simulations shown in Sect. 2.3.

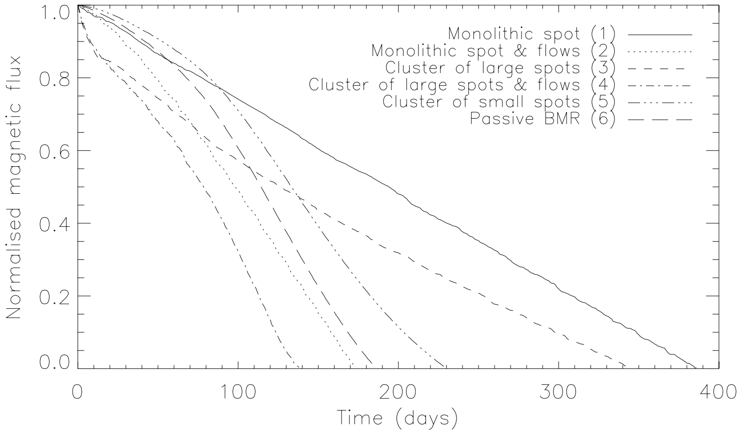

Figure 2.11: Evolution of magnetic flux of the area above the threshold field strength of $0.14B_0$ normalised to the initial value ($\sim 10^{22}$ Mx), for six different flux configurations, all of which are started at $\lambda_0 = 50^\circ$ (see main text).

The situation is shown in Fig. 2.12: For case 3, once the spots coalesce to a more diffuse patch, the effective length scale becomes larger so that the decay rate is reduced and the subsequent evolution takes place largely with the same rate as for the circular, monolithic region (case 1). When flows are introduced (case 4), the cluster of large spots decays much faster owing to the decrease of length scale by differential rotation. For cases 5 & 6, the evolutions are similar to each other, since they differ only in magnetic diffusivity. In general, the effect of flows for the cases 2 and 4-6 leads to shorter lifetimes and nonlinear flux decay (for field strength above the threshold), whereas the lack of flows leads to

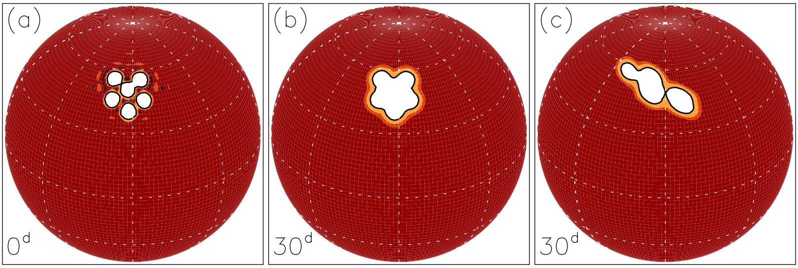

Figure 2.12: Magnetic field evolution for a cluster of unipolar magnetic regions, with $\eta = 50$ km^2 s^{-1} (cases 3 & 4). (a) The initial field distribution, (b) the field distribution 30 days after the emergence, without large-scale flows (case 2), (c) the field distribution 30 days after the emergence, with solar-like large-scale flows (case 3).

longer lifetimes and linear decay for the cases 1 and 3.

The linear decay of flux for the monolithic spot without flows can be understood through a simple analytical model. Consider the diffusion of a scalar field B, which is initially distributed with axial symmetry on a plane. For simplicity we neglect the curved surface on the sphere, which is appropriate as long as $R_{\rm spot} \ll R_\star$. We write the diffusion equation in cylindrical polar coordinates (r, θ, z) for an axisymmetric field of strength B along the z-direction as

$$\frac{\partial B}{\partial t} = \eta \left(\frac{\partial^2 B}{\partial r^2} + \frac{1}{r}\frac{\partial B}{\partial r} \right), \tag{2.8}$$

where η is the magnetic diffusivity. Assuming an initial field with a Gaussian profile,

$$B(r, t = 0) = B_0 \exp\left(\frac{-r^2}{R_0^2} \right), \tag{2.9}$$

a self-similar solution of the following form can be written as

$$B(r, t) = \frac{\Phi_{\rm 0T}}{\pi R^2(t)} \exp\left(\frac{-r^2}{R^2(t)} \right). \tag{2.10}$$

Here $\Phi_{\rm 0T} = \int_0^\infty \int_0^{2\pi} B(r, 0) r d\theta dr = \pi R_0^2 B_0$ is the total magnetic flux as the conserved quantity and $R(t) = (4\eta t + R_0^2)^{1/2}$ represents the characteristic length scale, which varies with time, so that the diffusion time-scale $\eta / R^2(t)$ also is a function of time. Integrating the flux density of the area with field strength above a threshold level f (taken as 0.14 in our simulations), we find the time-dependent flux above the threshold as

$$\Phi(t) = \Phi_0 \left(1 - \frac{4 f \eta t}{(1 - f)\, R_0^2} \right), \tag{2.11}$$

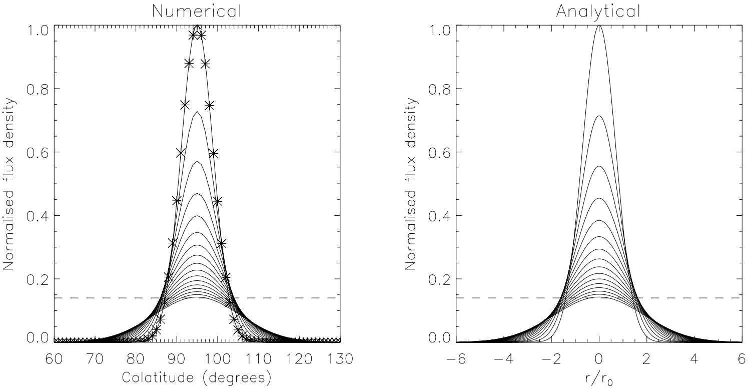

Figure 2.13: Radial profiles of magnetic flux density in the course of diffusion, for the numerical simulation (left), and the analytical solution (right). Dashed lines denote the threshold level which is used to define the boundary of the unipolar region. Asterisks show the values of the initial field distribution in the numerical solution and the continuous line shows the Gaussian fit.

where $\Phi_0 = \Phi_{0T}(1 - f)$ is the initial value. The linear decrease of the flux in Eq. (2.11) is reproduced in the numerical simulation of the monolithic spot case 1 in Fig. 2.11. A comparison of the analytically and numerically calculated profiles is shown in Fig. 2.13. Taking the initial characteristic radius R_0 as the width σ of the initial Gaussian profile of the numerical simulation, the lifetime of the enclosed region is 1623 days (about 1.5 diffusion time scales) from Eq. 2.11, in good agreement with the numerical simulation for $\eta_r = 0$.

2.5 Discussion

We have made numerical simulations of the surface transport of bipolar magnetic regions and starspots in various configurations, all regarded as purely radial magnetic fields with Gaussian initial profiles. Lifetimes calculated here are for isolated bipolar regions and unipolar spots or spot groups. In general, emergence of other bipoles at or around the location of an existing bipolar region can lead to a complete change of the spot distribution, which can be interpreted as the disappearance of a spot. This means that the real lifetimes should be lower to some extent which is determined by the emergence rate of BMRs. The estimated lifetimes of mid-latitude BMRs are in accordance with the estimated decay time of stellar active regions based on Ca II H & K observations (Donahue et al. 1997) and Doppler imaging of rapid rotators (Barnes et al. 1998, Hussain 2002, Kővári et al. 2004). Very low correlations between observations recorded a month apart set an upper limit for the lifetimes of low- to mid-latitude magnetic regions on rapid rotators (see Hussain 2002). When considered together with our simulations (assuming that the transport parameters for a rapidly rotating G-K dwarf are similar to the solar values), the observed lifetimes of 1 month also set an upper limit on the *sizes* of BMRs to be 10°-20° in angular diameter, or about 1% of the total surface area for a star with $R = R_\odot$. Our simulations for such a star indicate that the differential rotation within the observed range of values for AB Dor does not have a very significant effect on BMR lifetimes. Varying the surface shear or the emergence latitude changes the lifetimes by less than a month. We note that the simulations which were run without the meridional flow has shown that the absence of such a flow shortens the lifetime of a high-latitude BMR by only a few days. Therefore, the meridional flow does not disturb the above mentioned result. The differences in lifetimes for different emergence latitudes are caused by the flow pattern on the surface:

1. Stronger surface shear in mid-latitudes leads to lifetimes that are about 20 days ($\approx$ 30%) shorter than those for low (10°) and high (60°) latitudes.

2. The sign and the amplitude of the gradient of the meridional flow velocity also has an effect upon lifetimes. The presence of a diverging flow at low latitudes and a converging flow at high latitudes leads to shorter and longer lifetimes, respectively. In addition, meridional flow advects low-latitude BMRs to regions with stronger shear, thus the lifetime is shortened. It also advects the mid-latitude BMRs to higher latitudes with weaker shear, and this prolongs the lifetime. For instance, the lifetime of a BMR emerged at 60° latitude is 15 days longer than the one emerged at 30° latitude. This is the case for both of the AB Dor surface shear values. Hence, high-latitude BMRs live longer than low-latitude ones, even when the local surface shear is the same. In our model, this is caused only by the meridional flow.

BMRs which are larger than those discussed above live longer, and this tendency is substantially increased when a tilt angle according to the relation $\alpha = 0.5\lambda_0$ is assumed. For instance, a polar cap forms about six months after the emergence at 40° of a BMR initially covering 12% of the stellar surface. Once such a “polar spot” is formed, it will not be significantly affected by differential rotation because of its roughly circular shape and circumpolar boundaries. When there are more BMRs with the same polarity orientation, emerging at e.g. 60° latitude, we have shown that the lifetime of the polar spot is prolonged significantly.

For (sub)giant stars we find that BMRs emerging at high latitudes can persist as polar spots for more than 2 years. This is caused by the large radius of the star and the meridional flow pattern, which is assumed to be decelerating with latitude for $37° < \lambda < 75°$. Furthermore, during the evolution of a polar cap, emergence of new BMRs at high latitudes may inject fresh flux of follower polarity and this can lead to a longer persistence of the polar cap. This can possibly explain the observed polar spots with very long lifetimes (cf. Hussain 2002).

In summary, we suggest that the observed long lifetimes for polar spots in both dwarf and giant stars are likely to be caused by

1. high-latitude emergence of BMRs, as indicated by the numerical simulations of rising flux tubes (Schüssler et al. 1996, Granzer et al. 2000),

2. supply of follower-polarity flux by transport from mid-latitudes,

3. weak differential rotation near the poles, and its inefficiency in disrupting polar magnetic regions,
4. the possibility of small turbulent magnetic diffusivity, owing to larger supergranules in subgiant atmospheres.

The possibility (2) has been considered by Schrijver and Title (2001), whose simulations show the formation of a unipolar ring of spots surrounding an opposite-polarity polar cap on a highly active solar analogue. Process (1) was also studied in the simulations by Mackay et al. (2004), resulting in the intermingling of opposite polarity regions near the poles, owing to emergence at high-latitudes and an assumed meridional flow amplitude about 10 times larger than the solar value.

It is not obvious how to describe starspots and spot clusters in the framework of a linear surface flux transport model. Extrapolations of spot areas to stars more active than the Sun (Solanki and Unruh 2004) indicate that a large fraction of the observed starspots are smaller than the resolution limits of Doppler imaging maps and thus might be missed on existing reconstructions. These authors further suggest that, provided the spot areas are lognormally distributed, it is likely that the observed spots on RS CVn stars are actually conglomerates of smaller spots. Our simulations of starspots indicate that a large monolithic spot (case 1 in Sec. 2.4) and a similar-sized cluster of large spots (case 3) have similar lifetimes. Thus they do not favour either of the two configurations. In the cases 1 and 3, the magnetic flux of the region above the threshold field strength decreases linearly with time. We have demonstrated that this is a natural consequence of the two-dimensional diffusion of a scalar quantity with a Gaussian initial profile, when a region above the detection threshold of the quantity is considered.

We have treated the configuration and transport of a unipolar spot/cluster in a number of other ways, all chosen such that the total flux is kept the same. As a variant of case 3, we considered the effects of solar-like differential rotation and meridional flow on a cluster of large spots (case 4). The resulting lifetime turned out to be strongly reduced in comparison to the case without large-scale flows. In the initial phase, the individual spots expand rapidly because of their relatively small sizes. After their coalescence, the general evolution pattern becomes similar to that of the case 2, in which the evolution of a monolithic spot is studied in the presence of large-scale flows. Furthermore, we have considered a region (case 5) with an area about 10 times larger than a monolithic spot having the same magnetic flux. This is a very simple representation of a cluster of small starspots on a large area. This configuration has an intermediate lifetime, between that of the large-spot cluster with flows (case 4) and of the one without flows (case 3). In summary, the numerical simulations presented in Sec. 2.4 indicate that the lifetime of a unipolar spot or spot cluster can differ by a factor of about 2.5 depending on the assumed initial flux configuration and the effects of large-scale flows.

Hall and Henry (1994) give lifetimes for starspots of various angular sizes based on their photometric light curve analysis. We compared their lifetime estimates with the results of our simulations. We have selected the main sequence G-K type single and binary stars (5 stars/systems in total) from their sample. In Fig. 2.14 we give the comparison. Both sets of data are roughly consistent with each other. Hall and Henry (1994) suggested two “laws” for starspot lifetimes, based on long-term photometric observations on a sample of active main sequence, subgiant, and giant stars of spectral types G, K, M. For

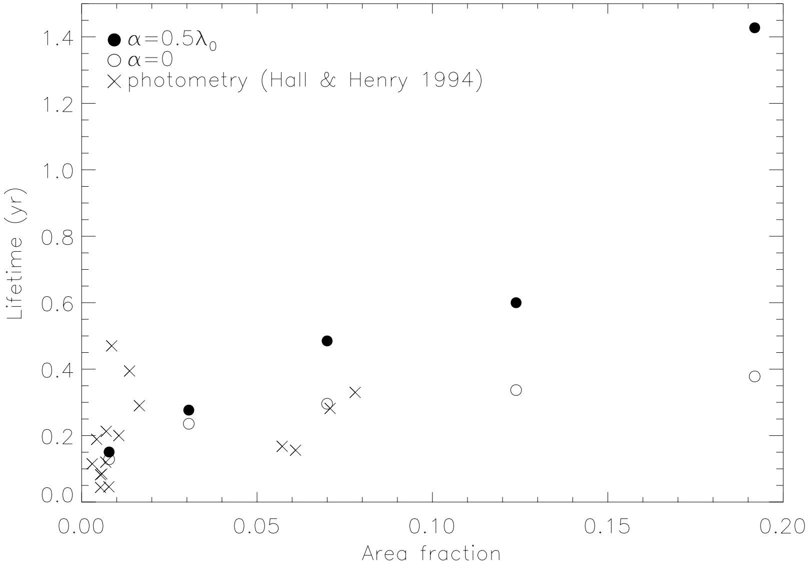

Figure 2.14: Comparison of lifetime estimates of our simulations for different areas with photometric results of Hall and Henry (1994).

very large spots, they assume that the lifetime is determined by shearing due to differential rotation, such that the spot lifetime is assumed to be inversely proportional to spot radius and differential rotation coefficient. In the second relation, the lifetime is proportional to spot radius and stellar radius; it is thought to apply for relatively small spots which have lifetimes shorter than the disruption time scale of differential rotation. Since they do not give error bars for spot sizes and lifetimes, we only take the data at the face value. Their plots are logarithmic in both axes and the stellar sample covers stars with very different radii and starspots probably at different latitudes (the data do not include information on the latitudes of the spots). Different stellar radii can cause a spread in lifetimes to within an order of magnitude, considering the $R_\star^2$- dependence mentioned in Sec. 2.3.2 and the weaker surface shear. Sources of error in the area calculation based on brightness changes can also include the fact that there is not only one big starspot but a cluster of spots with different sizes and lifetimes. Moreover, another spot might emerge within the lifetime of the other, which would cause errors in both the area and the lifetime. As a result, one cannot necessarily assume an individual coherent structure that is having such a lifetime. According to the test models made by Eker (1999), a photometric signal with an amplitude of about 0.15 mag, for light curves which are accurate by ±0.005 mag in brightness and by ±0.005 in the linear limb-darkening coefficient, the uncertainty of the spot size is comparable to the size itself.

We suggest that if the observed wave-like distortion in light curves can be caused by large spot conglomerates, differential rotation can disperse the group of relatively small spots over a large area so that the initial photometric signal (wave-like distortion seen in the light curves) would cease, but the individual spots can still survive without being detected, having lifetimes proportional to sizes. Emergence of new spots may complicate the situation even further. Taking into account the fact that unique solutions of spot distributions using light curves are in many cases not possible, the rotational modulation of activity indicators as well as the patches in Doppler maps can indicate different substructures for spot configurations such as those considered in the simulations in Sect. 2.4.

Vogt et al. (1999), using Doppler images of HR 1099 spanning 11 years, showed that the “migrating photometric wave” is not caused simply by longitudinal migration of spots on a differentially rotating star but rather to changes in the spatial distribution of a few spots that emerge and then disappear, at the same mean longitude. The same authors also tracked two long-lived spots and showed that they emerged at mid-latitudes and migrated upwards to merge with the polar spot. They report a weak but anti-solar differential rotation (poles rotating more rapidly than the equator), contrary to our model assuming a solar-like differential rotation. However, one can obtain a long lifetime provided that the magnetic flux concentrates in a circular polar cap of radial field, regardless of the strength and the pattern of differential rotation. Our simulations also indicate that additional flux from tilted BMRs emerging at mid-latitudes can always be transported by the meridional flow to feed the polar cap flux. In Sec. 2.3 we have shown that a large tilted BMR emerging at an intermediate latitude is transported by meridional flows and a solar-like differential rotation to form a polar spot. We have also shown that the follower-polarity flux from tilted BMRs emerging randomly in time and longitude, at mid- to high latitudes can feed an already existing polar spot with additional flux.

The simulations of surface magnetic flux transport presented in this chapter let us draw the following conclusions.

- The lifetime of a single, isolated bipolar magnetic region on a rapidly rotating star of solar radius is of the order of a few months, depending on the emergence latitude and the strength of surface shear.

- The combined effects of diffusion and high emergence frequency are responsible for the short lifetimes of starspots and stellar magnetic regions at low and mid-latitudes.

- Polar spots originate from the follower polarities of single or multiple tilted bipolar regions, emerging at mid- or high latitudes. A polar spot can be maintained by high-latitude emergence of new bipoles having the same polarity orientation.

- Polar caps of evolved stars have lifetimes proportional to $R_\star^2$. For low-latitude regions, shorter lifetimes result from an increase of the diffusion rate due to differential rotation.

- We find no clear indication as to whether large starspots are monolithic or clusters of smaller spots. The flux decay strongly depends on the details of the interaction between surface magnetic fields and large-scale flows, and the nature of turbulent diffusion.

3 Effects of external flows on thin magnetic flux tubes

The spatio-temporal organisation of solar magnetic field at large scales requires a mechanism for the generation, storage, and emergence of magnetic flux. In the present chapter, I will consider some aspects of magnetic flux storage in the overshoot region at the bottom of the solar convection zone. The central problem is whether magnetic flux tubes with field strengths on the order of $10^4 - 10^5$ G can be stored under the influence of external flows in the overshoot region, for times of the order of a few years. For the storage of such flux tubes which contain fluxes comparable to large bipolar magnetic regions on the Sun ($\sim 10^{22}$ Mx), the entire convection zone and the radiative core are not suitable locations. The reasons can be summarised in the following points:

1. Consider a horizontal magnetic flux tube in the superadiabatically stratified convection zone. If it is in thermal equilibrium with the surroundings, it suffers a net upward buoyancy force owing to the lateral pressure balance. Even if the tube is initially not buoyant (i.e., when it is cooler than its surroundings), the superadiabatic temperature gradient of the ambient medium would lead to a convectively unstable state. For instance, when an external perturbation drags a flux tube upward, the entropy difference between inside and outside the tube increases, owing to the negative entropy gradient of the ambient medium. Because of the excess entropy of the medium inside, the tube continues to rise.

2. In the upper parts of the radiative core, even though a strong toroidal field may, in principle, be generated by velocity shear, it cannot escape, because of the highly stable stratification. Therefore, it is not likely to be responsible for the formation of magnetic regions on the surface.

The most likely location for the flux storage is the overshoot region below the convection zone, where the subadiabatic stratification and overshooting convective downdrafts may compensate for the magnetic buoyancy for a time comparable with the cycle length. Furthermore, a toroidal flux tube can reach a mechanical equilibrium as a consequence of its buoyant rise and the magnetic tension force leading to poleward drift (Moreno-Insertis et al. 1992). In mechanical equilibrium, the tube has neutral buoyancy, so the curvature force is balanced by the Coriolis force induced by a prograde flow along the tube, relative to the rest frame of the ambient medium.

Ferriz-Mas and Schüssler (1995) have studied the linear stability of thin toroidal magnetic flux tubes at the bottom of the solar convection zone with arbitrary field strength and latitude, under the effects of nonaxisymmetric linear perturbations. They have obtained the stability properties of flux tubes as a function of latitude, field strength, and the location in the convective overshoot region (see Fig. 3.7). Toroidal flux tubes located in the overshoot region are subject to undulatory (Parker-type) instabilities with growth times (e-folding time) of less than one year, for $B \gtrsim 10^5$ G. This indicates that, in the linear regime, flux tubes with field strengths on the order of 10^4 G may be stored in the overshoot region for sufficiently long times in the course of the dynamo cycle. The time that it takes for the velocity shear in the solar tachocline to wind up the poloidal magnetic field into a toroidal (azimuthal) field is on the order of a few years. Parker-unstable tubes with growth times longer than this time may contribute to the magnetic flux reservoir in the overshoot region.

There may be other possibilities which may lead to rising flux tubes at times shorter than one year. Apart from the case of linear (first order) perturbations discussed above, *finite* perturbations caused by external flows may introduce nonlinear effects, which may lead to flux tube eruption. The reason is that, while the stratification of the overshoot region is subadiabatic ($\nabla < \nabla_{\rm ad}$) and stable to convection, the *superadiabaticity*, $\delta = \nabla - \nabla_{\rm ad}$, increases by about 5 orders of magnitude from the lower boundary ($\delta \sim -9 \cdot 10^{-2}$) to the upper boundary ($\delta \sim -5 \cdot 10^{-7}$) of the overshoot region, according to the model of Skaley and Stix (1991). Caligari et al. (1998) have investigated the effect of a local upflow on a linearly stable flux tube in mechanical equilibrium near the bottom of the overshoot region. They found that an upflow with velocities between 20-50 m $\rm s^{-1}$ and a flux tube with an initial field strength of 10^4 G, can trigger a nonlinear Parker instability, in the form of a rising loop, which reaches up to the surface within one year. At the first stages of its evolution, the loop reaches a state of dynamical force equilibrium. A subsequent downflow along the tube increases buoyancy at the top of the loop, so that it continues to rise. Because the drag force per unit volume of the tube exerted by the initial upflow is inversely proportional to the tube radius, a thinner tube is more likely to erupt, provided that the radial extent of the upflow is comparable with the local pressure scale height. For a magnetic field strength of $6 \cdot 10^4$ G, which is about half the critical value for linear Parker instability, the buoyancy force overcomes the magnetic curvature force, by means of a downflow from the crest of the loop, leading to an eruption within one year. However, the authors estimate an average upflow velocity using the model by van Ballegooijen (1982), and it is about an order of magnitude less than the velocities that they found for the nonlinear Parker instability. This indicates that convective flows are not likely to trigger eruption within one year for linearly stable flux tubes in the overshoot region.

Schüssler and Ferriz Mas (2007) have made a linear stability analysis to investigate the effect of flows perpendicular to the axis of a horizontal thin flux tube, which was chosen to be in equilibrium in the lack of external flows. They found monotonic and oscillatory instabilities for flow velocities on the order of the Alfvén velocity, and for wavelengths (along the flux tube) much smaller than those found in the case of linear Parker instability (in which external flows are not taken into account). They found two effects of the external flows which cause instabilities: 1) perturbations of the external pressure stratification by the inertial force (which is caused by the tube carrying material around it), 2) changes of the hydrodynamic drag force in the course of the displacement of the tube from its equilibrium position.

Holzwarth et al. (2007) have studied the effects of field-aligned flows for a horizontal flux tube in the overshoot region. When the drag force is taken into account in terms of a Stokes-type friction, which is linear in perpendicular velocity, they found that field-aligned flows above a critical speed lead to overstability of transverse waves propagating along the tube. They found that this friction-induced instability can develop for arbitrarily small flow speeds near the limit of Parker instability.

The studies mentioned above indicate that fluid flows in and around flux tubes have to be considered when discussing magnetic flux storage in the overshoot layer. A critical question in this respect is whether an external flow within the expected range of convective velocities may eventually lead to a buoyancy instability of the flux tube with a growth time on the order of less than a few years. This chapter is devoted to an extensive investigation concerning the effects of external flows on thin toroidal flux tubes is needed in order to quantify the effects of flows in the region where magnetic flux is stored for the operation of the dynamo.

In the following, I will consider the deformation of toroidal flux tubes subject to perpendicular flows, in order to derive relations between the properties of the tube, the flow, and the resulting displacement (Sect. 3.1). The relations provide information about how much the flux tube would be dragged by a perpendicular flow with a given velocity distribution. In Sect. 3.2, I present numerical simulations which show that nonlinear Parker instability can be trigerred when the perturbation amplitude is larger than a critical level. The growth time of both the nonlinear and friction-induced instabilities are proportional to the amplitude of the initial perturbation. Finally, I will investigate the behaviour of the friction-induced instability (Holzwarth et al. 2007) in the nonlinear regime by numerical simulations (Sect. 3.2). I will determine an approximate value for the velocity of the perpendicular flow, which allows for the storage of the flux tube for a few years before the instabilities develop.

3.1 Deformation of flux tubes by perpendicular flows

In this section, I discuss the stationary equilibrium properties of toroidal flux tubes which are deformed by perpendicular flows. The aim is to study under which conditions the deformation becomes large enough, so that parts of the flux tube would enter radiative and/or convective zones. If the flux tube hits the radiative core, a slingshot-like effect may occur, in which the trough of the tube becomes highly buoyant and is ejected upwards. If a part of the tube enters the convection zone, the crest of the tube may be destabilised owing to relatively large superadiabaticity. The goal here is to test these possibilities (Sect. 3.1.1-3.1.2). In addition, the question of how much a flux tube is displaced from its equilibrium position by the external flows as a function of magnetic flux will be considered in Sect. 3.1.3.

I consider a toroidal flux tube located in the convective overshoot region between the convection zone and the radiative interior. For the stratification of the ambient medium, a model convection zone developed by Skaley and Stix (1991) is considered, which uses a non-local treatment of convection as described by Shaviv and Salpeter (1973). In the model, the overshoot region extends about 10^4 km below the base of the convection zone, which is defined as the depth at which the convective energy flux becomes zero (changes its sign), at about $r = 512$ Mm (see Sect. 1.4). In the present chapter, the terms “bottom”, “middle”, “top” of the overshoot region are used to refer to the radial positions at, respectively, 2000, 5000, and 8000 km above the lower boundary of the overshoot region, which is at the radius of $r = 502$ Mm ($\sim 0.72 R_\odot$).

In order to determine the conditions under which a deformed flux tube reaches the convective or radiative zones, I consider an azimuthally periodic flow perpendicular to each mass element of the flux ring. In the following, I will derive relations between the flow velocity amplitude and the maximum displacement of the tube from its equilibrium state, corresponding to ranges of values for the tube thickness, magnetic flux density, and the azimuthal wavenumber in case of an azimuthally periodic flow.

A general linear stability analysis of thin magnetic flux tubes of toroidal geometry at the bottom of solar convection zone was done by Ferriz-Mas and Schüssler (1993) for the equatorial plane and by Ferriz-Mas and Schüssler (1995) for tubes outside the equatorial plane. They take the equations for mass conservation, magnetic induction, momentum, and the condition for lateral pressure balance for a thin flux tube and apply to them first-order perturbations in the Lagrangian reference frame. The resulting equations are linearised. Since the ratio of gas pressure p to magnetic pressure $B^2/8\pi$, called β, is much larger than unity in the lower convection zone, the equations are rewritten in the limit $\beta \gg 1$. Rigid internal rotation is assumed for the Sun. I first consider a toroidal flux tube in the equatorial plane, and then the more general case outside the equatorial plane. I use a frame of reference rotating with the angular velocity of the flux tube in stationary equilibrium, $\mathbf{\Omega}$, whereas the angular velocity of the external medium is $\mathbf{\Omega_e}$.

For stationary equilibrium of a flux ring in the equatorial plane, the azimuthal and latitudinal components of the momentum equation vanish identically. Assuming neutral buoyancy[1], the radial component yields

$$\frac{B_0^2}{4\pi R_0} - \rho_{i0} r_0 (\Omega^2 - \Omega_{\mathrm{e}0}^2) \quad = \quad 0, \tag{3.1}$$

where R_0 is the distance from the solar rotation axis, ρ the density, r the distance to the centre of the Sun. The index i stands for the quantities inside the flux tube, while e stands for the external values. “0” means the equilibrium value for a given quantity. Eq. 3.1 shows that the magnetic curvature force and rotationally induced forces must balance each other, requiring $\Omega \geqslant \Omega_{e0}$.

I consider the drag force per unit volume exerted by a steady flow of velocity $v_\perp$ perpendicular to a straight cylinder,

$$F_{\mathrm{D}} = -C_{\mathrm{D}} \frac{\rho_{e0} v_\perp^2}{\pi R_{\mathrm{t}}}, \tag{3.2}$$

where C_D is the hydrodynamic drag coefficient which is taken to be unity (because of the assumed cylindrical shape of the flux tube and the high Reynolds number) (Batchelor 1967), ρ_{e0} is the equilibrium value of the external density, and R_{t} is the cross-sectional radius of the tube.

---

[1] This condition is strictly required for the mechanical equilibrium of a flux tube outside the equatorial plane.

3.1.1 Flux tubes in the equatorial plane

In order to obtain relations between the flow velocity and the resulting displacement, I consider the linearised equations of motion for perturbations $(\xi_R, \xi_\phi, \xi_\lambda)$, where R is the distance from the rotation axis, ϕ is the longitude, and λ is the latitude. Here, only radial and azimuthal components (perturbations in the (R, ϕ) plane) are considered, because the equation for the latitudinal component is decoupled in the equatorial plane. Following Ferriz-Mas and Schüssler (1993), the linearised equations of motion for the perturbations in the (R, ϕ) plane read

$$\begin{aligned} \tau^2\left(\ddot{\xi}_R - 2\Omega\dot{\xi}_\phi\right) &= 2f^2\frac{\partial^2\xi_R}{\partial\phi_0^2} - 4f\left(f - \frac{1}{2\gamma}\right)\frac{\partial\xi_\phi}{\partial\phi_0} + T\xi_R, &(3.3)\\ \tau^2\left(\ddot{\xi}_\phi + 2\Omega\dot{\xi}_R\right) &= 2f^2\frac{\partial^2\xi_\phi}{\partial\phi_0^2} + 4f\left(f - \frac{1}{2\gamma}\right)\frac{\partial\xi_R}{\partial\phi_0}, &(3.4)\end{aligned}$$

where

$$\begin{aligned} T &= 2(\sigma-1)f^2 + \frac{4}{\gamma}f - \frac{2}{\gamma}\left(\frac{1}{\gamma} - \frac{1}{2}\right) + \beta\delta + \tau^2(\sigma-1)(\Omega_{e0}^2 - \Omega^2), &(3.5)\\ \tau &\equiv \left(\frac{\beta H_p}{g_0}\right)^{1/2} = \sqrt{2}\frac{H_p}{v_A}, &(3.6)\\ f &\equiv \frac{H_p}{R_0} = \frac{p_{i0}}{g_0\rho_{i0}R_0}, &(3.7)\\ \beta &\equiv \frac{8\pi p_{i0}}{B_0^2}. &(3.8)\end{aligned}$$

The meanings of the various symbols in the above equations are as follows. H_p is the local pressure scale height, δ is the superadiabaticity, p_{i0} and ρ_{i0} are the equilibrium values for the pressure and density inside the tube, respectively, r_0 is the spherical radial position of the equilibrium tube, Ω and Ω_{e0} are, respectively, the angular velocities of the plasma in the tube and the external medium, v_A is the Alfvén velocity, B_0 is the magnetic field strength and g_0 the gravitational acceleration with a radial dependence $g \propto r^\sigma$, where σ is taken to be -2, which means that the small contribution of the mass inside the convection zone is neglected. I consider a deformation of the flux tube by the drag force, Eq. (3.2), owing to a perpendicular flow with a velocity amplitude $v_\perp$, assuming that a force balance (dynamical equilibrium) results, which can be described by the stationary parts of Eqs. (3.3)-(3.4). The resulting equations of motion for stationary equilibrium (steady state) in the (R, ϕ) plane read

$$\begin{aligned} 2f^2\frac{\partial^2\xi_R}{\partial\phi_0^2} - 4f\left(f - \frac{1}{2\gamma}\right)\frac{\partial\xi_\phi}{\partial\phi_0} + T\xi_R &= \frac{-\tau^2 v_\perp^2}{\pi R_\mathrm{t}} &(3.9)\\ 2f^2\frac{\partial^2\xi_\phi}{\partial\phi_0^2} + 4f\left(f - \frac{1}{2\gamma}\right)\frac{\partial\xi_R}{\partial\phi_0} &= 0, &(3.10)\end{aligned}$$

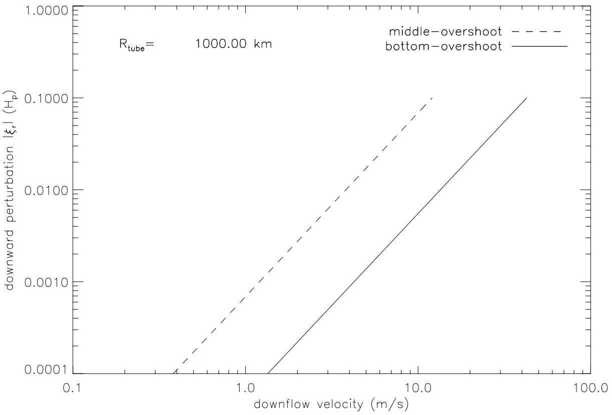

Figure 3.1: Drag-induced downward displacement (in units of the local pressure scale height) as a function of the downflow velocity at the bottom of the overshoot region (continuous line) and at the middle of the region (dashed line), respectively. The pressure scale height is about 55 Mm.

where the drag force has been multiplied by the factor τ^2/ρ_{e0} for consistency with the non-dimensionalisation of Eqs. (3.3)-(3.4). Because the drag force applies only in the direction normal to the axis of the flux tube, it only appears in the equation for the radial component (Eq. 3.9). Eqs. (3.9-3.10) correspond to the stationary equilibrium in which the drag force is balanced by the magnetic curvature force.

Axisymmetric perturbation. Consider a toroidal flux tube in the overshoot region, located in the equatorial plane. The simplest case is a perturbation caused by an axisymmetric downflow (towards the centre of the star). This is rather unlikely to be the case in the Sun, but will provide a rough estimate for the displacement of the tube as a function of flow velocity. For axisymmetric displacements, Eq. (3.10) vanishes and Eq. (3.9) yields

$$\frac{\rho_{e0} v_\perp^2}{\pi R_\mathrm{t}} = T\xi_r. \tag{3.11}$$

Fig. 3.1 shows the relation between the perturbation ξ_r and the velocity $v_\perp$, for $R_\mathrm{t} = 10^3$ km at the middle and the bottom of the overshoot region, respectively. Overshoot velocities between 1-30 m s^{-1} (van Ballegooijen 1982, Skaley and Stix 1991) lead to displacements up to the order of $10^{-3} - 10^{-2}$ H_p (55-550 km).

Nonaxisymmetric perturbations. Now I consider sinusoidal perturbations applied to toroidal flux tubes in the overshoot region. Suppose that the perturbation and its driver, the drag force have the form

$$[\xi, \mathbf{F}_\mathrm{D}] = [\hat{\xi}, \hat{F}_\mathrm{D}] \exp(im\phi_0), \tag{3.12}$$

where $\hat{F}_{\mathrm{D}} = \rho_{e0} v_{\perp}^2 / \pi R_{\mathrm{t}}$.

Substitution of Eq. (3.12) into Eqs. (3.9)-(3.10) leads to the system

$$\underbrace{\begin{pmatrix} 2f^2m^2 - T & 4f\left(f - \frac{1}{2\gamma}\right) im \\ 4f\left(f - \frac{1}{2\gamma}\right) im & -2f^2m^2 \end{pmatrix}}_{A} \begin{pmatrix} \hat{\xi}_r \\ \hat{\xi}_\phi \end{pmatrix} = \begin{pmatrix} \tau^2 v_{\perp}^2/\pi R_{\mathrm{t}} \\ 0 \end{pmatrix} \tag{3.13}$$

with the solution

$$\hat{\xi}_r = \frac{-1}{\det A} 2f^2m^2 \frac{\tau^2 v_{\perp}^2}{\pi R_{\mathrm{t}}} \tag{3.14}$$

$$\hat{\xi}_\phi = \frac{-1}{\det A} 4f\left(f - \frac{1}{2\gamma}\right) im \frac{\tau^2 v_{\perp}^2}{\pi R_{\mathrm{t}}} \tag{3.15}$$

I take the perturbations as in Eq. (3.12), with complex amplitudes and use Eqs. (3.14)-(3.15) and obtain

$$\Re\mathrm{e}(\xi_r) = \left[-(\det A)^{-1} 2f^2m^2 \frac{\tau^2 v_{\perp}^2}{\pi R_{\mathrm{t}}}\right] \cos(m\phi) \tag{3.16}$$

$$\Re\mathrm{e}(\xi_\phi) = \left[-(\det A)^{-1} 4f\left(f - \frac{1}{2\gamma}\right) m \frac{\tau^2 v_{\perp}^2}{\pi R_{\mathrm{t}}}\right] \sin(m\phi). \tag{3.17}$$

The resultant displacement vectors are shown in Fig. 3.2 for a flux tube at the bottom of the overshoot region, for $m = 5$, where $v_{\perp}$ is taken as 14 m s^{-1} from the non-local mixing length model by Skaley and Stix (1991). The amplitude of the azimuthal displacement is smaller than the radial one by a factor

$$\frac{|\xi_\phi|}{|\xi_r|} = \left|\frac{1}{m}\left(2 - \frac{1}{\gamma f}\right)\right| \simeq 0.68. \tag{3.18}$$

Because the phase difference between the radial and azimuthal displacements is $\pi/2$, the maximum azimuthal displacement occurs at the nodes of the radial displacement. Therefore, the azimuthal perturbation does not lead to a significant change in the positions of the crests and troughs of the flux tube.

3.1.2 Flux tubes outside the equatorial plane

The corresponding equations for a stationary flux ring at an arbitrary latitude λ_0, in the limit of $\beta \gg 1$ (see Ferriz-Mas and Schüssler 1995, Sect. 4.1), deformed by the drag force F_D read:

$$2f^2 \frac{\partial^2 \xi_R}{\partial \phi_0^2} + C_\phi \frac{\partial \xi_\phi}{\partial \phi_0} + C_R \xi_R + C_z \xi_z = -\frac{\tau^2}{\rho_{e0}} F_{\mathrm{D}} \cos\lambda_0, \tag{3.19}$$

$$2f^2 \frac{c_T^2}{v_a^2} \frac{\partial^2 \xi_\phi}{\partial \phi_0^2} + A_R \frac{\partial \xi_R}{\partial \phi_0} + A_z \frac{\partial \xi_z}{\partial \xi_\phi} = 0, \tag{3.20}$$

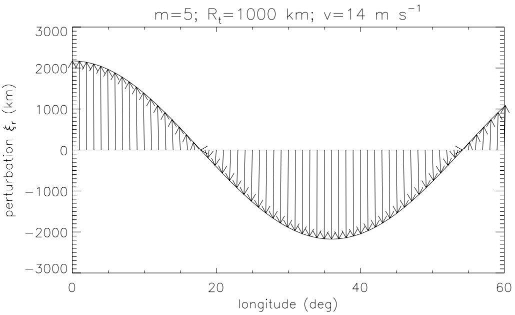

Figure 3.2: Geometry of the axis of a perturbed flux tube in the equatorial plane, in a state of stationary equilibrium between the drag force exerted by the periodic flow and the magnetic curvature and buoyancy forces. $\xi_r = 0$ is the original position of the flux tube. Arrows denote the displacement of the mass elements of the tube due to the flow-induced deformation.

$$2f^2\frac{\partial^2\xi_z}{\partial\phi_0^2} + D_\phi\frac{\partial\xi_\phi}{\partial\phi_0} + D_R\xi_R + D_z\xi_z \quad = \quad -\frac{\tau^2}{\rho_{e0}}F_\mathrm{D}\sin\lambda_0, \tag{3.21}$$

where

$$\begin{aligned} A_R = 4f\left(f - \frac{\cos\lambda_0}{2\gamma}\right), A_z = -\frac{2f}{f}\sin\lambda_0,& \\ C_\phi = -A_R, \quad C_R = \frac{4f}{\gamma}\cos\lambda_0 + \Delta\cos^2\lambda_0,& \\ C_z = \left(\frac{2f}{\gamma} + \Delta\cos\lambda_0\right)\sin\lambda_0,& \qquad (3.22) \\ D_\phi = -A_z, \quad D_R = C_z, \quad D_z = \Delta\sin^2\lambda_0,& \\ \Delta = \beta\delta - \frac{2}{\gamma}\left(\frac{1}{\gamma} - \frac{1}{2}\right).& \end{aligned}$$

(3.23)

Consider a flow along the spherical radial direction, applied to a flux tube located at latitude λ_0. Applying the *ansatz* Eq. (3.12) to Eqs. (3.19)-(3.21), one obtains

$$\underbrace{\begin{pmatrix} C_R - 2f^2m^2 & imC_\phi & C_z \\ imA_R & -2f^2m^2c_T^2/v_A^2 & imA_z \\ D_R & imD_\phi & D_z - 2f^2m^2 \end{pmatrix}}_{A}\begin{pmatrix} \hat{\xi}_R \\ \hat{\xi}_\phi \\ \hat{\xi}_z \end{pmatrix} = \begin{pmatrix} -\frac{\tau^2}{\rho_{e0}}F_\mathrm{D}\cos\lambda_0 \\ 0 \\ -\frac{\tau^2}{\rho_{e0}}F_\mathrm{D}\sin\lambda_0 \end{pmatrix}. \tag{3.24}$$

This equation can be solved in a straightforward way using Cramer's rule. The solution is

$$
\begin{aligned}
\hat{\xi}_R &= \frac{\tau^2 m^2}{\det A}\frac{F_D}{\rho_{e0}}\left\{\cos\lambda_0\left[2f^2\frac{c_\mathrm{T}^2}{v_\mathrm{A}^2}(D_z-2f^2m^2)-A_zD_\phi\right]\right. \\
&\qquad\qquad\left. +\sin\lambda_0\left[A_zC_\phi-2f^2\frac{c_\mathrm{T}^2}{v_\mathrm{A}^2}C_z\right]\right\}, \qquad (3.25)\\
\hat{\xi}_\phi &= im\frac{\tau^2}{\det A}\frac{F_D}{\rho_{e0}}\left\{\cos\lambda_0\left[A_R(D_z-2f^2m^2)-A_zD_R\right]\right. \\
&\qquad\qquad\left. +\sin\lambda_0\left[A_z(C_R-2f^2m^2)-A_RC_z\right]\right\}, \qquad (3.26)\\
\hat{\xi}_z &= \frac{\tau^2 m^2}{\det A}\frac{F_D}{\rho_{e0}}\left\{\cos\lambda_0\left[A_RD_\phi-2f^2\frac{c_\mathrm{T}^2}{v_\mathrm{A}^2}D_R\right]\right. \\
&\qquad\qquad\left. +\sin\lambda\left[2f^2\frac{c_\mathrm{T}^2}{v_\mathrm{A}^2}(C_R-2f^2m^2)-A_RC_\phi\right]\right\}. \qquad (3.27)
\end{aligned}
$$

Substituting the complex amplitudes (3.25)-(3.27) in the respective components of the *ansatz* Eq. (3.12) and using Euler's identity, the components of the displacement read

$$
\begin{aligned}
\xi_R &= \hat{\xi}_R\cos(m\phi_0),\\
\xi_\phi &= -\Im\mathrm{m}(\hat{\xi}_\phi)\sin(m\phi_0),\\
\xi_z &= \hat{\xi}_z\cos(m\phi_0). \qquad (3.28)
\end{aligned}
$$

Again, there is a phase difference of $\pi/2$ between the azimuthal displacement ξ_ϕ and the spherical radial displacement $\xi_r = (\xi_R^2+\xi_z^2)^{1/2}$. As a result, the radial position of the tube crest is not affected significantly by the azimuthal displacements, similar to the case of an equatorial flux tube in Sect. 3.1.1. Fig. 3.3 shows ξ_r as a function of ϕ, using Eqs. (3.28), evaluated at three depths in the overshoot region. The values for the convective velocity are taken from a non-local mixing length model (Skaley and Stix 1991). The azimuthal wave number is chosen such that in each case the crests or the troughs of the perturbed tube would get very close to the boundaries of the overshoot layer, the extent of which is about 10^4 km according to the model. Let us call this azimuthal wave number m_crit and the resulting perturbation the *critical perturbation*. For $m < m_\mathrm{crit}$ (wavelength larger than a critical value), the magnetic curvature force is smaller than in the case of the critical perturbation, so that the tube can exceed the boundaries of the overshoot region.

At the bottom of the overshoot region, relatively low wave numbers ($m_\mathrm{crit}\sim 5$) cause the troughs of the tube to touch the highly stable radiative zone. Because of the steep negative gradient of superadiabaticity (δ) with depth at the interface between the overshoot layer and radiative zone, the troughs of the tube become highly buoyant. Therefore, when the flow ceases, the troughs of the tube may start to rise due to strong magnetic buoyancy.

At the middle of the overshoot layer, where the convective flow speed is 26 m s^{-1}, perturbations with $m_\mathrm{crit} = 8$ are able to drag the tube crests up to the convection zone and the troughs down to the radiative zone boundary.

At the top of the overshoot region, large wave-number perturbations ($m_\mathrm{crit}\sim 15$) are

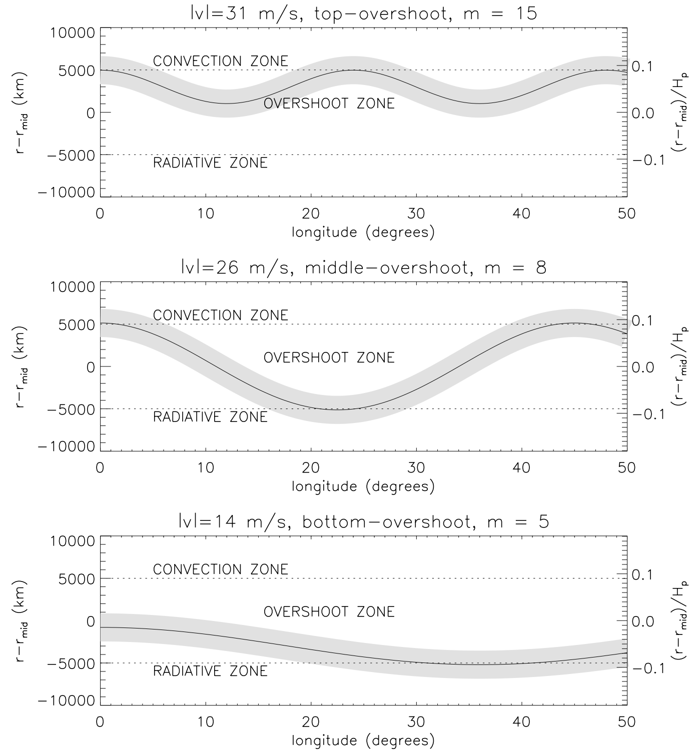

Figure 3.3: Geometry of a flux tube deformed by azimuthally periodic flows, at three initial locations: (from top to bottom of the figure) the top, the middle, and the bottom of the overshoot region. The latitude is 30° and the field strength is $6 \cdot 10^4$ G. The left vertical axes show the distance from the middle of the overshoot region in kilometers on the left axis, and in units of local pressure scale height (at $r = r_{\rm mid}$) on the right axis. The azimuthal wavenumber is chosen such that the troughs or crests of the tube partially enters the convective or the radiative zones. The radius of the tube is 1000 km.

able to carry the tube crests up to the convection zone, owing to the relatively large values for the flow speed (31 m s^{-1}) and superadiabaticity ($\delta \simeq -5.8 \cdot 10^{-7}$). At this location, it is thus more likely for small-scale loops to form, compared to the deeper parts of the layer. The corresponding azimuthal extension of such a loop ($m \sim 15$) is comparable to that of a large bipolar magnetic region on the Sun.

One may expect that rapidly rising flux loops can be formed by localised upflows at the top of the overshoot region. The question is whether such an eruption of a small part of the flux tube can occur near the top of the overshoot region. In order to test this

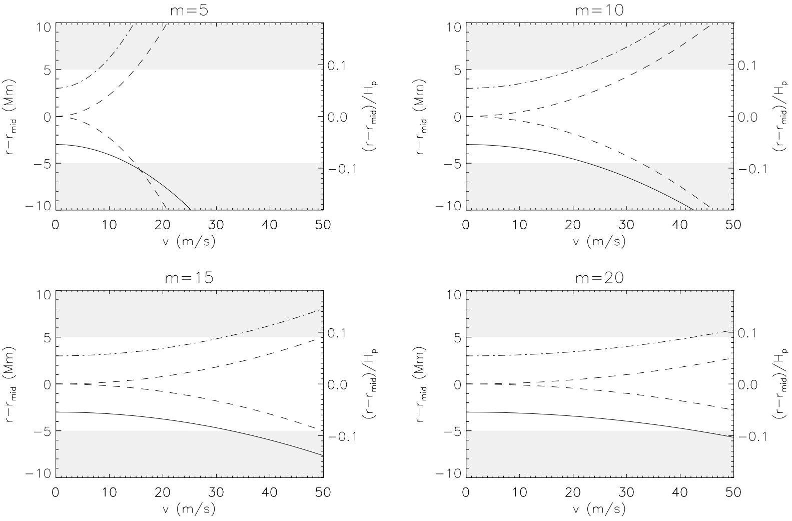

Figure 3.4: Stationary equilibria for flux tubes deformed by a radial external flow that is periodic in azimuth. The magnetic flux density of the tube is $B = 6 \cdot 10^4$ G and the tube radius is $R_t = 1000$ km. The vertical axes denote the distance of the tube crest from the middle depth of the overshoot region on the left hand side and in units of the local pressure scale height at the mid-overshoot region on the right hand side. The horizontal axis shows the amplitude of the flow velocity. The full lines correspond to a tube at the bottom of the overshoot region (only downflows considered), the dashed lines to the one at the middle of the overshoot (up- and downflows), and the dash-dotted line to the top of the overshoot region (only upflows). The shaded regions indicate the radiative zone at the bottom and the convection zone at the top.

possibility, I have carried out nonlinear numerical simulations of a flux tube, which is linearly unstable at the top of the overshoot region. The azimuthal wave number of the perturbation has been chosen to be $m = 15$. The simulation has shown that the wave energy in high modes is gradually transferred into lower-m modes. The tube erupts with $m = 2$ mode, which is consistent with the prediction of the linear stability analysis.

In summary, the critical azimuthal wave number required to carry the tube to the boundaries of the overshoot region, m_{crit}, decreases with increasing depth. The relationship between ξ_r, m, and the radial location of the tube is determined by 1) magnetic curvature force, which increases with m, 2) the convective velocity, which decreases with depth in the overshoot region.

3.1.3 Parameter study

Dependence on the drag velocity and the azimuthal wave number. Fig. 3.4 shows the variation of $r - r_{\mathrm{mid}}$, the radial distance of the crest of the perturbed tube from the middle of the overshoot region, as a function of the velocity amplitude of the radial external flow for various azimuthal wave numbers.

The thickness of the overshoot region in the model corresponds to about 20% of the local pressure scale height at the middle of the layer. For a flux tube deformed by about 5000 km from the middle of the region, the perturbation is about 10% of the local pressure scale height. On the other hand, different parts of the flux tube may be subject to significantly different magnetic buoyancy, because the superadiabaticity changes about three orders of magnitude between the upper and lower boundaries of the overshoot region. A larger perturbation is not expected at those depths for the chosen magnetic fluxes, because the convective velocities in the overshoot region are not expected to be considerably larger than about 50 m s^{-1}. At the top of the overshoot region, a small-scale deformation (a high m) can drive the flux tube into the convection zone proper, whereas for the bottom of the overshoot region, coherent downflows on a rather large scale ($m \sim 5$) are required to push the tube down to the radiative interior. However, the actual depth of penetration into the radiative zone cannot be estimated in this way, because the superadiabaticity changes strongly, and thus the linear approach becomes incorrect. In fact, the superadiabaticity becomes strongly negative so that the stable stratification acts like a solid wall, largely inhibiting any further downward penetration. I have made thin flux tube simulations for a downdraft of Gaussian shape with an azimuthal extension corresponding roughly to the wave number range $10 \leqslant m \leqslant 20$ near the bottom of the overshoot region. The trough of the flux tube bounces back from the radiative zone boundary. However, because of the drag force, which is proportional to the square of the rising tube velocity, it is quickly decelerated already within the overshoot region and its translational kinetic energy is transformed into MHD waves propagating along the tube.

Dependence on the magnetic field strength and the tube radius. Fig. 3.5 shows the variation of the maximum displacement of a flux tube as a function of its field strength. The cross-sectional radius of the flux tube is 10^3 km, and the amplitude of the azimuthally periodic perpendicular flow is 14 m s^{-1} at the bottom, 26 m s^{-1} at the middle, and 31 m s^{-1} at the top of the (overshoot) region. As the azimuthal wave number of the flow is increased, the tension force resists the deformation of the tube more strongly, so that the perturbation decreases. For fields with $B > 10^5$ G and perturbations with $m > 10$, the deformation of the tube by the flow becomes smaller than $10^{-3} H_p$. The corresponding superadiabaticity difference between the depths of the crests and the troughs is smaller than 10^{-7}. Therefore, a perturbation amplitude of this order may be chosen when carrying out nonlinear numerical simulations of toroidal thin flux tubes (e.g., in Chapter 4). In Sect. 3.2, it is shown that for larger perturbations, nonlinear effects can determine the growth rate of Parker instability. For increasing B and m, the radial displacement decreases and eventually becomes less sensitive to the field strength, owing to increasing magnetic tension force. For $m = 20$, a perpendicular flow with a speed of 26 m s^{-1}, applied to a tube with $B = 10^5$ G, located at the middle of the overshoot region, displaces it to an extent of about $5 \cdot 10^{-3} H_p$ (~300 km). Concerning the onset of Parker instability, the results of numerical simulations of toroidal flux tubes (e.g., in Sect. 3.2 and Chapter 4)

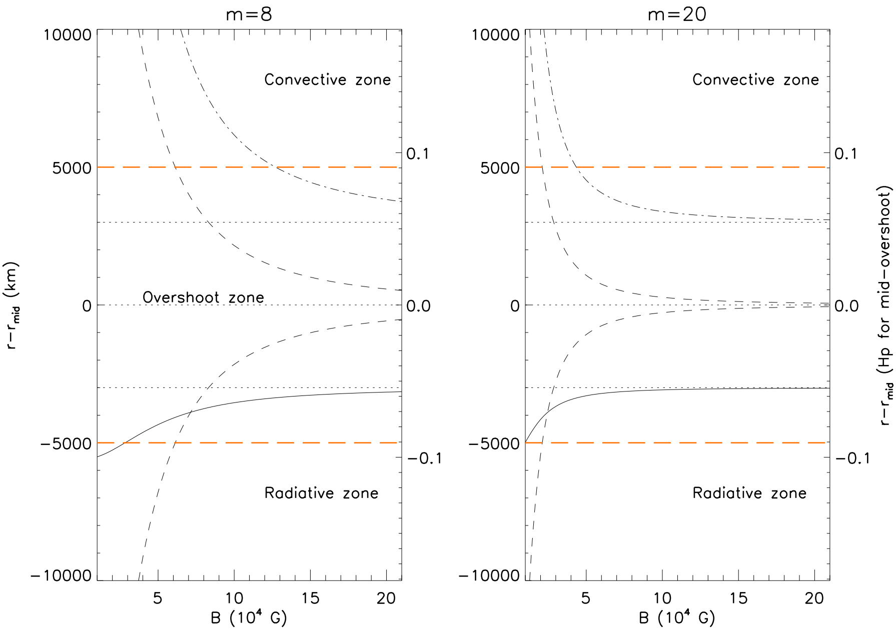

Figure 3.5: Stationary equilibria for flux tubes deformed by a radial external flow that is periodic in azimuth. The radius, the latitude, the initial depth of the flux tubes, and the vertical axis, and the line styles in the plots are the same as in Fig 3.4. The varied parameter is the magnetic field strength of the tube (horizontal axis). The tube is subjected to an azimuthally periodic flow with an amplitude of 10, 26, 31 m s^{-1} for the bottom, middle, and top of the overshoot region, respectively. The red dashed lines indicate the boundaries of the radiation and convection zones.

with perturbation amplitudes $\hat{\xi} \lesssim 10^{-3} H_p$ (55 km) are in overall agreement[2] with the prediction of the linear stability analysis.

Now I set $B = 6 \cdot 10^4$ G and $v_\perp = 26$ m s^{-1} and vary the tube radius, R_t, as shown in Fig. 3.6. Because the drag force is inversely proportional to R_t, the dynamics of thicker tubes is less affected by the external flow. For $m = 20$, tubes thicker than about 2000 km

---

[2] The numerical simulations are made with a superposition of modes between $m = 1$ and $m = 5$. However, the results of simulations do not depend on the choice of the azimuthal mode, say $m = 1$ or $m = 20$. In the latter case, the energy in high-degree modes are transferred to low-degree modes, such that the fastest growing mode is still $m = 1$ or $m = 2$. On the other hand, for $\hat{\xi} \gtrsim 10^{-3} H_p$, nonlinear effects become large enough to lead to instability even in the linearly stable regime. In other words, the amplitude of perturbations chosen for the numerical simulations corresponds to a disturbance that could indeed be caused by perpendicular flows with the estimated range of convective speeds in the framework of the mixing length approximation.

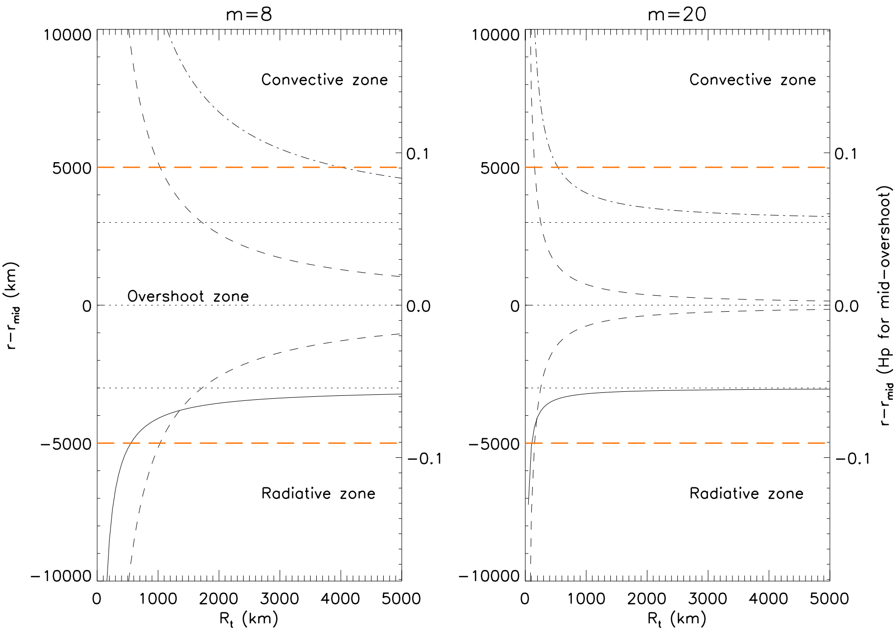

Figure 3.6: Same as Fig. 3.5, for $B = 6 \cdot 10^4$ G and varying tube radius.

in diameter do not touch the boundaries of the overshoot region. At a first glance, this indicates that thicker tubes may be stored for longer times than thinner tubes. However, diameters above 5000 km are not relevant in the present context, because the thin flux tube approximation is not valid for a tube which has a diameter comparable with the thickness of the overshoot layer.

3.2 Nonlinear effects caused by finite perturbations

The purpose of this section is to discuss the effects of perturbations beyond the linear limits and to obtain the velocity of the external flow which allows for the storage of toroidal magnetic flux tubes in the overshoot region for times on the order of 1000 days. The linear stability analysis for thin toroidal magnetic flux tubes as carried out by Ferriz-Mas and Schüssler (1995) gives the growth rate of Parker instability as a function of latitude and time. Figure 3.7 shows stability diagrams for flux tubes located at the bottom and the middle of the overshoot region, for the case of rigid rotation.

When carrying out test simulations for thin toroidal magnetic flux tubes in order to seek an appropriate value for the perturbation amplitude, I realised that for linearly sta-

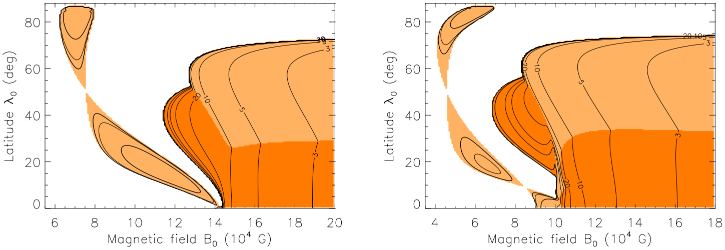

Figure 3.7: Stability diagrams for a flux tube in the bottom (left panel) and the middle (right panel) of the overshoot region. White areas show the linearly stable regime. Contour lines denote the growth time of the undulatory instability, in days. The two thick contours correspond to 100 and 300 days. The fastest growing mode is $m = 1$ within the light-shaded regions, and $m = 2$ within the dark shaded region.

ble configurations (shown as white regions in Fig. 3.7), initial perturbations which have a radial extent larger than about 10^{-3} H_p ($\sim$ 55 km) lead to eruption of the tube in times of days to weeks. The initial perturbation was periodic in azimuth with a superposition of modes from $m = 1$ to $m = 5$. They were applied in radial, azimuthal, and latitudinal directions. It turned out that the growth rate of this nonlinear instability depends on the perturbation amplitude. A possible explanation for the instability is that the initial perturbation and the steep radial gradient of superadiabaticity in the overshoot region cause different parts of the flux ring to experience a significantly different magnetic buoyancy force, outside the range of validity of the linear analysis. This leads to a buoyancy instability with the formation of a rising loop. In the following subsections, I will investigate the dependence of the instability growth time on the perturbation amplitude.

3.2.1 Flux tubes at high latitudes

I have carried out a number of simulations with the following settings: the equilibrium flux ring is located either at the bottom (with $B = 12.6 \cdot 10^4$ G) or at the middle (with $B = 8 \cdot 10^4$ G) of the overshoot region, at a latitude of 58°. For these values the flux tube is close to the Parker instability limit, but is stable against linear perturbations (Fig. 3.7). Fig. 3.8 shows the difference $\Delta\delta$ between the superadiabaticities at the depths of the highest ($R_{\max}$) and the lowest ($R_{\min}$) parts of the perturbed flux tube, as a function of $\Delta R = R_{\max} - R_{\min}$. The simulations were run without considering the drag force. The perturbations were applied either with only $m = 1$, or with a superposition of all modes in the range $1 \leqslant m \leqslant 5$. In both cases, nonlinear Parker instability sets in, because the radial displacement of the tube is sufficiently large for the crests of the tube to reach a location with a significantly larger value of δ, leading to a sufficiently high buoyancy at the crests of the tube. In the first case, the instability is trigerred for $\Delta R \gtrsim 1000$ km, which corresponds to $\log(\Delta\delta) \gtrsim -5.8$. In the second case, it occurs for $\Delta R \gtrsim 600$ km and $\log(\Delta\delta) \gtrsim -6.1$.

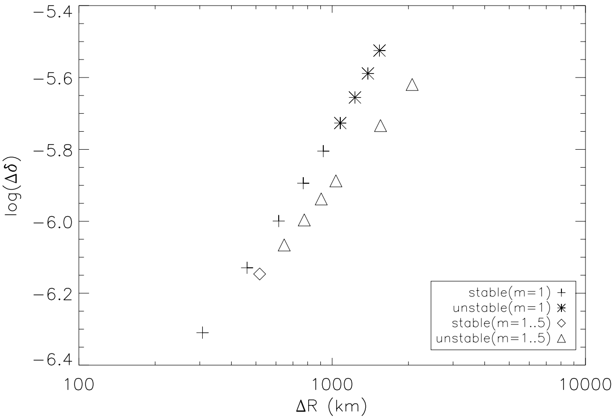

Figure 3.8: Logarithm of the difference $\Delta\delta$ of superadiabaticity between the surroundings of the top and bottom parts of the flux tube, as a function of the difference in the spherical r coordinates of the top and bottom parts of the tube. The simulations are run for $B_0 = 12.6 \cdot 10^4$ G, $\lambda_0 = 58°$, at the bottom of the overshoot region, without taking the drag force into account. $m = 1$ means that the perturbation was applied with the azimuthal wave number 1, and $m = 1..5$ means that perturbations with azimuthal wave numbers from 1 to 5 were superimposed with equal amplitudes.

When the drag force is taken into account in the numerical simulations, one finds instability for all latitudes and field strengths, provided that the field strength is above a critical value of about $4 \cdot 10^4$ G, which is weakly dependent on latitude (Holzwarth 2002). The instability is related to the hydrodynamic drag force (in other words, friction) and the presence of a field-aligned flow. The mechanical equilibrium of a toroidal thin flux tube requires a relative flow between the internal and external medium (see Eq. 3.1). If the velocity of this relative flow is larger than a critical value determined by the propagation velocity of the slowest retrograde eigenmode, it leads to transversal (MHD) waves of growing amplitude, in the presence of drag force. Figure 3.9 shows the results of simulations carried out for the middle overshoot region, $\lambda = 58°$, and $B = 8 \cdot 10^4$ G, taking into account the drag force and all the 5 azimuthal modes. The growth times have been estimated by fitting exponential functions to the variation of $r_{\rm top}$ (radial coordinate of the highest point of the flux tube) with time. For a given perturbation ΔR, the difference $\Delta\delta$ between the crest and the trough of a mid-overshoot tube is less than the corresponding value for the bottom-overshoot region. The reason is the steepening radial gradient of $\Delta\delta$ when approaching the radiative core. The growth time of the instability decreases as the perturbation amplitude is increased, as shown in Fig. 3.10, following roughly a power law. Two effects may be responsible for this dependence: a) $\Delta\delta$ increases with ΔR, causing a more rapid rise of the tube crest; b) it may be related to the nature of the friction-

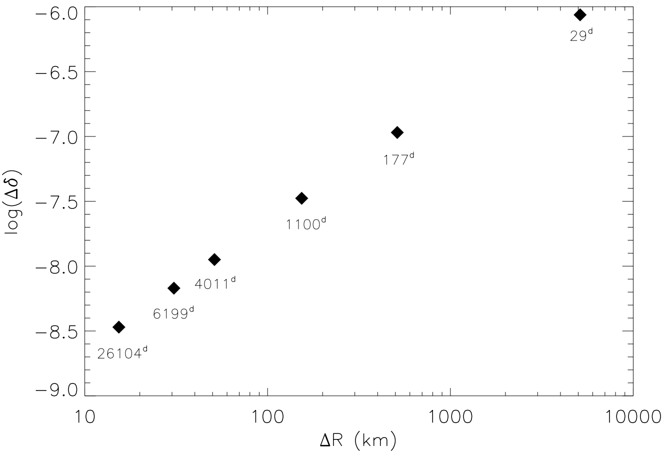

Figure 3.9: Same as Fig. 3.8, for the middle of the overshoot region, $B_0 = 8 \cdot 10^4$ G, $m = 1..5$ and with the drag force. Numbers indicate the growth time of the instability, in days.

induced flow instability, because the drag force is taken into account in the simulations (see Sect. 3.3).

3.2.2 Flux tubes at low latitudes

Next, I present simulations of toroidal flux tubes located at the middle of the overshoot region, at a latitude of 30°. For an initial flux density of $7 \cdot 10^4$ G, the tubes are linearly stable, since the drag force does not appear in the linearised equations of motion. Fig. 3.11 shows the superadiabaticity difference $\Delta\delta$ as a function of the displacement amplitude ΔR, at the beginning of the simulation, similar to Fig. 3.9. The drag force is taken into account, and perturbations are applied with $1 \leqslant m \leqslant 5$, having equal contributions. In all the simulations, flux tubes are unstable, i.e., they form buoyantly rising loops. The growth time of the instability decreases with increasing ΔR, as in the previous result shown in Fig. 3.9. I have carried out simulations without the drag force as well, and found no instability, in contrary to the case in the previous section (Fig. 3.8). In this case, the dependence of growth time on ΔR ($\sim |\xi_r|$) is therefore related to the nature of the friction-induced instability, rather than to $\Delta\delta$. Figure 3.12 shows the variation of the growth time as a function of ΔR. The relation follows a power law, as in the previous case.

I also show in Figs. 3.11 & 3.12 the perpendicular velocity amplitude of the external flow, as determined by Eqs. (3.25)-(3.27), for $m = 5$ and $|\xi_r|$ as given by the range of ΔR in the plot. For $|v_\perp| \lesssim 10$ m s^{-1}, a toroidal flux tube with $\lambda = 30°$, $B = 7 \cdot 10^4$ G, and

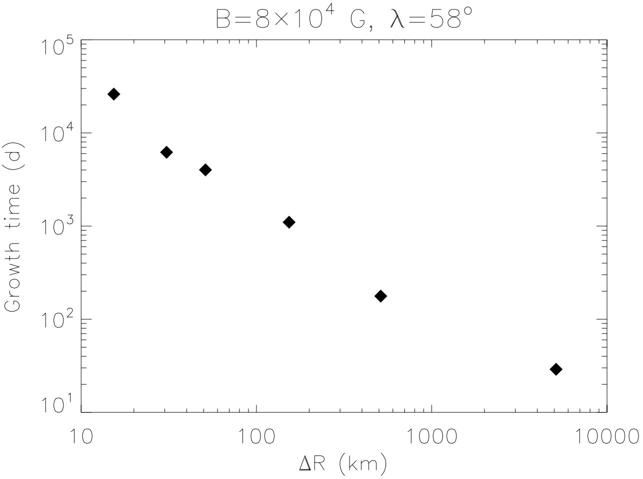

Figure 3.10: Growth time as a function of the displacement amplitude, for $B = 8 \cdot 10^4$ G, $\lambda = 58°$, at the middle of the overshoot region.

$R_\mathrm{t} = 1000$ km, can be stably stored in the overshoot region for a few years. However, this velocity estimate is based on the assumption of a rather well-ordered, azimuthally periodic flow field, which may not actually be the case in the solar convective overshoot region.

The simulations presented in the last two sections indicate that the instability with perturbation-dependent growth rate in the linearly Parker-stable regime is induced mainly by the hydrodynamic drag. However, at high latitudes nonlinear effects still play a role in the dynamics of flux tubes subject to finite perturbations. In the next section, I will further investigate the nature of the friction-induced instability in the nonlinear regime, in comparison with results of linear stability analysis.

3.3 Nonlinearity of the friction-induced instability

The linear stability analysis of thin horizontal flux tubes including a Stokes-type drag force per unit volume,

$$F_\mathrm{St} = \rho_e C_\mathrm{St} \mathbf{v}_\perp, \tag{3.29}$$

where the constant C_St is the Stokes drag coefficient, was carried out by Holzwarth (2002) and Holzwarth et al. (2007). This substitution was made in order to consider the drag force in the linearised equations of motion. These studies have shown that the threshold field strength leading to friction-induced instability is independent of the Stokes drag

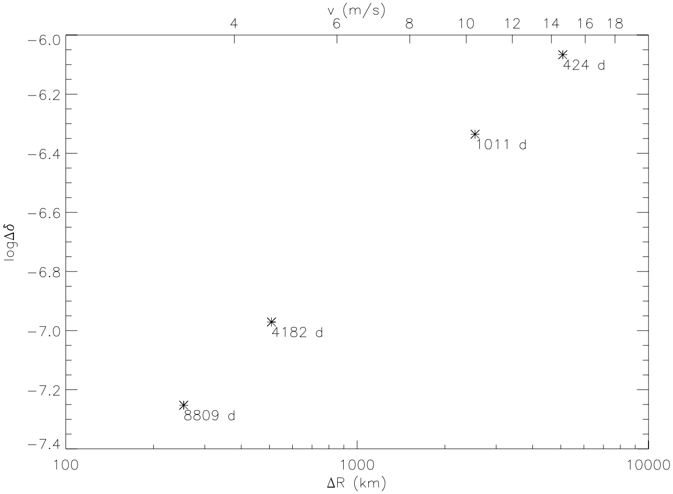

Figure 3.11: Same as in Fig. 3.8, for a flux tube initially located at the middle overshoot zone and $\lambda = 30°$, with a field strength of $7 \cdot 10^4$ G. The upper horizontal axis shows the velocity amplitude of the perpendicular flow, which would lead to the displacement ΔR, with $m = 5$ and $|v_\perp|_{\max} = 26\ \mathrm{m\ s^{-1}}$.

coefficient. Considering the actual drag force per unit volume (Eq. 3.2), the Stokes drag coefficient is of the order

$$C_{\mathrm{St}} \sim \frac{C_{\mathrm{D}} v_\perp}{\pi R_{\mathrm{t}}}, \tag{3.30}$$

where the drag coefficient, C_{D}, is of the order of unity, assuming cylindrical geometry and high Reynolds number. Holzwarth (2002) has estimated the value of C_{St} by carrying out numerical simulations of thin flux tubes including the full drag force (Eq. 3.2) and taking the tube radius to be $R_{\mathrm{t}} = 1000$ km. He has obtained an average value for C_{St} at the initial stages of the simulations. He has also calculated the growth rates of the instability of flux tubes in the (λ, B) plane, based on the linear stability analysis including the Stokes drag force (Eq. 3.29). Figure 3.13 shows the growth rates of the friction-induced instability as a function of the magnetic field strength, for 30° latitude at the middle of the overshoot region, for various values of C_{St} (data courtesy V. Holzwarth). The two plateaus where most of the curves merge correspond to Parker-unstable regions in the linear regime (shaded regions in Fig. 3.7). Thus Fig. 3.13 can be seen as a horizontal cut through Fig. 3.7 at $\lambda_0 = 30°$ (Fig. 3.7 corresponds to $C_{\mathrm{St}} = 0$).

Fig. 3.14 shows the same latitudinal cut as in Fig. 3.13, with a few curves corresponding to the range $5 \cdot 10^{-9} \leqslant C_{\mathrm{St}} \leqslant 1 \cdot 10^{-7}$, along with the growth rates from simulations presented in Sect. 3.2.2. Each set of simulations is made with different values of the per-

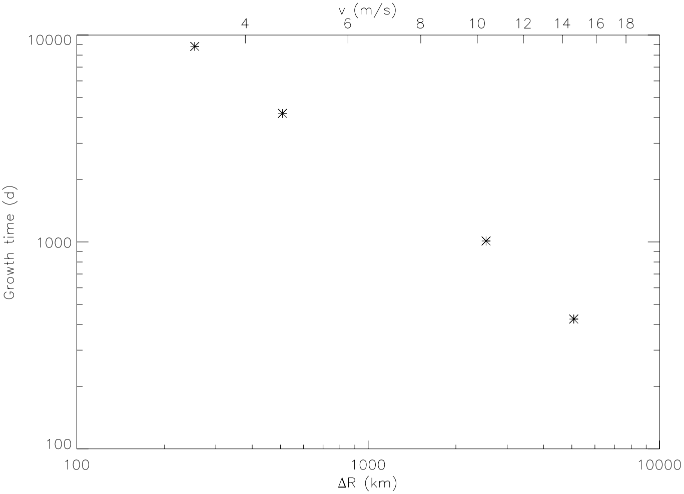

Figure 3.12: Growth time as a function of the displacement amplitude, $B = 7 \cdot 10^4$ G, $\lambda = 30°$, at the middle of the overshoot region.

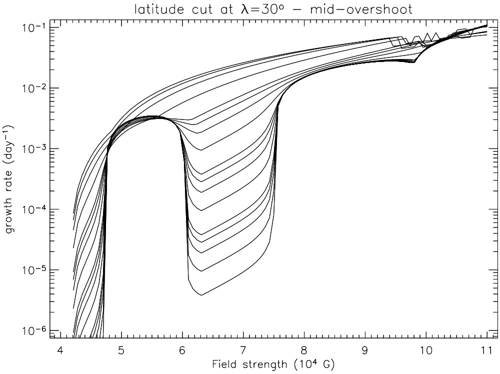

Figure 3.13: Results of the linear stability analysis (Holzwarth 2002) for a flux tube at 30° latitude, and for the Stokes drag coefficient in the range $7.5 \cdot 10^{-9} \leqslant C_{\mathrm{St}} \leqslant 10^{-5}$, C_{St} increasing towards the top of the plot for the range $6 \cdot 10^4 \lesssim B \lesssim 8 \cdot 10^4$ G.

turbation amplitude. The lines of constant C_{St} are chosen among those in Fig. 3.13, which give the best fit to the growth rates found in the simulations. The plateaus for which all the analytical solutions merge correspond to the Parker-unstable regime. The results of

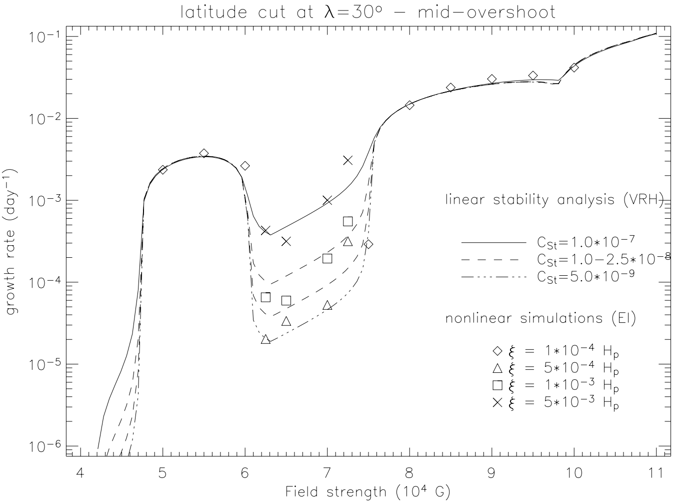

Figure 3.14: Comparison of the analytical solutions for the growth rate of the friction-induced instability (lines) with the numerical simulations (symbols) for flux tubes at the middle of the overshoot region and 30° latitude. The initial perturbation amplitude (ξ), and the Stokes drag coefficient ($C_{\rm St}$) are indicated in the legend.

the linear stability analysis match well with the numerical simulations. If one extends Eq. (3.30) for $C_{\rm St}$, it turns out that

$$C_{\rm St} \sim \frac{C_{\rm D} v_\perp}{\pi R_{\rm t}} \quad \propto \quad |\xi_r| \;\; \Re{\rm e}(\omega), \tag{3.31}$$

where $|\xi_r|$ is the amplitude of the radial perturbation and ω is the eigenfrequency of the fastest growing unstable wave mode for the case in which the Stokes drag force (Eq. 3.29) is taken into account in the unperturbed momentum equation. Therefore, for a given value of $\Re{\rm e}(\omega)$ (which is fixed for given λ and B), $C_{\rm St}$ increases with increasing perturbation amplitude, which is consistent with Fig. 3.14. Recalling the relation between the velocity amplitude of the external flow, $v_\perp$, and the perturbation amplitude, $|\xi_r|$, ($\sim \Delta R$; see Sect. 3.2.2), and taking $\xi_r \sim 5 \cdot 10^{-3} H_p$ from the data set with the largest growth rate (crosses in Fig. 3.14), one finds that the displacement can be caused by a flow with $v_\perp \sim 1$ m s^{-1} and $m = 5$ in the middle of the overshoot region (using Eqs. 3.25-3.27). Using Eq. (3.30), $v_\perp = 1$ m s^{-1} corresponds to $C_{\rm St} \simeq 3 \cdot 10^{-7}$, which is of the same order with the value chosen for the full curve in Fig. 3.14. As a result, the two approaches give the similar results: an external flow with a perpendicular component of 1-10 m s^{-1} leads to instability with a growth time on the order of 1000 days for a flux tube with the parameters chosen here. This range of velocities are consistent with the estimates of van

Ballegooijen (1982) for the convective velocities in the overshoot region, supporting the possibility of the storage of magnetic flux tubes containing fluxes on the order of 10^{21} Mx.

3.4 Summary

In this chapter, the problem of magnetic flux storage in the solar convection zone has been considered, with regards to the effects of external flows on toroidal magnetic flux tubes. Analytical solutions for the stationary equilibrium of a flux tube are obtained, and numerical simulations are made in order to test the stability of a given flux tube configuration. This approach has allowed me to infer the deformation of flux tubes by perpendicular flows of a given velocity amplitude. Substituting the deformation amplitude, I have done numerical simulations which show that in the nonlinear regime, linearly stable flux tube can become unstable. Furthermore, the growth rate of the instability is found to be proportional to the deformation amplitude. Simulations taking the hydrodynamic drag force into account has shown that the friction-induced instability (Holzwarth 2002, Holzwarth et al. 2007) is the main cause for the perturbation-dependent nonlinear buoyancy instability. The main results are summarised below.

- An azimuthally periodic external flow perpendicular to the flux tube induces perturbations in the (spherical) radial and azimuthal directions. The azimuthal perturbation has a smaller amplitude than the radial one, and their azimuthal phase difference is $\pi/2$. Therefore, azimuthal perturbations induced by perpendicular flows do not contribute significantly to the final shape of the deformation in stationary equilibrium.

- Perpendicular flows with an azimuthal wave number of $m = 15$ and with an amplitude 31 m s^{-1} can deform flux tubes of 2000 km thickness and $B = 6 \cdot 10^4$ G from the middle of the overshoot layer up to the convection zone proper. However, numerical simulations made for linearly stable flux tubes do not lead to instability within a few thousand days. In the linearly unstable regime, the instability develops, but the initial deformation pattern with $m = 15$ is changed to $m = 1$ or $m = 2$, in accordance with the results of linear stability analysis. This means that magnetic flux can be stored within the upper overshoot region within flux tubes with $R_{\mathrm{t}} \sim 1000$ km and field strengths of a few times 10^4 G for times on the order of a few years in the course of the dynamo intensification. This is supported by a comparison with the numerical experiments in Sect. 3.2.2: if the amplitude of the perpendicular velocity of the external flow is on the order of 10 m s^{-1}, when considered with the simulation results presented in Fig. 3.12, I estimate that flux tubes with a field strength of a few tesla can be stored for times of the order of a few years in the middle of the convective overshoot region. This velocity is about a factor of two less than the value given by the non-local mixing length model of Skaley and Stix (1991).

- Although the actual flow pattern in the overshoot region is unknown, assumption of an idealised flow has allowed me to obtain scaling relations between the perpendicular velocity, perturbation (deformation) amplitude, magnetic field strength, and the tube radius. I have obtained the ranges of flow velocity, field strength, and tube radius for which the tubes stay in the linear regime after a deformation in the overshoot region, corresponding to an azimuthal wave number. The problem of whether they can be stored for a sufficiently long time is considered by the nonlinear simulations.

- The estimate for the Stokes drag parameter, $C_{\mathrm{St}} \simeq 3 \cdot 10^{-7}$, indicates that the friction-induced flux tube instability develops in times of a few years, so that it is possible for magnetic flux tubes to be stored for sufficiently long times, which is necessary for the operation of the deep-seated solar dynamo.

3.5 Conclusion

In this systematic study concerning the effects of external flows on thin toroidal magnetic flux tubes at the base of the solar convection zone, I have found quantitative relations between the spatial scales of the flow and its subsequent effects. Within the existing estimates of flow velocities in the overshoot region, flux tubes can be stored for sufficiently long times for the operation of the dynamo. In particular, relatively fast upflows and downflows with a relatively small horizontal extent do not disturb the storage of flux tubes, owing to the magnetic curvature force, which increases with decreasing horizontal extent of the flow. On the other extreme, in order for relatively slow perpendicular flows to disrupt the tubes substantially, flows have to be coherently aligned over a large horizontal (azimuthal) extent, which is not very likely in the overshoot region.

Finally, I have shown that field-aligned flows lead to nonlinear and friction-induced instabilities with a dependence on the perturbation amplitude. If the flows have a typical speed of 10 m s^{-1}, toroidal flux tubes with a field strength of $7 \cdot 10^4$ G can be stored in the middle of the overshoot region for times on the order of a few years.

4 A coupled model of magnetic flux generation and transport

The increasing observational knowledge about stellar magnetic activity makes it possible to use the observed activity patterns to constrain stellar dynamo models (see e.g., Strassmeier 2005, Schüssler 2005, Holzwarth et al. 2006). On the one hand, most solar and stellar dynamo models in the literature assume that the latitudinal distribution of toroidal magnetic fields created in stellar interiors represent also the surface emergence patterns. However, the agreement between the latitudinal distribution of dynamo-generated field and the emergence pattern is not self-evident, because a) the stability properties of flux tubes in the bottom of the convection zone are not uniform and b) rising flux tubes are deflected towards the poles, owing to the Coriolis force. On the other hand, numerical simulations of the rise of flux tubes in the convection zone (Caligari et al. 1995) have successfully reproduced many observed properties of sunspot groups, among which the tilt angle is of particular importance for surface flux transport models (Baumann et al. 2004) and Babcock-Leighton-type dynamos (Dikpati and Charbonneau 1999). Therefore, it is now possible to consider in a consistent way the interrelations between the dynamo mechanism operating in stellar interiors, the transport of toroidal magnetic flux through the convection zone, and the emerging flux which evolves under the effects of surface flows. The approach taken here combines models for three processes: 1) the dynamo operating in the overshoot layer at the bottom of the convection zone, 2) the stability and rise of magnetic flux tubes through the convection zone, 3) the transport of magnetic flux on the surface.

4.1 Dynamo model

We consider the generation of magnetic flux in the overshoot layer at the bottom of the convection zone (at radius $r_0 \simeq 0.73R_\odot$). As a first example, we incorporate a kinematic $\alpha\Omega$ dynamo operating in a thin layer at this radius (Schmitt and Schüssler 1989). The model is based on the assumption that the radial diffusion of magnetic flux out of the layer is to some extent compensated by downward flux pumping by convective flows.

4.1.1 Differential rotation and the α-effect

We prescribe the mean velocity field in the thin layer as $\mathbf{u} = (0, 0, \Omega(r, \theta))$, where Ω stands for stellar angular rotation rate. The radial shear at the dynamo layer ($r = r_0$),

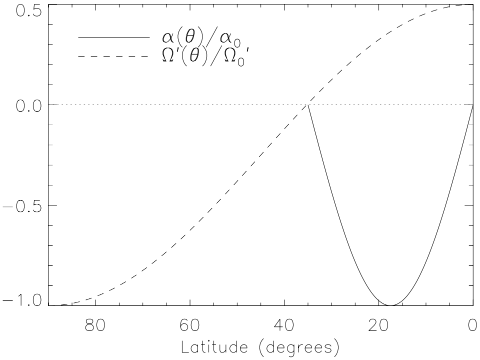

Figure 4.1: Normalised latitudinal profiles of α and the radial shear Ω'. α_0 is assumed to be negative, because $\alpha \cdot \Omega' < 0$ is required for equatorward propagating dynamo waves.

$\Omega' = d\Omega/dr$, is taken in the form

$$\Omega'(\theta) = -\Omega_0' P_2^0(\cos\theta) = -\frac{\Omega_0'}{2}(3\cos^2\theta + 1), \tag{4.1}$$

which is a suitable approximation to the observed shear profile in the solar tachocline, with $\Omega_0' \simeq 10^{-17}$ cm^{-1} s^{-1} at the equator, $\theta = \pi/2$, (Schou et al. 1998).

The latitudinal dependence of the α-effect is taken as

$$\alpha(\theta) = \begin{cases} \alpha_0 \sin\left[\pi\,(\theta - \theta_0)\,/\,(\pi/2 - \theta_0)\right] & : \quad \text{for } \theta \geqslant \theta_0 \\ 0 & : \quad \text{for } \theta < \theta_0, \end{cases} \tag{4.2}$$

where α_0 is the amplitude, and θ_0 is set to 55°, which corresponds to the zero crossing of the function $\Omega'(\theta)$. The functions $\alpha(\theta)$ and $\Omega'(\theta)$, normalised to their amplitudes, are shown in Fig. 4.1. The choice of Eq. (4.2) is motivated by an α-effect due to flux tube instabilities (Ferriz-Mas et al. 1994) or unstable magnetostrophic waves (Schmitt 2003). For dynamo waves propagating equatorward, one must have $\alpha\Omega' < 0$. In order to fulfill this criterion, α_0 has been chosen to be negative, because the sign of radial shear in the solar tachocline is known to be positive at this latitude range.

4.1.2 Dynamo equations

We decompose the axisymmetric mean magnetic field $\mathbf{B} = (B_r, B_\theta, B_\phi)$ into a toroidal component, $(0, 0, B(\theta))$, and a poloidal component described by the vector potential $\mathbf{A} = (0, 0, A(\theta))$:

$$\mathbf{B} = B(r,\theta)\mathbf{e}_\phi + \nabla \times \left(A(r,\theta)\mathbf{e}_\phi\right), \tag{4.3}$$

where $\mathbf{e}_\phi$ is the unit vector in the azimuthal direction. Following Hoyng et al. (1994), the radial dependence of A and B is assumed to have the form of a spherical wave with a certain wavenumber k:

$$\begin{aligned} A(r,\theta,t) &= A(\theta,t)\frac{r_0}{r}\exp(ikr) \\ B(r,\theta,t) &= B(\theta,t)\frac{r_0}{r}\exp(ikr) \end{aligned} \tag{4.4}$$

With this r-dependence, we include to some extent the effect of radial turbulent diffusion. Having defined the radial dependence, the axisymmetric mean (azimuthally averaged) magnetic field is considered as a function of the colatitude, θ.

The dynamo equations are obtained by writing the magnetic induction equation in spherical coordinates in the form of two equations for the poloidal and the toroidal components of the magnetic field:

$$\frac{\partial B}{\partial t} = \Omega'(\theta)\frac{\partial}{\partial\theta}(A\sin\theta) + \frac{\eta}{r_0^2}\left[\frac{1}{\sin\theta}\frac{\partial}{\partial\theta}\left(\sin\theta\frac{\partial B}{\partial\theta}\right) - \frac{B}{\sin^2\theta} - (kr_0)^2 B\right], \tag{4.5}$$

$$\frac{\partial A}{\partial t} = \alpha(\theta)B + \frac{\eta}{r_0^2}\left[\frac{1}{\sin\theta}\frac{\partial}{\partial\theta}\left(\sin\theta\frac{\partial A}{\partial\theta}\right) - \frac{A}{\sin^2\theta} - (kr_0)^2 A\right], \tag{4.6}$$

where η is the turbulent magnetic diffusivity, and r_0 is the distance of the dynamo layer from the centre of the star (middle part of the overshoot region at the bottom of the convection zone; $r_0 = 5.07\cdot 10^{10}$ cm).

We rewrite the dynamo equations in nondimensional form by taking r_0 as unit of length, the diffusion time, r_0^2/η, as unit of time, B_0 as unit field strength, α_0 as the maximum absolute value of the α-effect, and r_0B_0 as unit of the vector potential, A_0. Using the same symbols as before for the nondimensional quantities, Eqs. (4.5) and (4.6) transform into

$$\frac{\partial B}{\partial t} = R_\Omega\frac{\partial}{\partial\theta}(A\sin\theta) + \frac{1}{\sin\theta}\frac{\partial}{\partial\theta}\left(\sin\theta\frac{\partial B}{\partial\theta}\right) - \left(\frac{1}{\sin^2\theta} + (kr_0)^2\right)B \tag{4.7}$$

$$\frac{\partial A}{\partial t} = R_\alpha B + \frac{1}{\sin\theta}\frac{\partial}{\partial\theta}\left(\sin\theta\frac{\partial A}{\partial\theta}\right) - \left(\frac{1}{\sin^2\theta} + (kr_0)^2\right)A. \tag{4.8}$$

We take $kr_0 = 3$, so that a quarter of the wavelength of the radial dependence of the magnetic field corresponds roughly to the thickness of the convection zone.

The system is now described by two dimensionless numbers, namely 1) the Reynolds number for the α-effect,

$$R_\alpha = \frac{\alpha_0 r_0}{\eta}, \tag{4.9}$$

which represents the efficacy of induction by the alpha effect, 2) the Reynolds number for the radial shear (Ω-effect),

$$R_\Omega = \frac{\Omega_0' r_0^3}{\eta}, \tag{4.10}$$

which represents the efficacy of induction by the differential rotation.

The parity of the magnetic field is assumed to be dipolar (antisymmetric with respect to equator). The boundary conditions at the pole and at the equator are then given by

$$B = A = 0 \;\text{ for }\; \theta = 0 \tag{4.11}$$

$$B = 0, \quad \frac{\partial A \sin\theta}{\partial\theta} = 0 \;\text{ for }\; \theta = \pi/2. \tag{4.12}$$

We set the turbulent diffusivity to $\eta \simeq 5.6 \cdot 10^{11}\ \mathrm{cm^2\ s^{-1}}$, and the maximum strength of the α-effect to $\alpha_0 \simeq -22\ \mathrm{cm\ s^{-1}}$. With this choice of parameters, the fundamental dynamo mode at the limit of marginal stability[1] is obtained with a cycle period of about 22 years.

Eqs. (4.7)-(4.8) with the boundary conditions Eqs. (4.11)-(4.12), are numerically solved using a finite-difference algorithm.

4.2 Emergence of magnetic flux

We assume that in the dynamo layer, the toroidal magnetic field undergoes magnetic Rayleigh-Taylor instability, which leads to the formation of magnetic flux tubes (see Sect. 1.4 and Fan 2001). The flux tubes are subject to the undulatory (Parker) instability once their field strength exceeds a critical value, B_{cr}, which is a function of latitude (at a given depth in the convective overshoot layer). We determine the linear properties and the subsequent nonlinear evolution of the instability by using the thin flux tube approximation (see Sect. 1.3), following Ferriz-Mas and Schüssler (1995) and Caligari et al. (1995).

The equation of motion for the material inside a toroidal flux tube, in a reference frame rotating with angular velocity $\mathbf{\Omega}$, can be written as

$$\rho_i \frac{D\mathbf{v}_i}{Dt} = -\nabla\Big(p_i + \frac{B^2}{8\pi}\Big) + \frac{(\mathbf{B}\cdot\nabla)\mathbf{B}}{4\pi} + \rho_i[\mathbf{g} - \mathbf{\Omega}\times(\mathbf{\Omega}\times\mathbf{r})] + 2\rho_i\mathbf{v}_i\times\mathbf{\Omega} + \mathbf{F}_{\mathrm{D}}, \tag{4.13}$$

where $D/Dt \equiv \partial/\partial t + \mathbf{v}\cdot\nabla$ is the Lagrangian derivative, the subscript i denotes quantities inside the flux tube, and the terms on the right hand side of the equation are, respectively, the total pressure force (gas and magnetic), magnetic tension force, effective gravity (including the centrifugal force), Coriolis force, and hydrodynamic drag force. For the drag force we use the expression for a flow past a straight spherical cylinder:

$$\mathbf{F}_{\mathrm{D}} = -C_{\mathrm{D}} \frac{\rho_e v_\perp \mathbf{v}_\perp}{\pi R_{\mathrm{t}}}, \tag{4.14}$$

where $\mathbf{v}_\perp = v_\perp \hat{\mathbf{v}}_\perp$ is the perpendicular component of relative velocity of the tube with respect to the external medium, $\hat{\mathbf{v}}_\perp$ is the unit vector along $\mathbf{v}_\perp$, C_D is the hydrodynamic drag coefficient which we take as unity (Batchelor 1967), ρ_e is the density of the external medium, and R_{t} is the cross-sectional radius of the tube.

We combine the equation of continuity and the equation of magnetic induction into

---

[1] For the dynamo number $P = R_\alpha R_\Omega$ larger than a critical value, the magnetic field is amplified exponentially, and below that value it decays. The marginal stability is obtained for that critical value of P.

Walén's equation,

$$\frac{D}{Dt}\left(\frac{\mathbf{B}}{\rho_i}\right) = \left(\frac{\mathbf{B}}{\rho_i}\cdot\nabla\right)\mathbf{v}_i. \tag{4.15}$$

For the energy equation, we assume that the mass elements of the flux tube evolve isentropically ($DS/Dt = 0$). This is justified because the time scale for heat exchange by radiation in the deep convection zone is much longer than the time scale of flux tube evolution (Moreno-Insertis 1986). The system of equations is closed by the ideal gas law and the condition of magnetic flux conservation.

The magnetohydrodynamic equations given above are treated using the thin flux tube approximation (Spruit 1981), in the form given by Ferriz-Mas and Schüssler (1993). The flux tube is described as a space curve $\mathbf{r}(s,t)$, at time t, where s, the arc length along the tube, is the Lagrangian coordinate. We consider the orthonormal Frénet basis to define each element of the curve $\mathbf{r}(s,t)$. The unit vectors are $\mathbf{e_t}$ as the one tangent to the tube, $\mathbf{e_n}$ as the one normal to the tube, and $\mathbf{e_b}$ binormal to the tube:

$$\mathbf{e_t} = \frac{\partial\mathbf{r}}{\partial s}; \quad \mathbf{e_n} = \frac{1}{\kappa}\frac{\partial\mathbf{e_t}}{\partial s}; \quad \mathbf{e_b} = \mathbf{e_t}\times\mathbf{e_n}, \tag{4.16}$$

where $\kappa = |\partial\mathbf{e_t}(t)/\partial s|$ is the local curvature. In this approximation, the magnetohydrodynamic equations describing thin flux tubes are as follows.

Equation of motion:

$$\begin{aligned}
\rho_i\frac{D\mathbf{v}}{Dt}\cdot\mathbf{e_t} &= \frac{\partial}{\partial s}\left(\frac{B^2}{8\pi}\right) + (\Delta\rho\mathbf{g}_{\text{eff}} + \mathbf{F}_{\text{rot}})\cdot\mathbf{e_t}, && (4.17)\\
\rho_i\frac{D\mathbf{v}}{Dt}\cdot\mathbf{e_n} &= \frac{B^2}{4\pi}\kappa + (\Delta\rho\mathbf{g}_{\text{eff}} + \mathbf{F}_{\text{rot}} + \mathbf{F}_{\text{D}})\cdot\mathbf{e_n}, && (4.18)\\
\rho_i\frac{D\mathbf{v}}{Dt}\cdot\mathbf{e_b} &= (\Delta\rho\mathbf{g}_{\text{eff}} + \mathbf{F}_{\text{rot}} + \mathbf{F}_{\text{D}})\cdot\mathbf{e_b}, && (4.19)
\end{aligned}$$

Walén's equation (continuity and induction):

$$\frac{D}{Dt}\left(\frac{\rho_i}{B}\right) + \frac{\rho_i}{B}\left[\frac{\partial(\mathbf{v}_i\cdot\mathbf{e_t})}{\partial s} - \kappa(\mathbf{v}_i\cdot\mathbf{e_n})\right] = 0, \tag{4.20}$$

Condition of lateral pressure balance:

$$p_e = p_i + \frac{B^2}{8\pi}, \tag{4.21}$$

Energy equation:

$$\frac{Dp_i}{Dt} = \frac{\gamma p_i}{\rho_i}\frac{D\rho_i}{Dt}, \tag{4.22}$$

where

$$\begin{aligned}\Delta\rho &= \rho_i - \rho_e, && (4.23)\\ \mathbf{g}_{\rm eff} &= \mathbf{g} + \Omega^2 R\,\mathbf{e_R}, && (4.24)\end{aligned}$$

$$\mathbf{F}_{\rm rot} = 2\rho_i(\mathbf{v}\times\mathbf{\Omega}), +\rho_i(\Omega^2 - \Omega_e^2)R\,\mathbf{e_R}, \quad (4.25)$$

and $\mathbf{e_R}$ is the unit vector perpendicular to the axis of stellar rotation.

Eqs. (4.17)-(4.22) are used in the linear stability analysis and in the numerical simulations.

4.2.1 The removal of magnetic flux from the dynamo layer

Magnetic flux is lost from the dynamo layer by means of erupting flux tubes. In order to determine the number, field strengths, and latitudes of erupting flux tubes, we assign an eruption probability, p, at a given latitude and time.

The critical field strength for flux eruption is on the order of 10^5 G for the middle of the convective overshoot layer. The corresponding magnetic energy density is about 100 times larger than the kinetic energy density of convective motions. We assume that the shear-generated mean toroidal field, B, fragments into flux tubes of strength $B_{\rm FT}$, such that

$$B = fB_{\rm FT}, \quad (4.26)$$

where f is the magnetic fill fraction of flux tubes contributing to the mean field. We assume $B_{\rm FT} = 10^5$ G and $f = 0.1$, so that $B \simeq 10^4$ G, which is of the order of the equipartition field strength $B_{\rm eq} = (4\pi\rho)^{1/2}v_c$, where v_c is the convective velocity as determined by using a mixing length model.

Latitudes and number of erupting flux tubes

We assume the emergence rate of flux tubes to be proportional to the mean toroidal field given by the dynamo model,

$$B_{ij} = B(\lambda_i, t_j), \quad i = 1, ..., N \quad (4.27)$$

for given latitude, λ_i, and time, t_j. The eruption probability, p_{ij}, of a flux tube at λ_i and t_j is given by

$$p_{ij} = \frac{B_{ij}}{\sum_i B_{ij}}, \quad (4.28)$$

assuming that exactly one flux tube emerges at time t_j. At every time t_j, n_j flux tubes emerge. In order to determine the initial latitudes of flux tubes at the bottom of the convection zone, n_j pseudo-random numbers taken from a uniform distribution in the interval

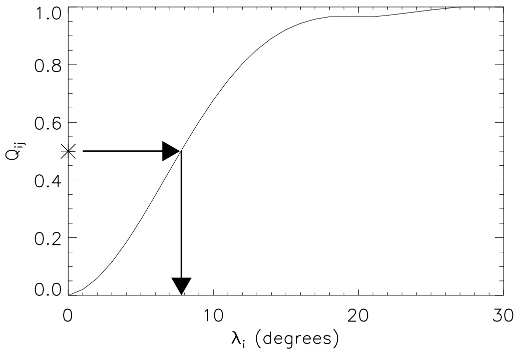

Figure 4.2: A sample probability density function, Q_{ij}, as a function of latitude, λ_i, at a given time t_j. For each erupting flux tube, a pseudo-random number is chosen uniformly in the interval [0,1] (the vertical axis), say 0.5. The latitude λ_i at which the flux tube erupts is then obtained by the mapping shown by the arrows.

$[0, 1]$ are mapped via the probability distribution function (PDF), Q_{ij}, based on p_{ij}:

$$Q_{ij} = \sum_{k=0}^{i} p_{kj} \tag{4.29}$$

The mapping for a sample PDF is illustrated in Fig. 4.2. n_j is set proportional to the total toroidal flux density, $\sum_i B_{ij}$, requiring the total number of erupting tubes per activity cycle (11 years) to be given by N, so that

$$n_j = \left[N \cdot \frac{\sum_i B_{ij}}{\sum_{i,j} B_{ij}} + 0.5 \right], \tag{4.30}$$

where the brackets indicate the largest integer that is smaller than or equal to the expression they enclose. N is set to 2100, which lead to a value for the total flux emerging over an activity cycle of the order of 10^{25} Mx, which is comparable with observations. Fig. 4.3 shows n_j as a function of time, with $B(\lambda, t)$ taken from the solar dynamo model given in Sect. 4.1.

Field strengths of erupting flux tubes

In order to determine the field strengths of erupting flux tubes, we consider the stability properties of flux tubes (Ferriz-Mas and Schüssler 1995) in the middle of the overshoot region (about 5000 km above the upper boundary of the radiative zone), according to the convection zone model including the overshoot region by Skaley and Stix (1991). We consider a Sun-like rotation, which is comparable to helioseismic observations (e.g.,

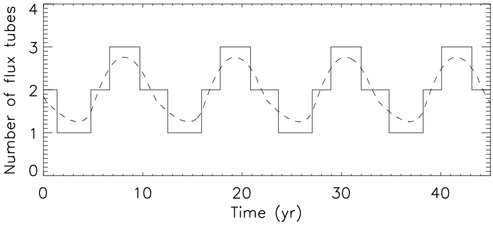

Figure 4.3: Number of flux tubes per time step (7 days), n_j, as a function of time. The dashed line shows the value in brackets of Eq. (4.30), and the full line shows n_j.

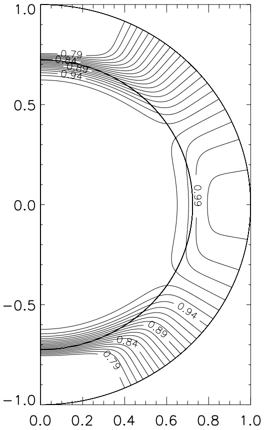

Figure 4.4: Meridional profile of internal rotation used in the stability analysis and flux tube simulations. Contours denote angular velocity, normalised to the equatorial value at the surface.

Schou et al. 1998), namely

$$\frac{\Omega(r,\theta)}{\Omega_0} = 0.9635 - \left[1 + \mathrm{erf}\left(\frac{r - r_0}{d_0}\right)\right] \cdot \left(0.0876\cos^4\theta + 0.0535\cos^2\theta - 0.0182\right), \quad (4.31)$$

where Ω_0 is the equatorial rotation rate at the surface, and d_0 roughly corresponds to the thickness of the tachocline. Lines of constant angular velocity are shown in Fig. 4.4. This 2D profile is consistent with the 1D profile in Eq. (4.1). We apply the stability criteria

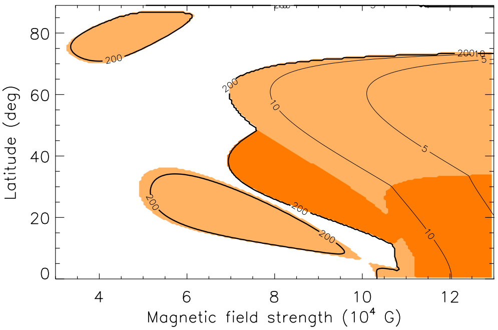

Figure 4.5: Stability diagram for thin flux tubes in the middle of the overshoot region, for Sun-like internal differential rotation (given by Eq. 4.31). White regions indicate stable flux tubes, while shaded areas indicate instability. For light-shaded areas, the fastest growing mode has azimuthal wave number $m = 1$, while for dark-shaded areas it is $m = 2$. Contours show lines of constant growth times (e-folding times), labelled in units of days.

of Ferriz-Mas and Schüssler (1995) to a model of the solar convection zone including the overshoot layer (Skaley and Stix 1991). Fig. 4.5 shows the stability diagram, as a function of flux tube latitude and field strength. Let $B_\tau(\lambda)$ be the field strength of Parker-unstable flux tubes as a function of latitude, corresponding to a certain growth time, τ, of the instability. In the course of the amplification of the toroidal magnetic field, we assume that toroidal flux tubes form out of the magnetic layer. When their field strength is above a certain threshold, Parker instability sets in with growth time τ. For most of the stability diagram (Fig. 4.5), τ decreases with increasing field strength. In the $\alpha\Omega$ dynamo model, the toroidal field amplification occurs in the time scale of the rotational shear in the tachocline, which is about a few years. As long as the growth time of the flux tube instability is longer than the shearing time scale, the toroidal field can continue to be amplified. As the field strength reaches a level (of order 10^5 G), the two time scales become comparable, so the flux tubes are immediately lost from the layer, limiting further growth of the dynamo intensification. Moreover, we do not consider tubes with growth times much longer than the amplification time scale, because they are intensified and thus have shorter growth rates for the instability. Hence we choose the field strengths of the flux tubes as given by the curve $B_{200}(\lambda)$, corresponding to $\tau = 200$ days. Choosing a growth time longer than this value does not change the results, because the curves of constant growth time get too close to each other near the stability limit (Fig. 4.5). We consider the contour line $B_{200}(\lambda)$ of the main region of instability in Fig. 4.5, which is a one-valued function of latitude. Taking field strengths corresponding to the closed curves to the left of the diagram do not lead to a significant difference in the emergence latitudes and tilt angles (Caligari et al. 1995).

We require that the mean toroidal field must be above 4% of the maximum mean field strength generated by the dynamo (equipartition field strength), in order to generate magnetic flux tubes. We have made this choice in order to avoid having flux tubes at very high latitudes.

An alternative procedure to determine the latitudes, field strengths, and probabilities of eruption is given in the Appendix.

4.2.2 The rise of flux loops

Having determined the times of emergence, initial latitudes, and the corresponding field strengths of the individual flux tubes (Sect. 4.2.1), we simulate the rise of unstable flux tubes throughout the convection zone. The simulations are made using the code developed by Moreno-Insertis (1986) and extended to three dimensions and spherical geometry by Caligari et al. (1995). In the numerical scheme, the flux tube is described by Lagrangian mass elements. The flux ring is treated as one-dimensional, but the mass elements can move in three dimensions (see Caligari et al. 1995).

The initial value for the cross-sectional radius of each flux tube is taken to be R_t = 1000 km. For $B = 10^5$ G, this corresponds to a magnetic flux of about $3 \cdot 10^{21}$ Mx, which is typical for a bipolar magnetic region (hereafter BMR) of a moderate size on the surface. The tube radius that we take is large enough for the drag force not to have a significant effect on the dynamics of rising flux loops (D'Silva and Choudhuri 1993, Caligari et al. 1995). In other words, the dynamics of flux tubes with $R_\mathrm{t} \gtrsim 1000$ km, with all the other parameters fixed, are not considerably different. Therefore, our simulations represent also the dynamics of tubes having more magnetic flux, for a given field strength.

The fastest growing modes of unstable flux tubes have azimuthal wavenumbers $m = 1$ or $m = 2$. On the other hand, the angular separation of large BMRs on the Sun corresponds to much larger azimuthal wavenumbers ($m = 10 - 60$). A possible resolution to this discrepancy could be that BMRs dynamically disconnect from their roots at depths of only a few Mm below the surface soon after the emergence, which limits the longitudinal separation (Schüssler and Rempel 2005).

In order to determine the emergence latitudes and tilt angles, we use a lookup table resulting from a large number of simulations for the dynamics of unstable flux tubes. The table entries are for given initial latitudes and magnetic field strengths. The initial latitudes are in 5°-steps, and the corresponding field strengths are obtained from the curve $B_{200}(\lambda)$, excluding the instability islands (Fig. 4.5). Bilinear interpolation is used to obtain the emergence latitudes and tilt angles as intermediate values of initial latitude and field strength. Fig. 4.6 shows a comparison of the dynamo-generated toroidal field (contour lines) and the surface emergence pattern of rising flux tubes (dots). The overall emergence pattern roughly coincides with the dynamo waves, because the poleward deflection of rising flux tubes is small for a slow rotator like the Sun. This result is consistent with the implicit assumption that is often made when interpreting solar dynamo models, namely that the surface activity pattern reflects the dynamo wave pattern.

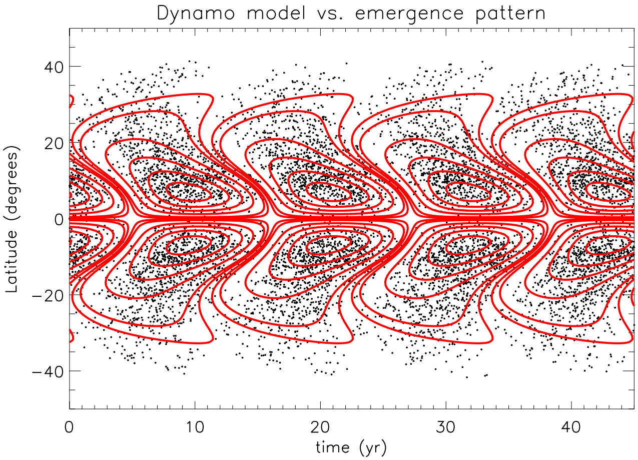

Figure 4.6: Time-latitude diagram of the dynamo-generated mean toroidal magnetic field $B(\lambda, t)$ at the bottom of the convection zone (contours) and of the flux loops emerging at the surface (dots) for a Sun-like star. The dynamo waves and the emergence pattern show a rather close match.

4.3 Surface flux transport

Emergence times, latitudes and tilt angles obtained in the previous steps determine the flux input into our surface flux transport simulation through the source term $S(\lambda, \phi, t)$ in Eq. (2.3). The model is described in the following Sects. 4.3.1-4.3.3. The emergence longitudes ϕ are assumed to be randomly distributed.

4.3.1 Treatment of source BMRs

The flux density of an emerging BMR is written in the form

$$B(\lambda, \phi) = B^{+}(\lambda, \phi) - B^{-}(\lambda, \phi), \tag{4.32}$$

where λ denotes the stellar latitude and ϕ the longitude. Following van Ballegooijen et al. (1998) and Baumann et al. (2004), we assume the unsigned field strength of the two polarities of a newly emerged BMR to be

$$B^{\pm}(\lambda, \phi) = B_0 \exp\left[-\frac{2\left[1 - \cos\beta_{\pm}(\lambda, \phi)\right]}{\delta_{\text{in}}^2}\right]. \tag{4.33}$$

Here, $\beta_{\pm}(\lambda, \phi)$ are the heliocentric angles between any given position (λ, ϕ) and the centre of the positive and negative polarities, $(\lambda_{\pm}, \phi_{\pm})$. The initial characteristic angular width

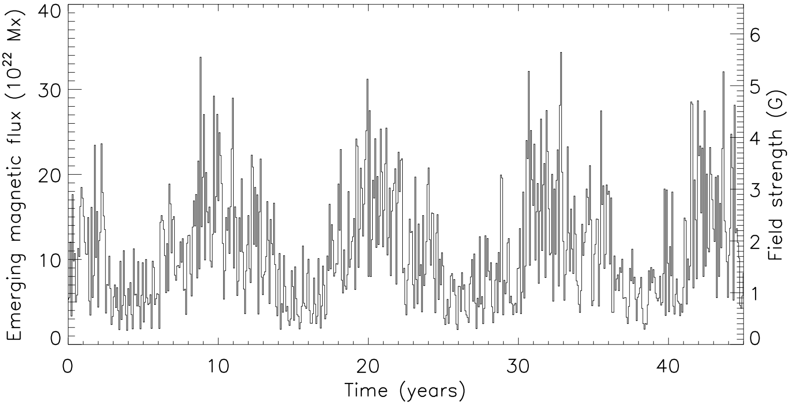

Figure 4.7: Time variation of the emerging magnetic flux integrated over the surface, and summed over 27-day time intervals. The corresponding total unsigned flux density scale is shown on the right-hand vertical axis.

of each polarity, $\delta_{\rm in}$, and the angular separation of the centres of the two poles, $\Delta\beta$ are related by $\delta_{\rm in} = 0.4\Delta\beta$. The maximum field strength B_0 is set to 250 G (see the discussion in Sect. 2.2).

BMRs which are smaller than the grid cell size of the simulations are taken into account by first considering such regions only at a later stage in their evolution, after having diffused to an angular width of $\delta_0 = 4°$. The description of the two polarities for such a BMR is thus given by

$$B^{\pm}(\lambda, \phi) = B_0 \left(\frac{\delta_{\rm in}}{\delta_0} \right)^2 \exp \left[- \frac{2\,[1 - \cos\beta_{\pm}(\lambda, \phi)]}{\delta_0^2} \right]. \tag{4.34}$$

4.3.2 Size distribution and the emerging magnetic flux

The total size of a BMR is related to the heliocentric angular separation of the centres of the two poles, $\Delta\beta$, which, in our model, ranges from 3.5° to 10° with a step width of 0.1°. The corresponding range of areas is 30-250 square degrees, and the resulting range of magnetic flux is $2.3 \cdot 10^{21}$-$3.5 \cdot 10^{22}$ Mx. The areas A of the bipolar source regions are determined randomly with a prescribed number distribution, $N(A) \sim A^{-2}$ (Schrijver and Harvey 1994).

The time series of emerging magnetic flux, summed over 27 days (one full solar rotation), is given in Fig. 4.7. It shows a cyclic variation with a period of about 11 years, determined by the dynamo model. The range of total unsigned flux density is similar to the one given by Baumann et al. (2004).

4.3.3 The surface evolution of magnetic flux

We follow the evolution of the surface field, resulting from the emergence of BMRs, as well as transport and diffusion. As in Chapter 2, we determine the time evolution of the surface field using the magnetic induction equation in the form

$$\frac{\partial B}{\partial t} = -\Omega(\lambda)\frac{\partial B}{\partial \phi} + \frac{1}{R_\star \cos\lambda}\frac{\partial}{\partial \lambda}\Big(v(\lambda)B\cos\lambda\Big) + \mathcal{D}_h(\eta_h) - \mathcal{D}_r(\eta_r) + S(\lambda,\phi), \quad (4.35)$$

where Ω is the angular rotation rate as a function of latitude λ (Eq. 2.4), v is the meridional flow (Eq. 2.5), $R_\star$ is the stellar radius, $\mathcal{D}_h$ is the term for horizontal diffusion with uniform turbulent diffusivity η_h, $\mathcal{D}_r$ denotes the radial diffusion term with uniform radial diffusivity η_r, and S is the source term describing the newly emerging BMRs (see Eq. 2.3). We consider the same numerical procedure as explained in Sect. 2.2. All transport parameters listed above are taken the same as in the solar reference model in Chapter 2. An animation of the evolving surface flux can be found under `http://www.solar-system-school.de/alumni/isik_movies/Bsurf_27d.gif`. The time-latitude diagram of the longitudinal (azimuthal) averages of the signed flux density is shown in Fig. 4.8a. The values are lower than those found by Baumann et al. (2004). The reason is that the tilt angles resulting from the rise of flux tubes are systematically smaller than the latitude dependence assumed by Baumann et al. (2004), but actually provide a better match to the observations (see Caligari et al. 1995, Fig. 12). The time variation of the total unsigned flux (and its density) is shown in Fig. 4.8b. For the evolving surface flux, the activity minima are less marked than for the emerging flux (Fig. 4.7); this is due to the phase difference of about half a period between the variations of the polar flux and the flux emerging at low latitudes. Polar fields are naturally built up by the surface flux transport. At the maximum of BMR emergence, poleward meridional flow and turbulent diffusion of tilted BMRs lead to a net flux transport towards the poles, such that the poloidal fields reach a maximum at about the minimum of BMR emergence.

4.4 Rapidly rotating Sun-like stars

We apply the combined model of magnetic flux generation and transport to rapidly rotating stars, assuming them to have Sun-like internal structure. The only parameter that we vary is the equatorial rotation rate at the surface, $\Omega_{0\star}$. The velocity fields and turbulent magnetic diffusivities for the dynamo region, the convection zone, and the surface are all assumed to be the same as in the reference model of the Sun in the previous sections. The difference between the minimum and maximum angular velocities in the convective envelope, $\Delta\Omega$, is taken to be independent of $\Omega_{0\star}$, according to observations of rapidly rotating cool stars (e.g., Barnes et al. 2005). This corresponds to a decrease of $\Delta\Omega/\Omega_{0\star}$ by a factor $\Omega_{0\star}/\Omega_{0\odot}$ with respect to the solar value, so that the constants on the right hand side of Eq. (4.31) are multiplied by $\Omega_{0\odot}/\Omega_{0\star}$. Because $\Delta\Omega \equiv \Omega_{\rm eq} - \Omega_{\rm pole}$ is kept constant, the surface flux transport equation (2.3) and thus Eq. (2.4) remains unchanged.

In order to describe the scaling of α, we consider a rising blob of gas with velocity $\mathbf{v}$ and a characteristic length scale l. In the reference frame rotating with $\mathbf{\Omega}_\star$, the Coriolis is $-2\mathbf{\Omega}_\star \times \mathbf{v}$. If we think of the rising plume as part of a turbulent fluid, we may assume

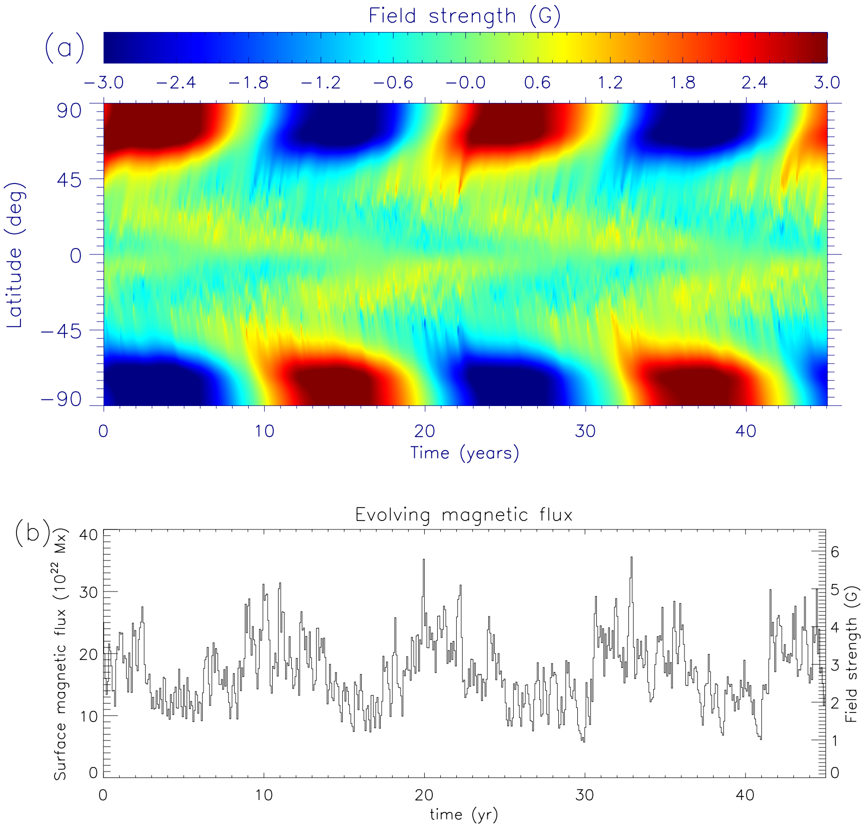

Figure 4.8: (a) Time-latitude diagram of the azimuthally averaged strength of the radial surface magnetic field for the solar model. (b) Time variation of the total unsigned surface magnetic flux. The values are averaged over 27-day time intervals.

that its velocity correlation with the surroundings vanishes after a time τ_c. The velocity induced by the Coriolis acceleration is then on the order $\Omega_\star v\tau_c$. Using the definition of α from the first-order smoothing approximation of mean-field hydrodynamics (Krause and Rädler 1980), we obtain

$$\begin{aligned} |\alpha| &\approx \tau_c\langle \mathbf{v}\cdot(\nabla\times\mathbf{v})\rangle \\ &\approx \tau_c v\cdot\left(l^{-1}\Omega v\tau_c\right) = \Omega l. \end{aligned} \tag{4.36}$$

Since we have taken $\Delta\Omega$ as independent of $\Omega_\star$, the Reynolds number for radial shear, R_Ω,

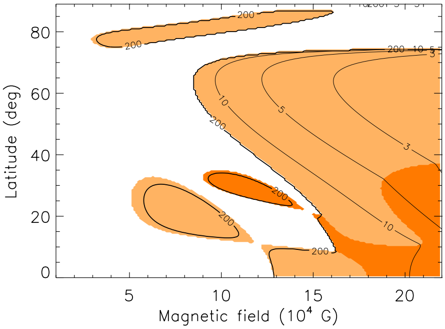

Figure 4.9: Stability diagram for the undulatory instability of flux tubes located in a Sun-like star with $P_{\rm rot} = 10$ d.

in Eq. (4.10) is unaltered, but the Reynolds number for the α-effect, R_α, is proportional to $\Omega_\star$, according to Eq. (4.36). Thus we take the maximum strength of the α-effect, α_0, to be proportional to the stellar equatorial rotation rate, $\Omega_{0\star}$. In our dynamo model, the dynamo cycle period, $P_{\rm cyc}$, is then inversely proportional to $\Omega_{0\star}$.

The total number of erupting flux tubes per activity cycle, N, is also scaled with $\Omega_{0\star}$, in accordance with the observed relation between rotation rate and the level of magnetic activity (e.g., Montesinos et al. 2001).

4.4.1 $P_{\rm rot} = 10$ d

We consider a Sun-like star with a rotation period of 10 d, which corresponds to a rotation rate of about $\Omega_\star = 2.7\Omega_\odot$. Fig. 4.9 shows the stability diagram of flux tubes located at the middle of the overshoot region. The critical field strength for Parker instability is larger than in the solar case: increasing the stellar rotation rate has a stabilising effect on the flux tubes. With increasing $\Omega_\star$, angular momentum conservation restricts the tube displacements to the direction parallel to the rotation axis, so that the magnetic buoyancy needs to be higher than in a similar situation in the Sun.

In determining the function $B_{200}(\lambda)$, we exclude the islands of instability seen in Fig. 4.9, for the same reason explained in Sect. 4.2: we have made test simulations for rising flux tubes having λ and B corresponding to these 'islands', and found that the resulting emergence latitudes and tilt angles do not show a significant dependence on field strength, between the island and the neighbouring part of the main region of instability.

The patterns of toroidal field and the flux emergence are shown in Fig. 4.10. In this case, the poleward deflection of rising flux tubes is stronger than in the case of the Sun. The responsible effect is the component of the Coriolis force directed towards the rotation axis (resulting from a retrograde flow along the flux tube in order to conserve angular momentum of a rising tube), which is proportional to the rotation rate.

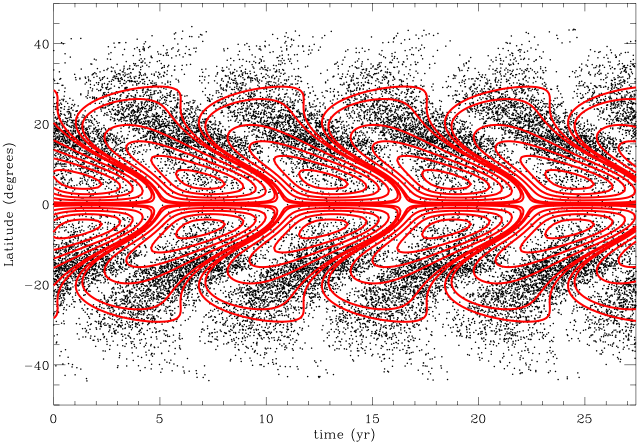

Figure 4.10: Time-latitude diagram of the dynamo-generated mean toroidal magnetic field at the bottom of the convection zone (contours) and of the flux tubes emerging at the surface (dots) for a Sun-like star with $P_{\rm rot}$ = 10 d.

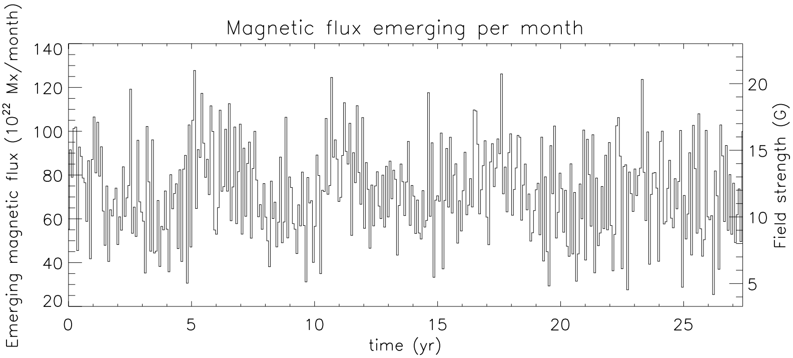

Figure 4.11: Time variation of the total emerging magnetic flux, summed over 27-day time intervals for a Sun-like star with $P_{\rm rot}$ = 10 d.. The corresponding total unsigned flux density scale is shown on the right-hand vertical axis.

The emerging magnetic flux, summed over one-month intervals is shown in Fig. 4.11. It shows a cyclic variation with the dynamo period of about 5 years. This is about half the length of the solar cycle. While the total flux input is about 5 times larger than in the solar case, the variation between the minimum and maximum emerging flux is

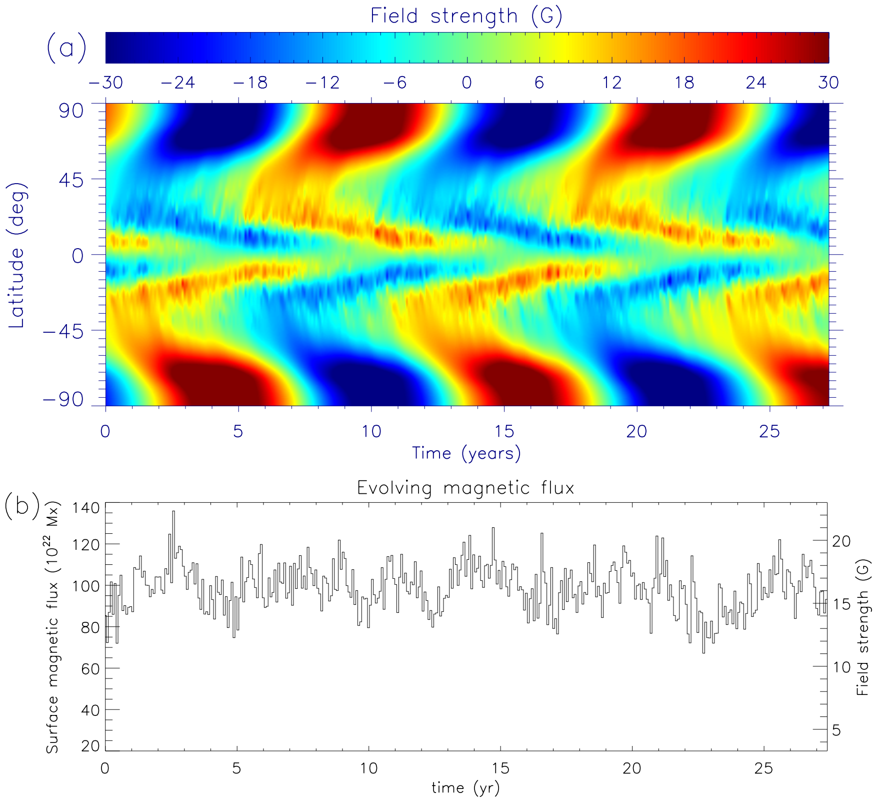

Figure 4.12: (a) Time-latitude diagram of the azimuthally averaged strength of the radial surface magnetic field for a Sun-like star with $P_{\rm rot}$ = 10 d. (b) Time variation of the total unsigned surface magnetic flux. The values are averaged over 27-day time intervals.

considerably smaller. This results from the stronger overlapping between consecutive cycles, which is a consequence of larger dynamo excitation. As shown in Fig. 4.12a, we have strong polar fields (note the different saturation level of the colour table, as compared to Fig. 4.8a). This is due to 1) higher emergence rate, 2) larger tilt angles owing to faster rotation. Larger tilt angles are caused by a larger Coriolis force experienced by the horizontally expanding crest of the tube. It is evident from the animation[2] of the surface field distribution that, although the flux emerges within a rather restricted latitude range, strong fields are spread over the entire surface by means of large-scale surface flows. There are unipolar magnetic regions near the poles and mixed-polarity regions

---

[2] `http://www.solar-system-school.de/alumni/isik_movies/Bsurf_10d.gif`

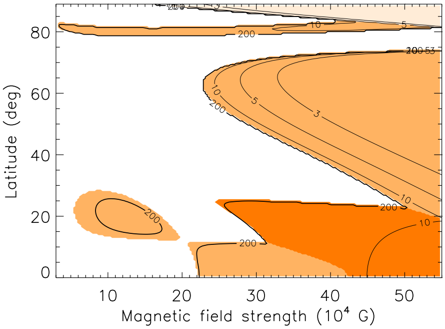

Figure 4.13: Stability diagram for the undulatory instability of flux tubes located in a Sun-like star with $P_{\mathrm{rot}} = 2$ d.

emerging at low to middle latitudes. Figure 4.12b shows that the cycle signal introduced by the underlying dynamo is no longer clearly observable when we consider the evolving surface magnetic flux. The reasons are 1) a larger degree of overlap between consecutive cycles owing to a stronger α-effect, and 2) strong polar magnetic fields in antiphase with the emerging flux.

4.4.2 $P_{\mathrm{rot}} = 2$ d

For a star with a rotation period of two days ($\Omega_\star \approx 13\Omega_\odot$), the stabilising effect of rotation is even stronger than in the previous case, as shown in Fig. 4.13. As before, we exclude the instability islands in determining the field strengths of flux tubes. Simulations of flux tube rise show that perturbations perpendicular to the rotation axis are largely suppressed, so the instability develops along the direction parallel to the rotation axis. As a result, an azimuthal wavenumber of $m = 1$ corresponds to a precessing flux ring around the rotation axis. Once a loop is formed, it rises almost parallel to the rotation axis and emerges at a significantly higher latitude than its original location. The start latitudes are in the range of roughly 0°-25° and the emergence latitudes at about 23°-40°. Fig. 4.14 shows a comparison of the dynamo-generated magnetic field and the distribution of flux tubes emerging at the surface. It is evident that the poleward deflection of flux tubes causes a significant difference between the dynamo waves and the pattern of surface emergence. The lack of emerging tubes in the latitude interval between the equator and $|\lambda| \simeq 23°$ occurs because flux tubes generated very close to the equator emerge already at this latitude.

For such a rapidly rotating star, the tilt angles of emerging bipolar regions are much larger (around 35°) than in the solar case, leading to two latitudinal belts of opposite magnetic polarity[3] Meridional transport of the high-latitude belt leads to strong polar fields, reaching field strengths up to 30 G, compared to a few gauss for the solar poles. The

---

[3] See `http://www.solar-system-school.de/alumni/isik_movies/Bsurf_2d.gif`.

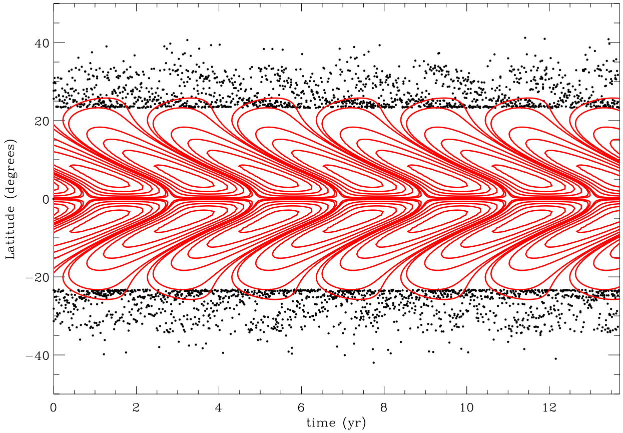

Figure 4.14: Time-latitude diagram of the dynamo-generated mean toroidal magnetic field at the bottom of the convection zone (contours) and of the flux tubes emerging at the surface (dots) for a Sun-like star with $P_{\rm rot} = 2$ d. The dots are shown for one-month intervals. The emergence pattern is completely different from the dynamo wave.

presence of “polar spots” observed in fast rotators can thus be explained by the emergence and meridional transport of bipolar regions at mid-latitudes with tilt angles as high as 35° (see also Schrijver and Title 2001 and Chapter 2).

4.5 Discussion

The dynamo model considered here is a simple example for the kind of dynamo processes which may be relevant for rapidly rotating cool stars. As a consequence of our assumption about the scaling of the dynamo strength with rotation (Eq. 4.36), the cycle frequency increases with $\Omega_\star$. As the cycle length decreases, it limits the maximum magnetic flux that can be built up in the polar regions of the surface. Therefore, the polar field strength does not change considerably as we change the rotation period from 10 d to 2 d, despite that flux input per cycle is increased by a factor of 5, and the tilt angles become larger. As a result, the lifetimes of polar magnetic regions on fast rotators might be determined by the dynamo frequency, rather than by the turbulent diffusion time, as in the case of isolated bipolar regions (Chapter 2).

The dynamo-generated toroidal field at the base of the convection zone is limited to low latitudes, between the equator and ±20°-30° in all the three cases. The reason is the assumed profile of the α-effect (Eq. 4.2 and Fig. 4.1), which is confined to this latitude range. In the case of the Sun, the assumption was based on the α-effect caused by flux tube instabilities (Ferriz-Mas et al. 1994) or by magnetostrophic waves (Schmitt 2003). This was strictly required in our model to have equatorward propagating dynamo waves.

For faster rotating Sun-like stars, we assumed the same Sun-like profiles for both $\alpha(\theta)$ and the radial shear, $\Omega'(\theta)$. Incorporation of a dynamo model having different spatio-temporal properties would lead to different results for the evolution of surface magnetic flux.

We find strong polar magnetic regions (cf., Schrijver and Title 2001, Işık et al. 2007) for rotation periods of 10 d and 2 d, in addition to low- and mid-latitude activity. For $P_{\rm rot} = 10$ d, the surface flux transport blurs the periodic signal from the dynamo model. This indicates that for rapid rotation, a cyclic dynamo may be hidden in a non-cyclic surface activity, which is caused by the combined effects of the dynamo (cycle overlapping), large tilt angles, and the meridional transport. Furthermore, for $P_{\rm rot} = 2$ d we have found that the dynamo wave pattern and the emerging surface flux are completely different, owing to the strong poleward deflection of rising flux tubes by the Coriolis force. Consequently, the observed activity patterns on the surface may not represent the spatio-temporal distribution of magnetic field in the deep interior. This means that models of the deep-seated dynamo for rapidly rotating cool stars should take into account the poleward deflection of the emerging magnetic flux.

It should be kept in mind that in all the particular results which we have obtained for rapidly rotating stars, there are two sources of ambiguity:

- For cool stars more active than the Sun, much less is known about the dynamo mechanism and the various processes of magnetic flux transport. Present observations do not have the sufficient spatial resolution and time coverage to constrain the combined models of magnetic field dynamics.

- The value of $\eta_h = 600$ km^2 s^{-1} represents the average value of turbulent magnetic diffusivity at the solar surface and it is consistent with the observations (Wang et al. 1989a). For more active stars, however, we do not know the supergranular flow pattern, if any, and its coupling with the magnetic structures on the surface.

4.6 Conclusions

We have developed a consistently coupled model of magnetic field generation and transport in the Sun and other cool stars. In the framework of our coupled models of flux transport, there are two major improvements in comparison to previous studies:

- We determine the cycle properties by an underlying dynamo model, whereas in previous studies of cyclic surface flux transport either butterfly diagrams were prescribed arbitrarily, or observed emergence patterns were used.

- The tilt angles of emerging regions are not prescribed, but consistently determined from simulations of rising flux tubes. The results reproduce the observed latitude dependence and this provides a physical mechanism for the tilt angles of BMRs.

Our investigation shows that the tilt angle of BMRs is a very important quantity both in slow rotators like the Sun and in rapid rotators, since it strongly affects the evolution of the surface magnetic flux and the strength of the polar magnetic fields. The strength of polar fields depends also on the dynamo cycle period, which is determined by the strength of the α-effect. The assumed linear dependence of the α-effect on the rotation rate limits the maximum polar field strength for stars rotating considerably faster than the Sun. Regardless of that assumption, for very fast rotating stars, the surface magnetic field distribution can be very different compared to the toroidal field distribution as determined from the deep-seated dynamo.

5 Outlook

A unified model which fully incorporates various physical aspects of the hydromagnetic dynamo problem for a highly complex system such as the Sun remains to be one of the unsolved problems of astrophysics, whereas even much less is known about dynamos of other magnetically active stars.

In the present dissertation, I have first investigated, through numerical simulations, two aspects of magnetism in cool stars: the effects of large-scale surface flows on magnetic regions of cool stars, and the effects of external flows on the storage of magnetic flux tubes in the deep convective overshoot layer of the Sun.

The effects of large-scale surface flows on the lifetimes of starspots have been revealed in Chapter 2 and the existence of polar spots have been explained on the basis of surface flux transport. Further studies on these lines will follow within the framework of the coupled models of magnetic flux generation and transport (Chapter 4).

The interaction of external flows with magnetic flux tubes in the overshoot region will be further investigated in an upcoming study, based on the findings presented in Chapter 3. The nature of the friction-induced instability and its effects on the storage of flux tubes in the overshoot region will be considered in more detail.

I have developed a combined model of generation, emergence, and surface transport of stellar magnetic flux (Chapter 4). The model has a significant potential for applications aiming to understand the structure and evolution of magnetic fields in cool stars. For instance, different deep-seated dynamo models for stars can be tested with our model in order to “see” what would happen on the surface and to compare with observations.

As next steps to improve the coupled model of magnetic flux generation and transport, I plan to quantify the loss of magnetic flux from the dynamo layer in a consistent manner and consider it in the dynamo equations as a nonlinear term. Furthermore, I intend to develop a scheme which includes the evolving surface flux into a two dimensional flux transport dynamo as the source of the poloidal component at the bottom of the convection zone. There are two goals in this plan: the first is to improve our understanding of the solar dynamo, and the second is to extend the model to cool stars in wide ranges of mass and age.

A An alternative treatment of flux loss

Instead of assuming $B(\lambda, t)$ given by the dynamo model to determine the eruption probability of flux tubes, one can also choose the growth rate of Parker instability. When the field B exceeds a critical value $B_0(\lambda)$, Parker instability sets in, giving rise to an erupting flux loop. The function $B_0(\lambda)$ is determined by a constant growth time (e-folding time), which we choose here to be 200 days, for the reasons explained in Chapter 4.

The initial field strength of a flux tube at a certain latitude λ and time t is given by $B(\lambda, t)$ from the dynamo model. The critical field strength for the onset of nonlinear flux loss, B_0, is taken to be 10^5 G in the case of the Sun, which is the average field strength of the onset of the instability at the location of the dynamo layer. This corresponds to a flux of about $3 \cdot 10^{21}$ Mx, which is a typical value for a small/moderate sized active region on the Sun.

Dynamo model

In order to characterise the removal of magnetic flux from the dynamo region by erupting flux tubes, we add the term

$$\frac{B_0}{\tau} f(B/B_0)$$

to the right hand side of Eq. (4.5), following Schmitt and Schüssler (1989). Here, B_0 is the critical mean field strength, above which the flux is lost from the layer, at a rate τ^{-1}. The function f describes the B-dependence of the flux loss in the form

$$f\left(\frac{B}{B_0}\right) = \begin{cases} -\mathrm{sgn}(B) \cdot \left(\frac{B}{B_0} - 1\right)^2 & : \quad \text{if } B \geq B_0 \\ 0 & : \quad \text{otherwise.} \end{cases} \tag{A.1}$$

With this choice of the flux loss function, the dynamo equation for the toroidal field becomes nonlinear. The flux loss time scale, τ, actually depends on the amount of magnetic flux in the storage region. After non-dimensionalisation of the dynamo equations, the nonlinear term becomes $Q \cdot f(B)$, where Q represents the strength of flux loss. Its value is set to 400, in order to have a maximum field strength of $2 \cdot 10^5$ G, which yields a growth time for the undulatory instability of magnetic flux tubes of about 2.2 days. The turbulent magnetic diffusivity is set to $\eta = 2.5 \cdot 10^{11}$ cm^2 s^{-1}, such that the dynamo cycle period becomes 22 years.

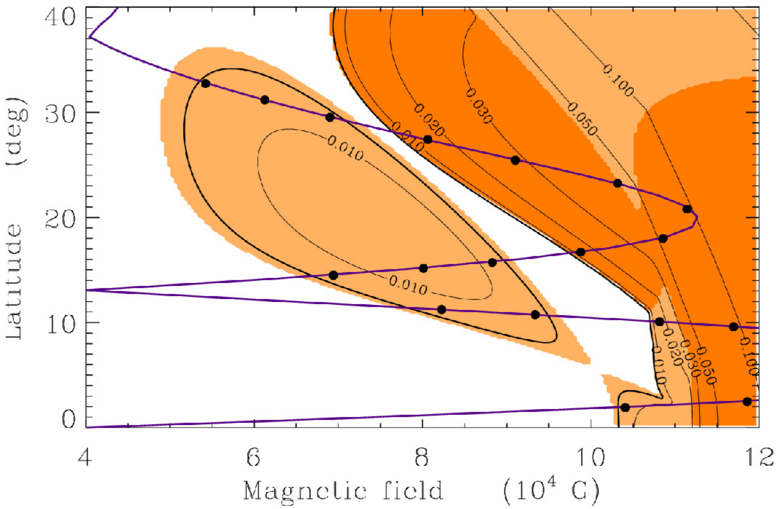

Figure A.1: The determination of the growth rate distribution g_{ij} of flux tubes at a certain time. The contour lines denote the growth rate g_{ij} of the instability (in units of d^{-1}). The limit growth rate of $g_0 = 5 \cdot 10^{-3}\ \mathrm{d}^{-1}$, which corresponds to a growth time of 200 days, is indicated by a thick contour. The blue curve is a snapshot of the magnetic field strength as a function of latitude. The filled circles indicate sample values of field strength and latitude for which g_{ij} is determined.

The latitudes and the number of erupting flux tubes

Flux tubes are assumed to emerge with a probability proportional to the growth rate of the Parker instability, $g(\lambda, t)$, resulting from the evolution of the toroidal field component $B(\lambda, t)$ in the dynamo model.

We determine $g(\lambda_i, t_j) \equiv g_{ij}$ at timestep t_j and latitude interval λ_i. The domain λ_i of g_{ij} is defined by the subdomain of $B(\lambda, t)$ for which $g_{ij} \geq g_0$, where g_0 is the lower growth rate limit of $5 \cdot 10^{-3}\ \mathrm{d}^{-1}$, which corresponds to a growth time of 200 days. This operation establishes a criterion to choose the unstable flux tubes, such that the growth time of the instability has to be shorter than 200 days. The procedure is illustrated in Fig. A.1. Snapshots of magnetic field distributions throughout one cycle is shown in Fig. A.2. The maximum field strength of the cycle is determined by the nonlinear flux loss by buoyant rise of flux tubes. The resulting function $g(\lambda_i, t_j)$ is plotted in Fig. A.3, along with the dynamo contours. The figure shows the correspondence between the strength of the dynamo-generated toroidal field and the growth rate of undular instabilities of the associated flux tubes. At time t_j, the probability for *one* flux tube to erupt at the latitude

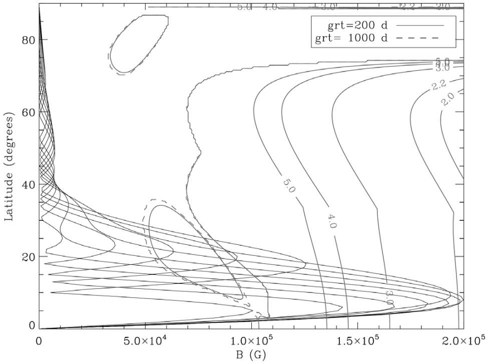

Figure A.2: Stability diagram for flux tubes in the reference case, $\Omega = \Omega_\odot$ (see Fig. 4.5). Snapshots of the magnetic field distribution $B(\lambda, t)$ of the dynamo model are overplotted. $B_0 = 10^5$ G, $B_{\max} = 2.0 B_0$ and $g_{\max} = 0.46/d$.

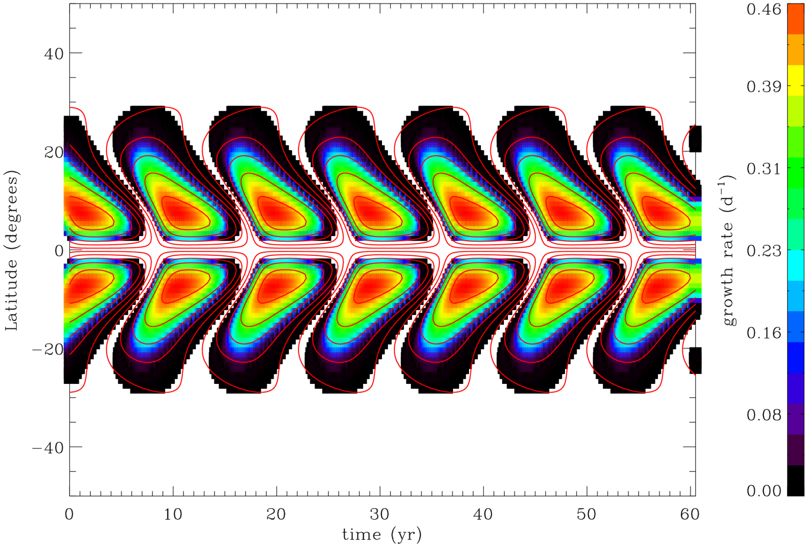

Figure A.3: Growth rate of the Parker instability, $g(\lambda, t)$ (shown with the colour code), as a function of latitude and time. Contours show the magnetic field strength, $B(\lambda, t)$, given by the dynamo model. The contour levels correspond to 0.2, 0.6, 1.0, 1.4, and 1.8 times the critical field strength, B_0, for the onset of Parker instability.

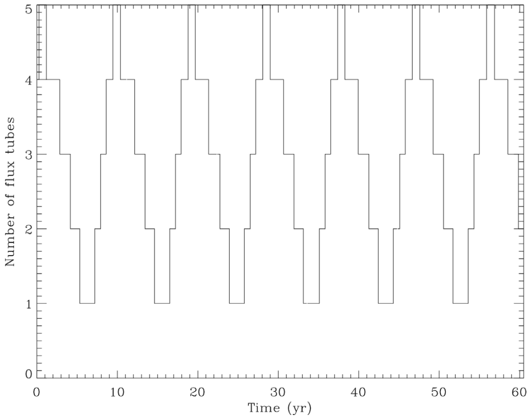

Figure A.4: Number of flux tubes per time step (10 days), $[n_j]$, as a function of time.

λ_i is given by

$$p_{ij} = \frac{g_{ij}}{\sum_i g_{ij}}. \tag{A.2}$$

At every time step t_j, n_j pseudo-random numbers with uniform distribution in $[0, 1]$ are mapped via the probability distribution function (PDF), Q_{ij}, based on p_{ij}:

$$Q_{ij} = \sum_{k=0}^{i} p_{kj} \tag{A.3}$$

For each flux tube to be generated, a new random number is determined. The number of flux tubes, n_j, to be generated at time step t_j (thus the number of random values) is proportional to the summed growth rates at the same step, $\sum_i g_{ij}$, requiring the total number of tubes per activity cycle (11 years) to be given by N, so that

$$n_j = \left[N \cdot \frac{\sum_i g_{ij}}{\sum_{i,j} g_{ij}} + 0.5 \right], \tag{A.4}$$

where the value between brackets is rounded to the largest integer that is smaller than or equal to the expression they enclose. The number of emerging flux tubes, n_j, per time step (taken as 10 days) is shown as a function of time in Fig. A.4.

Having determined the initial latitudes and field strengths at each time step, the emergence latitudes are obtained with the method described in Sect. 4.2.2. The latitudes before and after flux tube eruptions are shown in Fig. A.5. The resulting emergence pattern does not exhibit a marked difference with respect to the corresponding one in Chapter 4, except that the highest latitude is smaller by about 10° in the present case. The difference is how the link between the dynamo model and the distribution of erupting flux tubes is made in

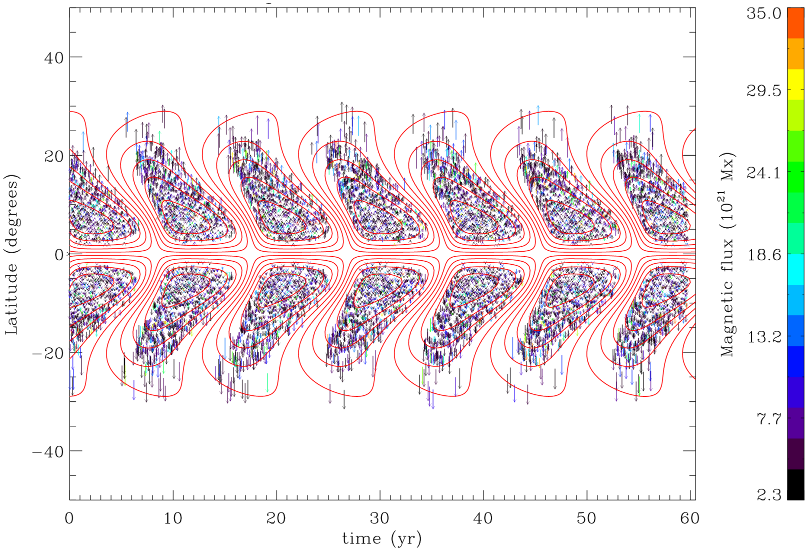

Figure A.5: The butterfly diagram showing the initial and the final latitudes of the emerging flux loops. The beginning of each arrow represents the initial latitude of the flux tube, and the tip of an arrow indicates the emergence latitude.

the coupled models. The variations of the emerging unsigned magnetic flux and the total unsigned surface flux at a time are shown in Figs. A.6 and A.7. A comparison with the corresponding variations in Chapter 4 shows no significant difference between the results of the two methods.

Application for $P_{\rm rot}$ =10 d

For a star with the same internal structure as the Sun, and rotating 2.6 times faster, we follow the same procedure as in the reference case above. We assume that increasing the rotation rate by 2.6 times corresponds to increasing α_0 by the same factor. This leads to a decrease of the dynamo cycle period by about a factor of two. The only other quantity that is different with respect to the previous case is the critical field strength for the onset of Parker instability, B_0, which is now about $1.5 \cdot 10^5$ G. Because faster rotation rate changes the stability properties of flux tubes in the overshoot region. Except for the determination procedure of the initial latitudes and times of eruption, the rest of the method is the same as described in Sect. 4.4. The stability diagram with a few snaphots of the magnetic field distribution is given in Fig. A.8. The function $g(\lambda_i, t_j)$ is plotted along with the dynamo contours in Fig. A.9. The initial and emergence latitudes of flux tubes are shown in Fig. A.10. Comparison with the reference case (Fig. A.5) reveals that the poleward

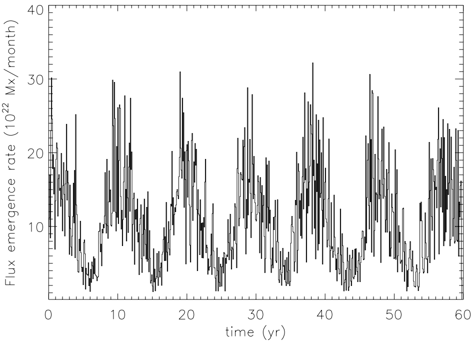

Figure A.6: Emerging unsigned magnetic flux per month, as a function of time for the reference case.

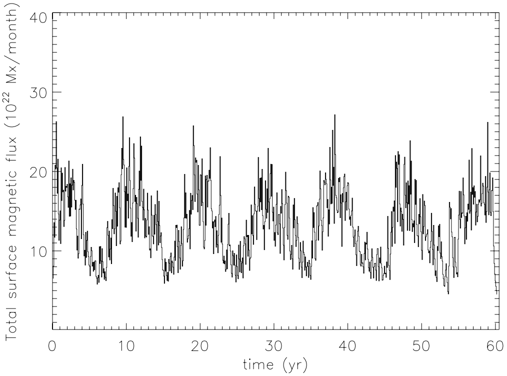

Figure A.7: The total unsigned magnetic flux on the surface of the reference star, integrated over 27-day time intervals.

deflection is larger in this case. Finally, in Figs. A.11-A.12, we show the variations of the emerging and total unsigned magnetic fluxes at the surface.

Comparisons of the figures in this appendix with the corresponding ones in Chapter 4 reveals that the results do not depend significantly on the method chosen to treat the flux loss from the dynamo layer. In a future study, the nonlinear coupling of the flux loss with the dynamo will be further developed.

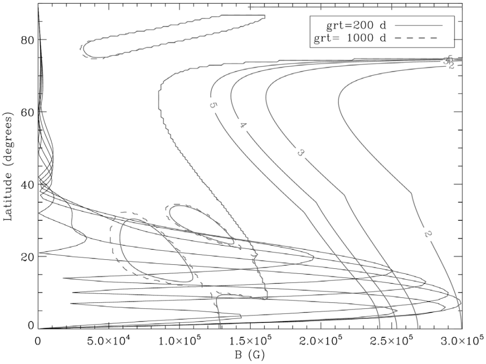

Figure A.8: Stability diagram for flux tubes in the star with $P_{\rm rot} = 10$ d ($\Omega = 2.6\ \Omega_\odot$). Snapshots of the magnetic field distribution $B(\lambda, t)$ of the dynamo model are overplotted. $B_0 = 1.5 \cdot 10^5$ G, $B_{\rm max} = 2.0 B_0$ and $g_{\rm max} = 0.52/d$.

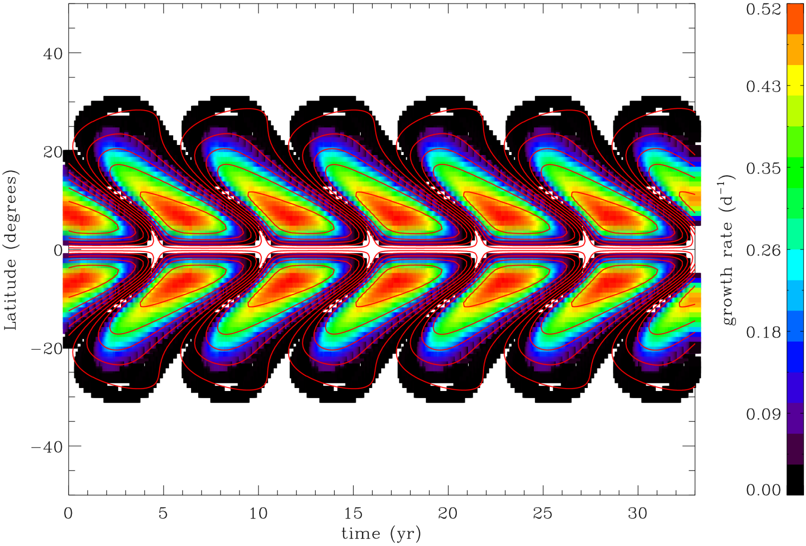

Figure A.9: Same as Fig. A.3, for the star with $P_{\rm rot}$ =10 d.

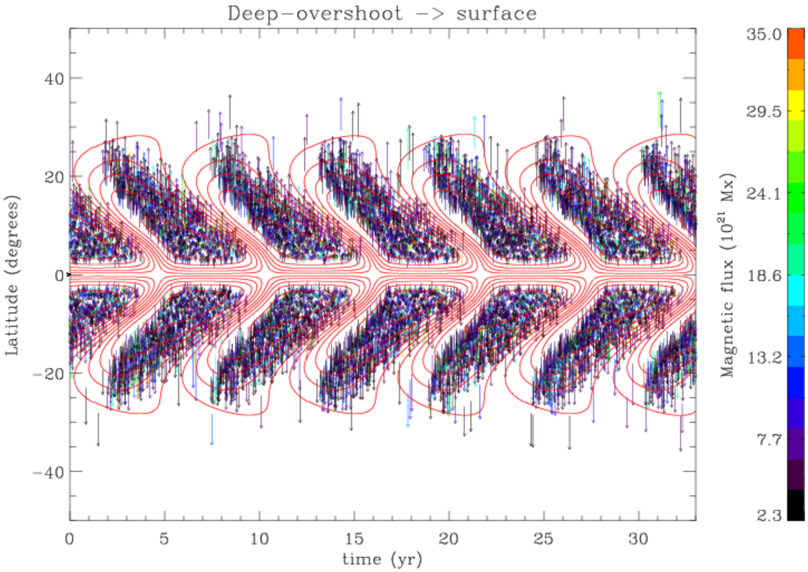

Figure A.10: Same as Fig. A.4 and Fig. A.5, but for the star with P_{rot} =10 d.

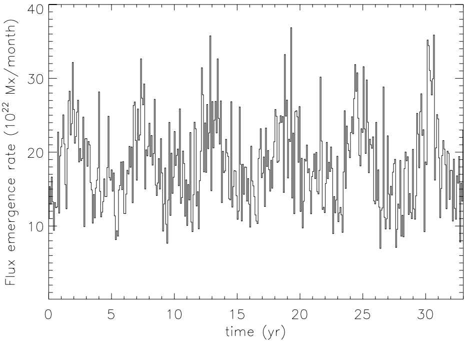

Figure A.11: Emerging magnetic flux per month, as a function of time for the case of P_{rot} = 10 d. The values are integrated over 27-day intervals.

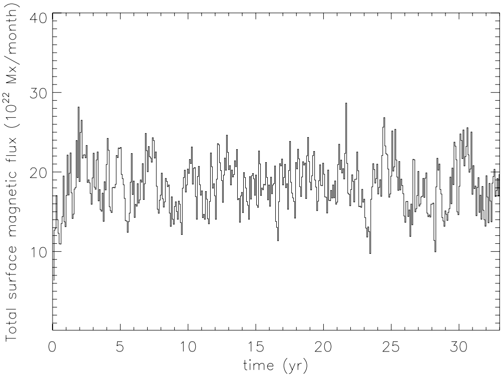

Figure A.12: The total unsigned magnetic flux on the surface of the star with $P_{\mathrm{rot}} = 10$ d, averaged over 27-day time intervals.

Bibliography

Ambruster, C. W., Fekel, Jr., F. C., Brown, A., 2003, The Radii of Solar Neighborhood ZAMS Stars, in The Future of Cool-Star Astrophysics: 12th Cambridge Workshop on Cool Stars, Stellar Systems, and the Sun, eds. A. Brown, G.M. Harper, and T.R. Ayres, (University of Colorado), 2003, p. 912

Barnes, J. R., Collier Cameron, A., Unruh, Y. C., Donati, J. F., Hussain, G. A. J., 1998, Latitude distributions and lifetimes of star-spots on G dwarfs in the alpha Persei cluster, Mon. Not. Royal Astron. Soc., 299, 904

Barnes, J. R., Cameron, A. C., Donati, J.-F., James, D. J., Marsden, S. C., Petit, P., 2005, The dependence of differential rotation on temperature and rotation, Mon. Not. Royal Astron. Soc., 357, L1, `arXiv:astro-ph/0410575`

Batchelor, G. K., 1967, Fluid dynamics, Cambridge, England, Cambridge University Press

Baumann, I., 2005, Magnetic flux transport on the Sun, PhD thesis, Universität Göttingen

Baumann, I., Schmitt, D., Schüssler, M., Solanki, S. K., 2004, Evolution of the large-scale magnetic field on the solar surface: A parameter study, Astron. & Astrophys., 426, 1075

Baumann, I., Schmitt, D., Schüssler, M., 2006, A necessary extension of the surface flux transport model, Astron. & Astrophys., 446, 307

Brandenburg, A., Subramanian, K., 2005, Astrophysical magnetic fields and nonlinear dynamo theory, Phys. Rep., 417, 1, `arXiv:astro-ph/0405052`

Caligari, P., Moreno-Insertis, F., Schussler, M., 1995, Emerging flux tubes in the solar convection zone. 1: Asymmetry, tilt, and emergence latitude, Astrophys. J., 441, 886

Caligari, P., Schüssler, M., Moreno-Insertis, F., 1998, Emerging Flux Tubes in the Solar Convection Zone. II. The Influence of Initial Conditions, Astrophys. J., 502, 481

Charbonneau, P., 2005, Dynamo Models of the Solar Cycle, Living Reviews in Solar Physics, 2, 2

Defouw, R. J., 1976, Wave propagation along a magnetic tube, Astrophys. J., 209, 266

Deluca, E. E., Fan, Y., Saar, S. H., 1997, The Emergence of Magnetic Flux Loops in Sunlike Stars, Astrophys. J., 481, 369

Dikpati, M., Charbonneau, P., 1999, A Babcock-Leighton Flux Transport Dynamo with Solar-like Differential Rotation, Astrophys. J., 518, 508

Dikpati, M., Choudhuri, A. R., 1995, On the Large-Scale Diffuse Magnetic Field of the Sun, Solar Phys., 161, 9

Donahue, R. A., Dobson, A. K., Baliunas, S. L., 1997, Stellar Active Region Evolution - I. Estimated Lifetimes of Chromospheric Active Regions and Active Region Complexes, Solar Phys., 171, 191

Donati, J.-F., Collier Cameron, A., Hussain, G. A. J., Semel, M., 1999, Magnetic topology and prominence patterns on AB Doradus, Mon. Not. Royal Astron. Soc., 302, 437

Donati, J.-F., Cameron, A. C., Semel, M., Hussain, G. A. J., Petit, P., Carter, B. D., Marsden, S. C., Mengel, M., López Ariste, A., Jeffers, S. V., Rees, D. E., 2003a, Dynamo processes and activity cycles of the active stars AB Doradus, LQ Hydrae and HR 1099, Mon. Not. Royal Astron. Soc., 345, 1145

Donati, J.-F., Collier Cameron, A., Petit, P., 2003b, Temporal fluctuations in the differential rotation of cool active stars, Mon. Not. Royal Astron. Soc., 345, 1187, `astro-ph/0307448`

Dorch, S. B. F., Nordlund, Å., 2001, On the transport of magnetic fields by solar-like stratified convection, Astron. & Astrophys., 365, 562

D'Silva, S., Choudhuri, A. R., 1993, A theoretical model for tilts of bipolar magnetic regions, Astron. & Astrophys., 272, 621

Eker, Z., 1999, Reliability of Light Curves for Photometric Imaging, Astrophys. J., 512, 386

Fan, Y., 2001, Nonlinear Growth of the Three-dimensional Undular Instability of a Horizontal Magnetic Layer and the Formation of Arching Flux Tubes, Astrophys. J., 546, 509

Fan, Y., 2004, Magnetic Fields in the Solar Convection Zone, Living Reviews in Solar Physics, 1, 1

Ferriz-Mas, A., Schüssler, M., 1993, Instabilities of magnetic flux tubes in a stellar convection zone. I. Equatorial flux rings in differentially rotating stars, Geophysical and Astrophysical Fluid Dynamics, 72, 209

Ferriz-Mas, A., Schüssler, M., 1995, Instabilities of magnetic flux tubes in a stellar convection zone. II. Flux rings outside the equatorial plane, Geophysical and Astrophysical Fluid Dynamics, 81, 233

Ferriz-Mas, A., Schmitt, D., Schüssler, M., 1994, A dynamo effect due to instability of magnetic flux tubes, Astron. & Astrophys., 289, 949

Galloway, D. J., Weiss, N. O., 1981, Convection and magnetic fields in stars, Astrophys. J., 243, 945

Granzer, T., Schüssler, M., Caligari, P., Strassmeier, K. G., 2000, Distribution of starspots on cool stars. II. Pre-main-sequence and ZAMS stars between 0.4 $M_\odot$ and 1.7 $M_\odot$, Astron. & Astrophys., 355, 1087

Hall, D. S., Henry, G. W., 1994, The Law of Starspot Lifetimes, International Amateur-Professional Photoelectric Photometry Communications, 55, 51

Harvey, K. L., 1993, Magnetic dipoles on the Sun, Ph.D. thesis, , Univ. Utrecht

Harvey, K. L., Zwaan, C., 1993, Properties and emergence of bipolar active regions, Solar Phys., 148, 85

Hathaway, D. H., 1996, Doppler Measurements of the Sun's Meridional Flow, Astrophys. J., 460, 1027

Holzwarth, V., 2002, Dynamik magnetischer Flussröhren in Riesensternen und engen Doppelsternen, PhD thesis, Universität Göttingen

Holzwarth, V., Mackay, D. H., Jardine, M., 2006, The impact of meridional circulation on stellar butterfly diagrams and polar caps, Mon. Not. Royal Astron. Soc., 369, 1703, `arXiv:astro-ph/0604102`

Holzwarth, V., Schmitt, D., Schüssler, M., 2007, Flow instabilities of magnetic flux tubes. II. Longitudinal flow, Astron. & Astrophys., 469, 11, `arXiv:0704.3685`

Howard, R., 1974, Studies of solar magnetic fields. II - The magnetic fluxes, Solar Phys., 38, 59

Hoyng, P., Schmitt, D., Teuben, L. J. W., 1994, The effect of random alpha-fluctuations and the global properties of the solar magnetic field, Astron. & Astrophys., 289, 265

Hussain, G. A. J., 2002, Starspot lifetimes, Astronomische Nachrichten, 323, 349

Işık, E., Schüssler, M., Solanki, S. K., 2007, Magnetic flux transport on active cool stars and starspot lifetimes, Astron. & Astrophys., 464, 1049, `arXiv:astro-ph/0612399`

Işık, E., 2004, Magnetic activity and orbital dynamics of the K-dwarf triple system DH Leonis, in Spectroscopically and Spatially Resolving the Components of the Close Binary Stars, (Eds.) R. W. Hilditch, H. Hensberge, K. Pavlovski, vol. 318 of Astronomical Society of the Pacific Conference Series, p. 251

Kővári, Z., Strassmeier, K. G., Granzer, T., Weber, M., Oláh, K., Rice, J. B., 2004, Doppler imaging of stellar surface structure. XXII. Time-series mapping of the young rapid rotator LQ Hydrae, Astron. & Astrophys., 417, 1047

Krause, F., Rädler, K. H., 1980, Mean-field magnetohydrodynamics and dynamo theory, Oxford: Pergamon Press, 1980

Mackay, D. H., Priest, E. R., Lockwood, M., 2002, The Evolution of the Sun's Open Magnetic Flux - II. Full Solar Cycle Simulations, Solar Phys., 209, 287

Mackay, D. H., Jardine, M., Cameron, A. C., Donati, J.-F., Hussain, G. A. J., 2004, Polar caps on active stars: magnetic flux emergence and transport, Mon. Not. Royal Astron. Soc., 354, 737

Martínez Pillet, V., Moreno-Insertis, F., Vazquez, M., 1993, The distribution of sunspot decay rates, Astron. & Astrophys., 274, 521

Martínez Pillet, V., Lites, B. W., Skumanich, A., 1997, Active Region Magnetic Fields. I. Plage Fields, Astrophys. J., 474, 810

Miesch, M. S., 2005, Large-Scale Dynamics of the Convection Zone and Tachocline, Living Reviews in Solar Physics, 2, 1

Moffatt, H. K., 1978, Magnetic field generation in electrically conducting fluids, Cambridge, England, Cambridge University Press, 1978

Moffatt, K., Murdin, P., 2000, Dynamo Theory, Encyclopedia of Astronomy and Astrophysics

Montesinos, B., Thomas, J. H., Ventura, P., Mazzitelli, I., 2001, A new look at the relationship between activity, dynamo number and Rossby number in late-type stars, Mon. Not. Royal Astron. Soc., 326, 877

Moreno-Insertis, F., 1986, Nonlinear time-evolution of kink-unstable magnetic flux tubes in the convective zone of the sun, Astron. & Astrophys., 166, 291

Moreno-Insertis, F., Schüssler, M., Ferriz-Mas, A., 1992, Storage of magnetic flux tubes in a convective overshoot region, Astron. & Astrophys., 264, 686

Moreno-Insertis, F., Caligari, P., Schüssler, M., 1995, “Explosion” and Intensification of Magnetic Flux Tubes, Astrophys. J., 452, 894

Ossendrijver, M., 2003, The solar dynamo, Astron. & Astrophys. Rev., 11, 287

Parker, E. N., 1975, The generation of magnetic fields in astrophysical bodies. X - Magnetic buoyancy and the solar dynamo, Astrophys. J., 198, 205

Petrovay, K., Moreno-Insertis, F., 1997, Turbulent Erosion of Magnetic Flux Tubes, Astrophys. J., 485, 398–+, `astro-ph/9703152`

Petrovay, K., van Driel-Gesztelyi, L., 1997, Making Sense of Sunspot Decay. I. Parabolic Decay Law and Gnevyshev-Waldmeier Relation, Solar Phys., 176, 249, `astro-ph/9706029`

Pidatella, R. M., Stix, M., 1986, Convective overshoot at the base of the sun’s convection zone, Astron. & Astrophys., 157, 338

Rempel, M., Schüssler, M., 2001, Intensification of Magnetic Fields by Conversion of Potential Energy, Astrophys. J. Lett., 552, L171

Rempel, M., Schüssler, M., Tóth, G., 2000, Storage of magnetic flux at the bottom of the solar convection zone, Astron. & Astrophys., 363, 789

Roberts, B., Webb, A. R., 1978, Vertical motions in an intense magnetic flux tube, Solar Phys., 56, 5

Rüdiger, G., Hollerbach, R., 2004, The magnetic universe : geophysical and astrophysical dynamo theory, ISBN 3-527-40409-0. Wiley-VCH

Schmitt, D., 2003, Dynamo action of magnetostrophic waves, in Advances in Nonlinear Dynamos, The Fluid Mechanics of Astrophysics and Geophysics, (Eds.) A. Ferriz-Mas, M. Núñez, Taylor and Francis, p. 83

Schmitt, D., Schüssler, M., 1989, Non-linear dynamos. I - One-dimensional model of a thin layer dynamo, Astron. & Astrophys., 223, 343

Schou, J., Antia, H. M., Basu, S., Bogart, R. S., Bush, R. I., Chitre, S. M., Christensen-Dalsgaard, J., di Mauro, M. P., Dziembowski, W. A., Eff-Darwich, A., Gough, D. O., Haber, D. A., Hoeksema, J. T., Howe, R., Korzennik, S. G., Kosovichev, A. G., Larsen, R. M., Pijpers, F. P., Scherrer, P. H., Sekii, T., Tarbell, T. D., Title, A. M., Thompson, M. J., Toomre, J., 1998, Helioseismic Studies of Differential Rotation in the Solar Envelope by the Solar Oscillations Investigation Using the Michelson Doppler Imager, Astrophys. J., 505, 390

Schrijver, C. J., 2001, Simulations of the Photospheric Magnetic Activity and Outer Atmospheric Radiative Losses of Cool Stars Based on Characteristics of the Solar Magnetic Field, Astrophys. J., 547, 475

Schrijver, C. J., 2002, Solar spots as prototypes for stellar spots, Astronomische Nachrichten, 323, 157

Schrijver, C. J., Harvey, K. L., 1994, The photospheric magnetic flux budget, Solar Phys., 150, 1

Schrijver, C. J., Title, A. M., 2001, On the Formation of Polar Spots in Sun-like Stars, Astrophys. J., 551, 1099

Schüssler, M., 2005, Flux tubes, surface magnetism, and the solar dynamo: constraints and open problems, Astronomische Nachrichten, 326, 194

Schüssler, M., Ferriz Mas, A., 2007, Flow instabilities of magnetic flux tubes. I. Perpendicular flow, Astron. & Astrophys., 463, 23

Schüssler, M., Rempel, M., 2005, The dynamical disconnection of sunspots from their magnetic roots, Astron. & Astrophys., 441, 337, `arXiv:astro-ph/0506654`

Schüssler, M., Solanki, S. K., 1992, Why rapid rotators have polar spots, Astron. & Astrophys., 264, L13

Schüssler, M., Caligari, P., Ferriz-Mas, A., Solanki, S. K., Stix, M., 1996, Distribution of starspots on cool stars. I. Young and main sequence stars of 1 $M_\odot$, Astron. & Astrophys., 314, 503

Shaviv, G., Salpeter, E. E., 1973, Convective Overshooting in Stellar Interior Models, Astrophys. J., 184, 191

Sheeley, Jr., N. R., 2005, Surface Evolution of the Sun's Magnetic Field: A Historical Review of the Flux-Transport Mechanism, Living Reviews in Solar Physics, 2, 5

Skaley, D., Stix, M., 1991, The overshoot layer at the base of the solar convection zone, Astron. & Astrophys., 241, 227

Snodgrass, H. B., 1983, Magnetic rotation of the solar photosphere, Astrophys. J., 270, 288

Snodgrass, H. B., Dailey, S. B., 1996, Meridional Motions of Magnetic Features in the Solar Photosphere, Solar Phys., 163, 21

Solanki, S. K., 1993, Smallscale Solar Magnetic Fields - an Overview, Space Sci. Rev., 63, 1

Solanki, S. K., Unruh, Y. C., 2004, Spot sizes on Sun-like stars, Mon. Not. Royal Astron. Soc., 348, 307, `astro-ph/0311310`

Spruit, H. C., 1981, Motion of magnetic flux tubes in the solar convection zone and chromosphere, Astron. & Astrophys., 98, 155

Spruit, H. C., van Ballegooijen, A. A., 1982, Stability of toroidal flux tubes in stars, Astron. & Astrophys., 106, 58

Strassmeier, K. G., 2002, Doppler images of starspots, Astronomische Nachrichten, 323, 309

Strassmeier, K. G., 2005, Stellar activity cycles: observing the dynamo?, Astronomische Nachrichten, 326, 269

Tobias, S. M., Brummell, N. H., Clune, T. L., Toomre, J., 2001, Transport and Storage of Magnetic Field by Overshooting Turbulent Compressible Convection, Astrophys. J., 549, 1183

Ulrich, R. K., Boyden, J. E., 2005, The Solar Surface Toroidal Magnetic Field, Astrophys. J. Lett., 620, L123

van Ballegooijen, A. A., 1982, The overshoot layer at the base of the solar convective zone and the problem of magnetic flux storage, Astron. & Astrophys., 113, 99

van Ballegooijen, A. A., Cartledge, N. P., Priest, E. R., 1998, Magnetic Flux Transport and the Formation of Filament Channels on the Sun, Astrophys. J., 501, 866

Vögler, A., Schüssler, M., 2007, A solar surface dynamo, Astron. & Astrophys., 465, L43, `arXiv:astro-ph/0702681`

Vogt, S. S., Hatzes, A. P., Misch, A. A., Kürster, M., 1999, Doppler Imagery of the Spotted RS Canum Venaticorum Star HR 1099 (V711 Tauri) from 1981 to 1992, Astrophys. J. Supp. Ser., 121, 547

Wang, Y.-M., 1998, Cyclic Magnetic Variations of the Sun, in ASP Conf. Ser. 154: Cool Stars, Stellar Systems, and the Sun, (Eds.) R. A. Donahue, J. A. Bookbinder, pp. 131

Wang, Y.-M., Nash, A. G., Sheeley, Jr., N. R., 1989a, Magnetic flux transport on the sun, Science, 245, 712

Wang, Y.-M., Nash, A. G., Sheeley, Jr., N. R., 1989b, Evolution of the sun's polar fields during sunspot cycle 21 - Poleward surges and long-term behavior, Astrophys. J., 347, 529

Publications

Publications in refereed scientific journals

- Işık, E., Schüssler, M., Solanki, S. K., 2007, Magnetic flux transport on active cool stars and starspot lifetimes, *Astronomy and Astrophysics*, 464, 1049
- Işık, E., Schmitt, D., Schüssler, M., 2007, A coupled model of magnetic flux generation and transport in stars, *Astronomische Nachrichten*, 328, 1111

Contributed paper in conference proceedings

- Işık, E., Schüssler, M., Solanki, S. K., 2007, Magnetic flux transport and the lifetimes of spots on active cool stars, in: F. Kneer, K.G. Puschmann, A.D. Wittmann (eds.) *Modern solar facilities - advanced solar science*, Universitätsverlag Göttingen

Acknowledgements

I would like to thank Manfred Schüssler for his great supervision during my PhD project, in the course of which I have become a driven oscillator and acquired a “magnetic” activity cycle with a period of exactly one week, thanks to his stimulating discussions.

I thank Sami Solanki for contributing to my initial motivation, and thought-provoking discussions about the magnetic flux transport models on active cool stars. I am thankful to Franz Kneer for accepting me as a PhD student at the University. I will miss our Solar Group seminars and tea discussions at the Institute of Astrophysics in Göttingen.

I am grateful to Dieter Schmitt for his generous practical help about the dynamo model, along with fruitful discussions. Of course, many thanks for his great effort in running the International Max Planck Research School on Physical Processes in almost everywhere in the Solar System and even related “Beyond” (e.g. this thesis). I feel lucky that we have *been* to the Beyond, for the unforgettable Solar Eclipse Retreat in Antalya, Turkey.

I am indebted to Volkmar Holzwarth for welcoming me in St. Andrews, and then flooding me with an oceanful of information on simulations and physics of thin magnetic flux tubes. Again, I feel lucky that shortly after my visit, he moved back to Lindau, where he continued with the flood of useful discussions, and has been only a few steps away for my occasional linear and nonlinear disturbances.

I thank Ingo Baumann for introducing me the flux transport mechanism on the Sun and much help with understanding his numerical code.

I also thank to Robert Cameron for sharing his broad spectrum of interesting ideas and intuitions.

I thank Antonio Ferriz-Mas for very interesting discussions and lectures on the fundamentals of (magneto-)hydrodynamics, thermodynamics, dynamo theory, and how to pour a bottle of hefeweizen beer into a glass in a rigourous way.

And all the student/postdoc friends (for example, chan chan Lotfi), despite the Lindau damping, thanks for sharing a fascinating three years at the heart of Germany. I will always remember our first-time skiing adventures in Harz, and the fascinating expeditions to the nearest city, Göttingen.

I am indebted to my pre-PhD professors, especially Zeki Aslan for supporting my plans and giving suggestions, and Rennan Pekünlü for the stimulating, interactive MHD courses to which I owe my motivation of coming here to work with M. Schüssler.

My special thanks are to my wife Arzu, who has been patiently waiting and working in Antalya, for her generous support... I am indebted to my parents Nejla and İbrahim for the love and humanism that they have given, and to my great brother Murat, especially for the astronomy book he sent me from Malta in 1993.

Lebenslauf

Name:	Emre Işık
Geburt:	Am 07.10.1977 in Trabzon, Türkei
Staatsangehörigkeit:	türkisch
Schulbildung:	09/1991 bis 06/1994: 50. Yıl Tahran Lisesi, Göztepe, Istanbul
Studium:	09/1994 bis 06/1998: Astronomiestudium an der Ege Universität in Izmir Lisans diploması (Batchelor of Science)
	10/1999 bis 07/2002: Master of Science in Physik an der Akdeniz Universität in Antalya Assistent an der Abteilung für Physik
	09/2002 bis 12/2004: Promotionsstudent in Physik an der Akdeniz Universität in Antalya Assistent an der Abteilung für Physik
	01/2005 bis 01/2008: Doktorand der International Max Planck Research School on Physical Processes in the Solar System and Beyond, am Max-Planck-Institut für Sonnensystemforschung in Katlenburg-Lindau